The Hydrated Excess Proton Studied by Nonlinear Time-Resolved Vibrational Spectroscopy

Dissertation

zur Erlangung des akademischen Grades

doctor rerum naturalium
(Dr. rer. nat.)

im Fach Physik

eingereicht an der
Mathematisch-Naturwissenschaftlichen Fakultät
der Humboldt-Universität zu Berlin

von

Diplom-Biophysiker Fabian Dahms

Präsident der Humboldt-Universität zu Berlin
Prof. Dr.-Ing. Dr. Sabine Kunst

Dekan der Mathematisch-Naturwissenschaftlichen Fakultät
Prof. Dr. Elmar Kulke

Gutachter:

1. Prof. Dr. Thomas Elsässer
2. Prof. Dr. Oliver Benson
3. Prof. Dr. Peter Hamm

Eingereicht am: 19.03.2018
Tag der Disputation: 03.07.2018

Abstract

The excess proton (H^+) in aqueous environment, elusive in its structure and local surrounding, has been intensively studied for more than two centuries and is often discussed in terms of two limiting structures, the Eigen cation ($H_9O_4^+$) and the Zundel cation ($H_5O_2^+$). However, the prevailing solvation structure and ultrafast fluctuating character of the hydrated proton in solution at room temperature is debated. The present thesis elucidates a predominant solvation structure of excess protons in solution under thermal equilibrium conditions. Zundel cations selectively prepared in acetonitrile solution are investigated by ultrafast two-dimensional infrared (2D-IR) and two-color pump-probe spectroscopy. OH stretching and bending vibrations of the flanking water molecules in the $H_5O_2^+$ moiety are discerned from the proton transfer vibration ($O\cdots H\cdots O$) and the absorption continuum, a hallmark of Zundel cations in solution, by their markedly different vibrational character. Intramolecular lifetimes are found in the sub-100 fs range, much shorter than for neat liquid water. The "Zundel continuum" is explained by solvent driven field fluctuations that modulate the double minimum proton potential in $H_5O_2^+$ on the femtosecond time scale. Together with stochastic populations of low frequency modes, both effects lead to strong frequency excursions of the proton transfer fundamental and its overtone and combination tone transitions. Utilizing the distinct vibrational character of the proton transfer mode, time-resolved data of Zundel cations in acetonitrile are compared to those obtained for excess protons in bulk liquid water. The nearly identical vibrational response of both samples found in 2D-IR and two-color pump-probe experiments identifies the $H_5O_2^+$ moiety as a predominant solvation structure of protons in water. A concentration-dependent steady state infrared spectroscopy series of different water/acetonitrile mixtures hosting the excess protons is used to demonstrate the persistence of the Zundel-type hydration structure in polar solvation environments.

Kurzfassung

Das Überschussproton (H^+) in wässriger Umgebung, schwer fassbar in seiner Struktur und seinem lokalen Umfeld, wurde seit mehr als zwei Jahrhunderten intensiv studiert und wird oft in Bezug auf zwei limitierende Strukturen diskutiert, dem Eigen-Kation ($H_9O_4^+$) und dem Zundel-Kation ($H_5O_2^+$). Die vorherrschende Hydratisierungsstruktur und der ultraschnelle fluktuierende Charakter des Überschussprotons in Lösung bei Raumtemperatur bleiben jedoch diskutiert. Die vorliegende Dissertation klärt eine dominante Hydratisierungsstruktur von Überschussprotonen in Lösung unter thermischen Gleichgewichtsbedingungen auf. Zundel-Kationen, selektiv präpariert im Lösungsmittel Acetonitril, wurden mittels ultraschneller zweidimensionaler Infrarot (2D-IR) und Zweifarben-Anrege-Abtastspektroskopie untersucht. OH Streck- und Biegeschwingungen der flankierenden Wassermoleküle der $H_5O_2^+$-Gruppierung konnten anhand ihres eindeutig unterschiedlichen Schwingungscharakters von der Protontransferschwingung ($O\cdots H\cdots O$) und der kontinuierlichen Absorption, ein Kennzeichen von Zundel-Kationen in Lösung, unterschieden werden. Intramolekulare Lebensdauern liegen im sub-100 fs Bereich, viel kürzer als in reinem flüssigen Wasser. Das „Zundel-Kontinuum" erklärt sich durch Lösungsmittel getriebene Feldfluktuationen, die das Doppelminimumpotential des Protons in $H_5O_2^+$ auf der Femtosekundenzeitskala modulieren. Zusammen mit stochastische Besetzungen niederfrequenter Moden, führen beide Effekte zu einer starken Frequenzverschiebung der Fundamentalschwingung der Protonbewegung und ihrer Ober- und Kombinationstöne. Der einzigartige Schwingungscharakter der Protontransfermode wurde ausgenutzt, um zeitaufgelöste Daten von Zundel-Kationen in Acetonitril mit denen von Überschussprotonen in flüssigem Wasser zu vergleichen. Die nahezu identische Schwingungsantwort beider Proben in 2D-IR und Zweifarben-Anrege-Abtastexperimenten identifiziert die $H_5O_2^+$-Gruppierung als eine vorherrschende Hydratisierungsstruktur für Protonen in Wasser. Eine konzentrationsabhängige Serie verschiedener Überschussprotonen enthaltender Wasser/Acetonitril-Mischungen, wurde mittels stationärer Infrarotspektroskopie analysiert und dazu verwendet, die Beständigkeit von Zundelartigen Hydratisierungsstrukturen in polaren Solvatationsumgebungen zu demonstrieren.

Contents

List of Abbreviations

- 2D Two-Dimensional
- ACN Acetonitrile
- ATR Attenuated Total Reflection
- ESA Excited State Absorption
- FROG Frequency Resolved Optical Gating
- FTIR Fourier Transform Infrared
- FWHM Full Width at Half Maximum
- GSB Ground State Bleach
- H bond Hydrogen Bond
- PES Potential Energy Surface
- IR Infrared
- mid-IR Mid-Infrared
- OPA Optical Parametric Amplifier
- SE Stimulated Emission
- TG Transient Grating
- VER Vibrational Energy Relaxation
- XC Cross-Correlation

1 Introduction

The proton H^+ is a unique chemical species, that is a proton nucleus with no electrons, and thus can be described as a "bare charge" [1]. Owing to its high reactivity [1,2] and anomalously high mobility in chemical environments such as water [3–6], H^+ plays an important role in chemistry [1,2,7–10], biology [11–14] and technological applications [15,16].
Albeit the general agreement on a structural diffusion concept ("Grotthuss diffusion") to explain the migration of the charge defect in water (Fig. 1.1), the local environment of H^+ during active and resting periods of proton transfer steps has remained elusive. The hydrated excess proton is typically described by two limiting structures, the Eigen cation (E) ($H_9O_3^+$) [7,8,17] and the Zundel cation (Z) ($H_5O_2^+$) [18], named in honor of the pioneering researchers Manfred Eigen and Georg Zundel[1].
Extensive theoretical and experimental efforts [20–22] to elucidate the microscopic mechanism of proton transport in water resulted in conflicting views and have steered a controversy about the relative abundance and stability of Eigen and Zundel type structures in the liquid phase.
Theoretical simulations of protons in water are extremely challenging. The minimum configuration energies of the fully hydrated Eigen and Zundel cation are similar and none of the structures can a priori be selected as more stable with currently available simulation techniques [23,24]. Multistate empirical valence bond (MS-EVB) studies of hydrated excess protons in water assign the Eigen cation as the more stable structure in solution [25]. Furthermore, the fluctuating character of the water environment scrambles the proton motifs and leads to inter-conversion of species expected on the picosecond time scale, closely linked

[1] The $H_5O_2^+$ complex was actually first suggested by Huggins in the year 1936 [19].

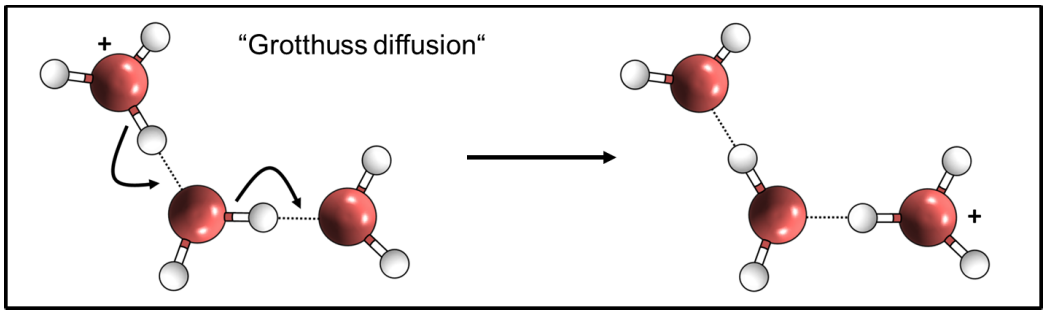

Figure 1.1: Schematic depiction of structural "Grotthuss" diffusion for the charge defect in water. Red and white balls represent oxygen and hydrogen atoms, respectively. The proton is effectively shuttled along "water chains" by consecutive hydrogen bond breaking and reforming events.

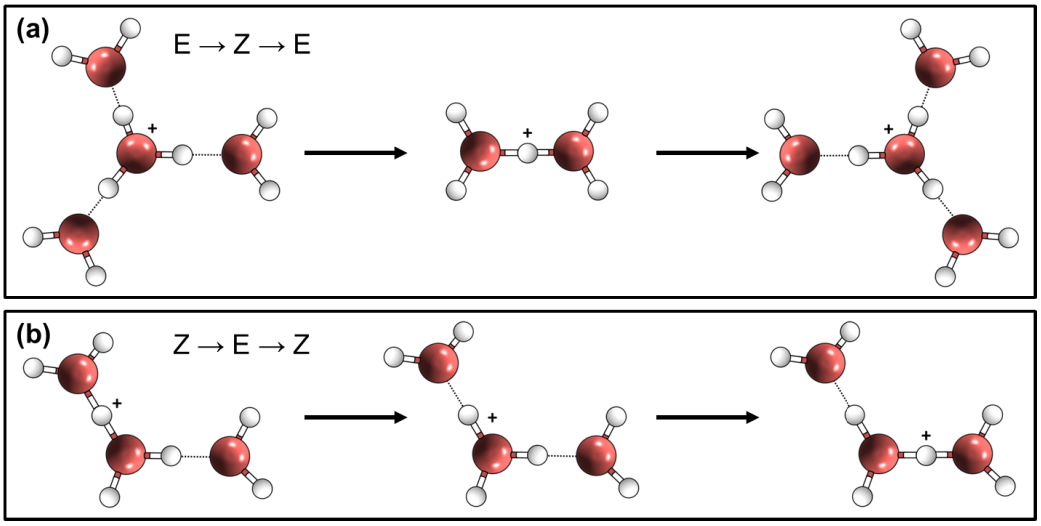

Figure 1.2: In the longstanding debate on the microscopic picture of proton transport processes in water, typically two mechanisms are discussed. **(a)** The excess proton is hydrated in an Eigen complex during the resting period between successful proton transfer events. A stimulus, such as a hydrogen bond breaking event triggers the charge migration and the Eigen cation transiently becomes a Zundel cation. The transfer mechanism ends with the formation of yet another Eigen cation, so that the charge has effectively "hopped" to a neighboring water molecule. This mechanism is referred to as an Eigen to Zundel to Eigen (E-Z-E) mechanism, that has made its way into modern textbooks [10]. **(b)** Same principles apply as in (a) but the meta-stable structure is the Zundel cation $H_5O_2^+$. The Eigen cation appears only as a fleeting transition state in the Z-E-Z mechanism.

to the average lifetime of a hydrogen bond in bulk water [26]. The "fluxional" character of the charge defect poses special demands on the theoretical framework, e.g., accounting for hydrogen bond dynamics and the inclusion of quantum effects resulting in high computational cost [20, 22].

Time-resolved spectroscopy in the mid-infrared (mid-IR) spectral range (2,5-25 μm) with femtosecond (1 fs = $1{\times}10^{-15}$ s) time resolution has the potential to map the dynamical properties of the charge defect in real time. Such experiments require precise knowledge about spectroscopic marker modes that can be linked to either Eigen or Zundel type species. Gas phase studies of ultracold protonated water clusters have helped identifying these modes experimentally [27], but the extrapolation into the liquid phase is debated [28]. Protons in water at ambient conditions display an absorption continuum spanning a range from at least 1000 cm^{-1} to almost 4000 cm^{-1}, a trait absent in gas phase clusters. Vibrational lineshapes are substantially broadened and absorption features that are clearly separated in the gas phase become difficult to discern in the liquid phase [29].

To circumvent such complicating matters, this work relies on the predominant preparation of a prototypical species in acetonitrile (ACN) – the Zundel cation $H_5O_2^+$ [30]. Acetonitrile is a particularly suitable solvent, as the polar ACN molecules undergo structural fluctuations on a multitude of time scales with strong contributions in the sub-100 fs range, similar to water [31]. Consequently, the fluctuating character of the environment that bulk water imposes on the hydrated excess proton is, to a certain degree, retained. Such a benchmark system gives the unique opportunity to collect species dependent experimental data that

can directly be linked to theoretical calculations. In a next step, the benchmark system is compared to protons in water.
Moreover, Zundel cations prepared in ACN provide an attractive alternative to describe the hydrated proton in biological environments with partial hydration. Among such systems are proton channels [12], the surface area of proteins [32] or reactive sites of enzymes [33] that are poorly described by protons in bulk water.
The approach outlined above bears the potential to propel the field of research forward − a field that has struggled with the structural ambiguity of the hydrated proton in bulk water and the lack of meaningful experimental data for a long time. Although this study does not qualify to make a definite statement on the microscopic proton transfer mechanism in water, e.g., a E-Z-E (Fig. 1.2a) vs. Z-E-Z (Fig. 1.2b) mechanism, it will elucidate the role of the Zundel cation from a new perspective.

Outline

The thesis is structured as follows. Chapter 2 sketches the elusiveness of the hydrated proton with help of influential literature from the past century and introduces the concept of this study. Chapter 3 will provide a brief summary of the theoretical description of molecular vibrations and nonlinear vibrational spectroscopy followed by a detailed description of the experimental setups that were used to collect the time-resolved 2D-IR and two-color pump-probe data. To benchmark our results on Zundel cations in ACN, results on water monomers in ACN are discussed in detail in chapter 4. Chapter 5 provides a characterization of Zundel cations selectively prepared in acetonitrile. Here, experimental observations are linked to theoretical simulations culminating in a compelling picture to describe the absorption continuum of Zundel cations in the liquid phase. Results of ultrafast mid-infrared experiments obtained for Zundel cations in ACN are directly compared to results obtained for protons in water in chapter 6. The final chapter 7 presents a summary and conclusion.

2
Overview & Concept

2.1 Pictures of Proton Transport in Water

This section gives a brief summary of the current pictures of proton transport in water. Owing the importance of the topic across many fields in science, there exists a vast amount of literature. It is beyond the scope of this work to cover every contribution to the field but a brief overview of the development is sketched with the help of influential literature from the past decades. Exemplary review articles are [20–22]. In this context, hydrogen bonding in water and the basic dynamics of neat liquid water are briefly discussed before presenting the hydrated excess proton.

2.1.1 Hydrogen Bonding

"The hydrogen bond is the most important of all directional intermolecular interactions. It is operative in determining molecular conformation, molecular aggregation, and the function of a vast number of chemical systems ranging from inorganic to biological." [37]

A hydrogen bond (H bond) is defined as the local bond interaction between a proton donating group $X{-}H$ and a proton acceptor A [37]:

$$X - H \cdots A \ . \tag{2.1}$$

Water, the medium for life, has been the subject of intense studies for decades [38–40] and many of its special properties can be linked to the complex three-dimensional hydrogen bond network formed between molecules in the bulk. Here the OH group of one water molecule acts as the proton donor and the oxygen atom of another water molecule as the proton acceptor:

$$O - H \cdots O \ . \tag{2.2}$$

To put the hydrogen bond of water into perspective, we want to rely on a correlation plot with empirical data obtained for various solids by Novak and Libowitzky [34, 35]. Fig. 2.1 displays the OH stretching frequency as a function of the O$\cdots$O distance. The regression curve (red line, taken from [35]) relates a certain O$\cdots$O distance to a specific OH stretching frequency. It should be noted, that the calculated curve only gives a rough approximation, as is evident from the experimental data (symbols) that scatter around the theoretical curve. The average O$\cdots$O distance of hydrogen bonded molecules in bulk water is 2.82 Å [41] and the OH stretching vibrations have a frequency of approximately 3400 cm^{-1} (cf. Fig. 2.2), in good agreement with the regression curve in Fig. 2.1. Following the definitions of Jeffrey [36], this classifies the hydrogen bonds in water as moderate in regards of their strength and the

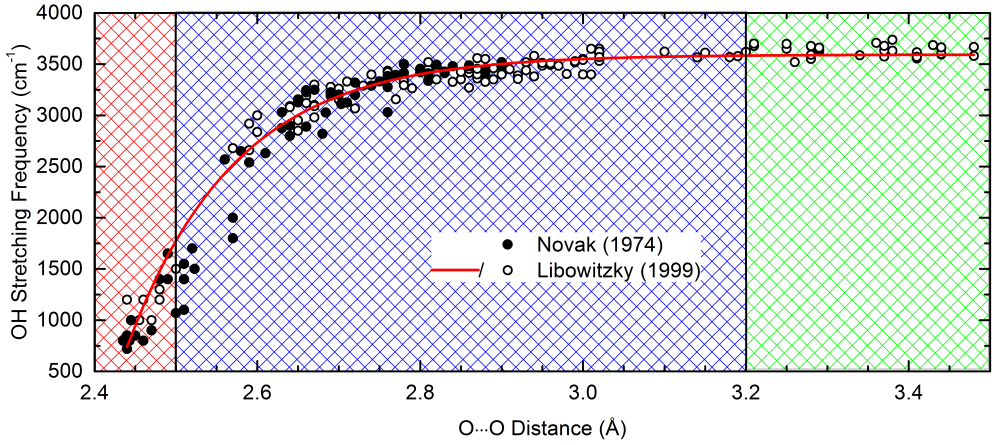

Figure 2.1: OH stretching frequency as a function of O···O distance for various solids taken from [34, 35]. The regression curve (red line) correlates a certain OH stretching frequency with a specific O· · ·O distance. Red, blue, and green patterned areas indicate strong, moderate and weak hydrogen bonds following the definitions proposed by Jeffrey [36].

interaction forces are mostly electrostatic (blue patterned regime in Fig. 2.1).
Hydrogen bonds in complexes involving the hydrated proton are substantially stronger compared to bulk water. For the Eigen core (H_3O^+), OH stretching frequencies shift by about 700 cm^{-1} to lower frequencies and absorb at 2700 cm^{-1} (cf. Fig. 3.18 on page 49). For the fully hydrated Eigen complex ($H_9O_4^+$), the interaction forces can be separated into mainly covalent contributions for the three hydrogen atoms bonded to the central oxygen and mainly electrostatic interactions between the central hydronium and the three water molecules in its first solvation shell. For the Zundel cation however, a clear separation between electrostatic and covalent contributions becomes difficult. The central hydrogen bond in $H_5O_2^+$ becomes substantially shorter than the average hydrogen bond in bulk water (∼2.4 Å vs. ∼2.8 Å) and classifies as a strong hydrogen bond (red patterned regime in Fig. 2.1) [36]. The O···H···O stretching vibration absorbs at approximately 1200 cm^{-1} (cf. Fig. 5.2 on page 68) deviating from the regression curve in Fig. 2.1.
There are many experimental methods that are suitable to investigate the local structure of hydrogen bonded systems, such as x-ray or neutron diffraction experiments [42]. Although offering excellent spacial resolution, these methods lack time resolution and only provide static structures. Time-resolved nuclear magnetic resonance studies provide an alternative to map hydrogen bond dynamics but due to the longer wavelength, direct observations are hampered. For liquid phase systems like bulk water, complicated hydrogen bond dynamics occur on fast time scales and better time resolution is needed.

2.1.2 Water

For a long time, understanding the dynamical properties of water on the microscopic level has been a major challenge, especially in the liquid phase [26, 43–45]. Ultrafast energy redistribution processes, intertwined with highly fluctuating hydrogen bond dynamics lead to complex and convoluted spectroscopic signatures (blue line in Fig. 2.2a). To map such events in real time and to deconvolute the fundamental mechanisms leading to the observed lineshapes, both powerful experimental and theoretical techniques are needed. With the

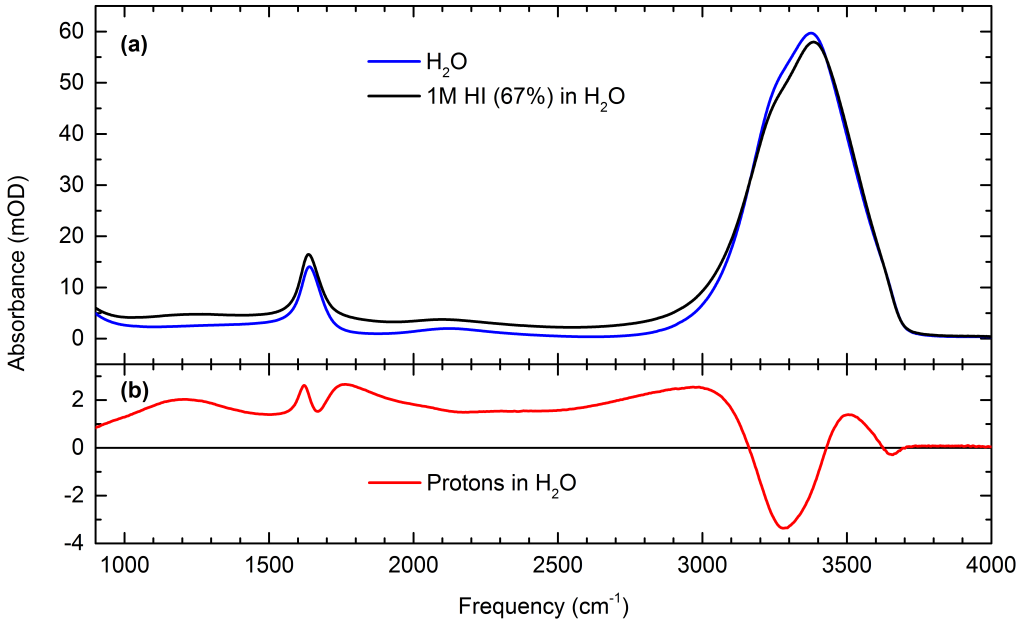

Figure 2.2: **(a)** Steady state absorption spectra of H_2O (blue line) and 1 M HI (67 % wt. in H_2O) in H_2O (black line) measured in attenuated total reflection (ATR). The addition of HI to neat H_2O leads to an increased absorption in the 900-3100 cm^{-1} range and a slight absorption decrease from 3100-3400 cm^{-1}. **(b)** The difference spectrum of H_2O (blue line) and 1 M HI (67 % wt. in H_2O) in H_2O (black line) reveals the complex absorption spectrum of protons in water (red line).

implementation of Ti:Sapphire laser systems, nonlinear mid-infrared spectroscopy has become a powerful tool to investigate the dynamics of liquid water on femtosecond time scales. These studies, in combination with theory, have shaped our understanding of the dynamical properties of liquid water at ambient conditions in the recent years.

The linear absorption spectrum of bulk water in a range from 900-4000 cm^{-1} is displayed in Fig. 2.2a (blue line). It shows strong absorption features of hindered rotations (librations) of water molecules with a maximum at 670 cm^{-1} (cf. Fig. 1 in [46]) and a high frequency tail extending up to 1750 cm^{-1}. The rather sharp band at 1650 cm^{-1} is assigned to the intramolecular OH bending vibration of the water molecules. The absorption feature around 2100 cm^{-1}, usually referred to as the association band of water [47], is assigned to a combination band of intermolecular librations (at ∼400 cm^{-1}) and the intramolecular bending fundamental (at 1650 cm^{-1}) [47–51]. The symmetric and asymmetric OH stretching vibrations cannot be distinguished in the linear absorption spectrum of bulk water and show up as one strong absorption feature in the 2900-3700 cm^{-1} range.

The most prominent hallmark of neat liquid water is its complex and disordered intermolecular hydrogen bond network, that rearranges on a multitude of time scales. Such hydrogen bond dynamics and vibrational energy dissipation have been studied by ultrafast nonlinear infrared spectroscopy and theory [26, 44, 46, 52–56] .

The transition frequency of the OH stretching vibration depends critically on its local environment and makes it an excellent probe of structure. As there is no long-range ordering in the H bond network [26, 54], water molecules in the bulk experience different local environments, that fluctuate on ultrafast time scales. Studies employing ultrafast 2D-IR

spectroscopy in the range of the OH stretching vibration [53] have shown, that correlations in the water structure are lost extremely fast, with librational motions as the dominating contributions, leading to spectral diffusion of the OH stretching vibrations on a 50 fs time scale. Moreover, OH stretching oscillators of different water molecules are coupled by the intermolecular hydrogen bonds and mechanisms, such as dipole-dipole coupling, leading to a resonant energy transfer between neighboring water molecules on a 75 fs time scale [53]. Furthermore, it has been shown that upon vibrational excitation of the OH stretching vibrations the energy relaxes on a femtosecond time scale in a cascade like mechanism [46,52–55]. The v = 1 state of the OH stretching oscillators decays with a 200 fs lifetime. This fast decay is facilitated by the Fermi resonance of the OH bending overtone and the symmetric OH stretching fundamental, hence making the bending vibration an excellent primary acceptor for the excess energy. The OH bending vibration is the intramolecular vibration lowest in frequency and represents the gateway to intermolecular energy transfer from an initially excited water molecule into its local environment. The bending vibration relaxes on a 170 fs time scale and the excess energy is transferred to the "libration continuum" [46,52]. Intermolecular energy transfer in neat liquid water leads to sub-100 fs nuclear rearrangements, where the H bonds in the close viscinity of the initially excited molecule are weakened but unbroken and correlations in the water structure are lost [52, 53]. Subsequent energy delocalization occurs on a slower ∼1 ps time scale and is linked to hydrogen bond breaking and reforming events resulting in a macroscopically heated liquid. This state persists for more than 500 ps and leaves the intermolecular hydrogen bonds weakened, thus shifting intramolecular transition frequencies.

2.1.3 The Hydrated Excess Proton

What happens upon addition of excess protons to liquid water? A question with fundamental importance across all fields of science [14, 16, 57], that has been subject of controversial discussion for centuries [20–22].
H^+ ions in water have an anomalously high mobility (3.62×10^{-3} cm^2/Vs) compared to other ions of similar size [3–5]. What are the underlying mechanisms that facilitate such anomalously high mobility?
A first conceptual idea of structural diffusion can be traced back over two centuries to an original paper by Johann Dietrich von Grotthuss published in the year 1805 [58], where he postulated migration of "negative/positive properties" along "chains of water molecules". His idea of structural diffusion, where breaking and reforming events of the "water chains" effectively shuttle the "negative/positive property" was termed "Grotthuss diffusion" (cf. Fig. 1.1 on page 11) and is the basis of nowadays interpretations [20].
More than a century later, different descriptions of limiting structures for the hydrated excess proton were proposed by Manfred Eigen [7, 8, 17] and Georg Zundel [18]. Eigen and coworkers attribute the hydrated excess proton to a single water molecule forming the hydronium core (H_3O^+), with all three protons covalently bound to the central oxygen atom. In their picture, the hydronium core is solvated by three water molecules forming $H_9O_4^+$, later known as the "Eigen cation" (Fig. 2.3).
In contrast, Zundel and coworkers propelled a picture where the excess proton is shared by two flanking water molecules forming the $H_5O_2^+$ complex, later termed the "Zundel cation" (Fig. 2.4). In subsequent papers [59, 60], they discussed the extremely high polarizability of the central hydrogen bond in the protonated water dimer. Their analysis let to a picture where the observed absorption continuum, a hallmark of excess protons in water (cf.

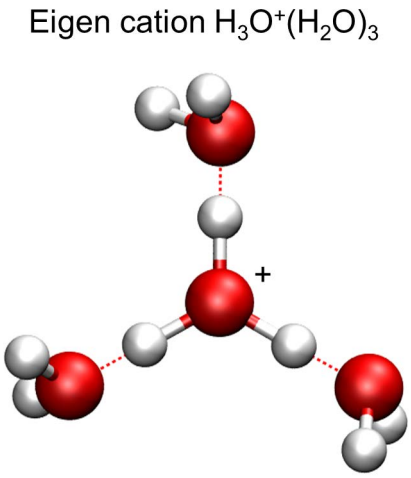

Figure 2.3: $H_9O_4^+$ structure as proposed by Manfred Eigen. The central hydronium (H_3O^+) is fully solvated by three water molecules in its first hydration shell. The excess proton H^+ is covalently bond to the central oxygen atom and the hydrogen bonds formed to the first shell waters are expected to be stronger compared to those formed in bulk water [61]. This cation was later termed the "Eigen cation".

Fig. 2.2b), could be explained by the fluctuating character of the shared proton tunneling through the barrier of its double minimum potential. Nevertheless, their calculations were based on a one-dimensional potential that was insufficient to describe proton transfer in water.
The quick advancements in computer technology in the following years lead to the development of more powerful calculation methods. With ab initio molecular dynamics simulations (AIMD), especially Car-Parinello molecular dynamics (CPMD) and multistate empirical valence bond (MS-EVB) methods on the rise, it soon became clear that proton tunneling in protonated water clusters only remains relevant for certain ice phase conditions [21, 22].
With modern theoretical and experimental tools at hand, a remarkable effort was spent in the last decades to elucidate proton transport processes in aqueous environments on the microscopic level [21, 23, 28, 30, 62–91] . However, the ambiguity of hydrated excess proton motifs scrambled by the fluctuating water environment and the nearly identical minimum configuration energies of fully hydrated Zundel and Eigen structures within theoretical methods of moderate cost, has led to controversial theories of proton transport in water.
The von Grotthuss picture was revisited by Agmon in 1995 [66], where he critically analyzed present experimental and theoretical data to deduce a proton transfer mechanism. The approach taken has been reminiscent of the model for acid dissociation in water as reported by Hynes et al. [63–65, 73]. Agmon advanced a picture of an Eigen to Zundel to Eigen mechanism (E-Z-E) (cf. Fig. 1.2 on page 12), where a hydrogen bond breaking event in a second shell water of the hydronium triggers the transfer process. Following the hydrogen bond cleavage, he expected readjustments of bond angles and lengths on the femtosecond time scale to form an intermediate Zundel cation. In this picture, the protonated water dimer acts only as a short lived transition state that will be re-isomerized by fluctuations of the surrounding water dipoles, hence the rate limiting step is the hydrogen bond cleavage in the second shell. The proposed mechanism was qualitatively consistent with the results from the first AIMD simulation by Tuckerman et al. in the same year [67].

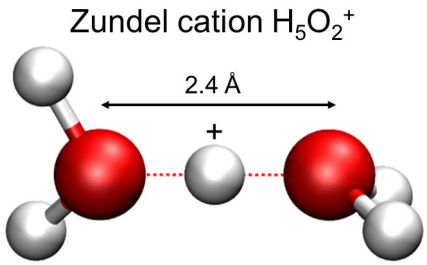

Figure 2.4: $H_5O_2^+$ structure as proposed by Georg Zundel. The excess proton is shared in between two flanking water molecules via an exceptionally strong hydrogen bond. The bond length of ∼2.4 Å is substantially shorter than the average hydrogen bond length in bulk water (∼2.8 Å) [102]. This cation was later termed the "Zundel cation"

This picture was refined a couple of years later by inclusion of quantum effects using the ab initio path integral method [23]. Here, Marx et al. demonstrated that the topological defect for protons in water cannot be characterized entirely by terms of Eigen and Zundel structures. They showed that quantum effects, like zero point motion, blur out the barrier between inter-conversion of the complexes. In this regard, they introduced the term of a "fluxional complex" that only approaches the "idealized" Zundel and Eigen structures as limiting terms [22].
On this basis, the so called "presolvation concept" was developed [92]. This concept is based on the preferred 4-fold tetrahedral solvation structure of bulk water molecules [93] and that the proton receiving species must have a solvation pattern that corresponds to the species it will be transformed to. This unifying model was used to explain various structural diffusion processes in hydrogen bonded systems [94–97] including proton transport in water [92].
MS-EVB studies in combination with AIMD trajectories simulated for excess protons in water have generated a conflicting picture, where the fully hydrated Eigen core ($H_9O_4^+$) features a "special pair" in the resting state before a transition, again propagating an E-Z-E mechanism [83, 98]. Here, the resting state is a distorted Eigen cation with one of its water ligands in closer proximity and one further away than the average. The identity of the special pair interchanges in the first hydration shell of H_3O^+ on a 40-45 fs time scale and is called the "special pair dance", closely linked to the cleavage of an acceptor type hydrogen bond. In this picture, the protonated water dimer ($H_5O_2^+$) acts as a fleeting transition state mediating the transfer of the proton to a neighboring water molecule.
Despite the detailed theoretical descriptions of proton transport in water, the experimental investigation has been a major challenge and still lacks behind today. Gas phase studies in combination with theoretical simulations [27, 99–101] have helped to assign characteristic spectral features to ultracold Eigen and Zundel complexes. The identification of marker modes is a necessary prerequisite for any experimental study on hydrated protons in solution, where they exhibit a complex and convoluted steady state absorption spectrum covering almost the entire mid-infrared region (cf. Fig. 2.2b).
Woutersen et al. used ultrafast pump-probe spectroscopy on partially deuterated water/HCl solutions to deduce vibrational and structural dynamics of the hydrated excess proton [103]. They claimed similar vibrational lifetimes for the OH stretching vibrations of Zundel and Eigen cations on the order of 120 fs with a sub 100 fs inter-conversion of these complexes. Their interpretation follows the ideas of the 1999s nature paper by Marx et al. [23], linking their experimental observations to the proposed two-step model [22]. Here, the sub 100 fs

inter-conversion time is regarded as the direct observation of the second step in the model, where the proton H^+ is transferred from H_3O^+ to a neighboring water molecule with reduced coordination number including $H_5O_2^+$ as a transition state.
Several years later, Thämer et. al employed two-dimensional infrared spectroscopy to investigate the dynamical properties of the hydrated excess proton in water/HCl solutions [29]. They analyzed cross-peaks in two-dimensional spectra between the Zundel OH bending vibration at $\sim$1730 cm^{-1} and OH stretching vibration at $\sim$3400 cm^{-1} (cf. Fig 5.2 on page 68) to conclude that these cations are an important species for proton solvation in water. Further, they estimated a minimum lifetime of 470 fs for such complexes, invoking that Zundel cations are not just a fleeting transition state in the proton transfer process, as thought for many years and in clear contradiction to leading theories [20–22].
With the extensive experimental and theoretical efforts spent, various ideas of proton transport in water have been proposed and received partial confirmation. However, compelling experimental data are still lacking, adding to the controversial view of proton transport in water. So far, one has mainly relied on OH stretching and bending vibrations as a local probe for the dynamics of the excess proton. More elaborate experimental studies are needed, that are able to directly map the proton dynamics and clearly discriminate Zundel from Eigen type structures in order to drive the understanding of proton transport in water forward.

2.2 Concept of This Study

The previous section sketched the theoretical and experimental effort that has been undertaken in order to decipher the structural heterogeneity and dynamics of hydrated excess protons. Up to date, compelling experimental data remains scarce owing to the many challenges that are inherently linked to the investigated system.
First and foremost, excess protons in liquid water exhibit a complex and convoluted linear absorption spectrum (cf. Fig. 2.2) that is overlapped with the intense absorption features of bulk water. Moreover, one expects rapid inter-conversion between different hydrated proton complexes on the picosecond time scale, which is at the heart of proton migration in water. Probing such systems spectroscopically requires in depth knowledge about vibrational dynamics and signatures of the involved species in order to disentangle the complex signals. Up to date, such knowledge is lacking and experimentally investigating protons in liquid water seems premature.
In this work, an approach is presented that makes use of a chemically well defined benchmark system that greatly reduces the complexity of the problem at hand. Taking this step back enables the collection of data for a prototypical species in solution, in particular the Zundel cation $H_5O_2^+$. Understanding the benchmark system is a mandatory step before investigating excess protons in bulk water.
This concept is based on the work by Kalish et al. [30]. They have investigated strong mineral acids ($HClO_4$, HCl, HBr, HI, HCF_3SO_3) in water/acetonitrile mixtures with steady state infrared spectroscopy. Here, small protonated water clusters that are embedded in an acetonitrile environment, are created and their size is controlled by the water content added to the solution. In this study, they identified the spectral features of the hydronium (H_3O^+) only for very small ratios between excess protons (H^+) and water molecules (H_2O). With the addition of water, they found the protonated water dimer ($H_5O_2^+$) to be the main solvation structure of the excess protons in H_2O/ACN mixtures and the corresponding spectral

features remained almost unchanged for water concentrations up to 10 M. These important results show that even for larger proton water clusters in acetonitrile, the core motive is that of a Zundel cation.

3
Fundamentals

3.1 Theoretical Description of Nonlinear Spectroscopy

This section provides the theoretical background to understand the time-resolved pump-probe and 2D-IR data and the respective analyses in the following chapters. These concepts have been described in detail elsewhere [104–107].
Linear spectroscopy is often not sufficient to describe and disentangle complex spectra, especially for condensed phase systems. Correlations, couplings or mechanisms that lead to the observed line broadening remain hidden in stationary spectra. Nonlinear spectroscopy, with multiple light-matter interactions, bears the potential to reveal underlying dynamics and kinetics, correlate different spectral features, and allows for conclusions on molecular structure. To understand nonlinear spectroscopy, a brief introduction to molecular vibrations, couplings and lineshapes is given. The nonlinear response of an ensemble of states will be discussed with perturbation theory of the density matrix. Such light-matter interactions can be represented with double-sided Feynman diagrams. To conclude this section, a more detailed description of the relevant third-order nonlinear response functions will be presented.

3.1.1 Molecular Vibrations and Couplings

Vibrational modes describe periodic displacements of atoms in a molecule with respect to each other. These vibrations have characteristic frequencies which depend on their potential energy surface as defined by the electronic structure of the molecule. Moreover, molecular vibrations can be affected by various influences, such as neighboring molecules, field fluctuations, hydrogen bonding, intra- and inter-molecular couplings and many more. These properties make them an excellent probe of structure and dynamics of the molecular ensemble.
The field-free and isolated molecule is represented by the Hamiltonian:

$$\begin{aligned}\hat{H} &= \hat{T} + \hat{V}(r) \\ &= -\sum_i \frac{\hbar^2}{2m_e}\nabla_e^2 - \sum_i \frac{\hbar^2}{2m_{n,i}}\nabla_n^2 + V_{ee} + V_{nn} + V_{en} \ .\end{aligned} \tag{3.1}$$

The kinetic energy $\hat{T}$ is described by the first two terms on the right-hand side of the second part of Eqn. 3.1, with the sum over all electrons and nuclei with the masses m_e and m_n, respectively. The potential energy $\hat{V}(r)$ can be split into three contributions. These arise from Coulomb repulsion between the electrons (V_{ee}) and the nuclei (V_{nn}) and from Coulomb attraction between the electrons and nuclei (V_{en}).

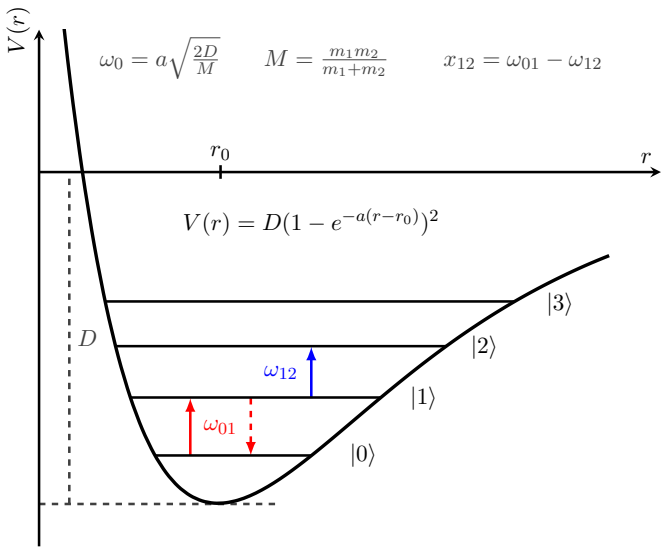

Figure 3.1: Anharmonic Morse potential describing a molecular vibration. In the potential of the form $V(r) = D[1 - exp(-a(r - r_0))]^2$, D describes the dissociation energy, a the curvature of the potential and r the bond length. Ground state bleaching and stimulated emission between the $|0\rangle$ and $|1\rangle$ state are depicted with solid and dashed red arrows, respectively. The excited state absorption between the $|1\rangle$ and $|2\rangle$ state is shown in blue.

We start by describing a single anharmonic vibrational mode with the potential energy curve of a Morse oscillator [106]:

$$V(r) = D(1 - e^{-a(r-r_0)})^2 \ , \tag{3.2}$$

where r is the bond length, r_0 the equilibrium position, D the dissociation energy and a the curvature of the potential.
Considering the vibrational potential $V(r)$ shown in Fig. 3.1, repulsion is the driving force for very short distances r between the atoms of a molecule. For distances larger than r_0, attractive terms dominate until further separation leads to dissociation of the bond. The potential can be approximated as harmonic only for small distances around the equilibrium position r_0. Consequently the energy splitting between consecutive vibrational states narrows with each higher lying state.
The vibrational eigenstates can be found by solving the time independent Schrödinger equation:

$$\hat{H}|n\rangle = E|n\rangle \ . \tag{3.3}$$

In our case this yields:

$$E_n = \hbar\omega \left(n + \frac{1}{2}\right) - x\left(n + \frac{1}{2}\right)^2 \ , \tag{3.4}$$

with the harmonic frequency ω, quantum number n and the anharmonicity x [108].
An external stimulus, such as an incident light field can change the vibrational states of a molecule. For example, a molecule in the vibrational ground state $|0\rangle$ will be in the first excited state after resonant interaction with an incident light field:

$$\omega_{in} = \hbar\omega - 2x \equiv \omega_{01} \ , \tag{3.5}$$

here ω_{in} and ω are the frequencies of the incident light field and molecular vibrator, respectively. In nonlinear spectroscopy, this process is called ground state bleaching (GSB), where population is transferred from the $|0\rangle$ to $|1\rangle$ state (solid red arrow in Fig. 3.1). If the molecule was already in the first excited state, resonant interaction with an external light field would take it into the second exited state, a process called excited state absorption (ESA) (solid blue arrow in Fig. 3.1):

$$\omega_{incident} = \hbar\omega - 4x \equiv \omega_{12} \ , \tag{3.6}$$

or the molecule would return back to the ground state through stimulated emission (SE) (dashed red arrow in Fig. 3.1).
We now want to extend the picture of an isolated molecular vibration by introducing a coupling to a second vibrator. In a simplified way, one can express coupling as the dependence of the transition frequency of one oscillator on the excitation state of the other. One generally distinguishes intra- and intermolecular couplings between different vibrational modes of a single molecule and vibrational modes between different molecules, respectively. In the simplest bilinear approximation, the combined potential $V(r_1, r_2)$ can be written as:

$$V(r_1, r_2) = V_1(r_1) + V_2(r_2) + \beta_{12} r_1 r_2 \ , \tag{3.7}$$

with

$$\beta_{12} = \frac{1}{4\pi\epsilon_0}\left[\frac{\vec{\mu}_1 \cdot \vec{\mu}_2}{r_{12}^3} - 3\frac{(\vec{r}_{12} \cdot \vec{\mu}_1)\,(\vec{r}_{12} \cdot \vec{\mu}_2)}{r_{12}^5}\right] \ , \tag{3.8}$$

where $V(r_1)$ and $V(r_2)$ are the one-dimensional potentials of two coupled oscillators and $\beta_{12} r_1 r_2$ is the coupling between them. Note that Eqn. 3.7 is only valid in the limit where bilinear coupling is dominant. Eqn. 3.8 holds for dipole-dipole coupling with $\vec{\mu} = \langle 1|e\vec{r}|0\rangle$. The vibrational eigenstates can be retrieved by diagonalizing $\hat{H}(r_1, r_2)$. The coupling between the oscillators will alter their respective energies of the quantum states, which will result in shifted transition frequencies. In nonlinear vibrational spectroscopy such changes can be monitored and thus give insight in the vicinity and couplings of the probed oscillator.

We now consider a nonlinear molecule of N atoms with $3N-6$ vibrational degrees of freedom. For small displacements, we expand the vibrational potential $V(\vec{r})$ in a normal mode basis with a Taylor expansion for the coordinate $\vec{r}_i (i = 0, ..., 3N-6)$ [109]:

$$\begin{aligned} V(\vec{r}) = V(\vec{r}_0) + \sum_{i=1}^{3N-6} \left.\frac{\partial V}{\partial r_i}\right|_{\vec{r}_0} r_i + \frac{1}{2}\sum_{i,j=1}^{3N-6} \left.\frac{\partial^2 V}{\partial r_i \partial r_j}\right|_{\vec{r}_0} r_i r_j \\ + \frac{1}{6}\sum_{i,j,k=1}^{3N-6} \left.\frac{\partial^3 V}{\partial r_i \partial r_j \partial r_k}\right|_{\vec{r}_0} r_i r_j r_k + \ldots \end{aligned} \tag{3.9}$$

The first term $V(\vec{r}_0)$ describes the potential energy in the equilibrium configuration and sets the zero point for measured vibrational potential energies. The first-order gradient $F_1 = {}^{\partial V}/_{\partial r_i}|_{\vec{r}_0}$ vanishes at equilibrium configuration so that only quadratic and higher terms have to be considered in Eqn. 3.9 [110]. One should note, that these higher order terms introduce anharmonicity [106]. Consequently, including the anharmonicities x_{ik} of the

potentials allows for an approximation of the vibrational energies similar to Eqn. 3.4 [106]:

$$E_{n_i}(i=1,...,3N-6) \approx \sum_{i=1}^{3N-6} \hbar\omega_i \left(n_i + \frac{1}{2}\right) + \sum_{i=1}^{3N-6} \sum_{k\geq i}^{3N-6} x_i k \left(n_i + \frac{1}{2}\right)\left(n_k + \frac{1}{2}\right) + \dots \tag{3.10}$$

In condensed phase systems, polyatomic molecules are embedded in a fluctuating and complex environment that deforms and modulates vibrational potentials on a multitude of time scales, making an explicit description difficult.
Subsection 3.1.4 will introduce an approach to treat such systems time-dependent with perturbation theory of the density matrix.

3.1.2 Vibrational Lineshapes

The lineshapes of vibrational transitions are of special interest in nonlinear vibrational spectroscopy.
In an interaction-free model system, transition frequencies $\omega_{ij}(i=0,...,n; j=1,...,m$ with $n<m)$ are stationary, where the indexes i and j denote the states of the oscillator. In reality however, the potential energy surface of a molecule will be perturbed by the interaction with its environment, consequently modulating the transition frequencies ω_{ij}. The time dependence of the transition frequency leads to dephasing processes that can be measured in real time with nonlinear vibrational spectroscopy, revealing the underlying dynamics of the molecular system (e.g. [111]). In the following, a brief summary of dephasing and the consequences on the measured lineshapes will be given using a concept, that was originally formulated for NMR transitions but can be extrapolated for vibrational spectroscopy [106, 112].
Structural changes in the environment of a molecule will perturb its vibrational energy surface and the instantaneous transition frequency $\omega_{ij}(t)$ will fluctuate around an average value ω_{ij}. In the Kubo picture, this relation is expressed with a simple equation:

$$\omega_{ij}(t) = \omega_{ij} + \delta\omega_{ij}(t) \ , \tag{3.11}$$

with ω_{ij} as the mean frequency and $\delta\omega_{ij}(t)$ describes the fluctuating part of Eqn. 3.11.
Assuming a time dependent transition dipole moment:

$$\mu_{ij}(t) = \mu_{ij}(0)e^{i\omega_{ij}t} \ , \tag{3.12}$$

we can express the fluctuating transition frequency $\omega_{ij}(t)$ by the equation of motion of the corresponding dipole moment:

$$\dot{\mu}_{ij} = -i\omega_{ij}(t)\mu_{ij}(t) \ . \tag{3.13}$$

Formally solving Eqn. 3.13, while also considering that not a single molecule, but an ensemble of molecules in the sample is excited by the laser pulse, gives:

$$\begin{aligned}\mu_{ij}(t) &= \mu_{ij}(0)\left\langle exp\left(-i\int_0^t \mathrm{d}\tau\ \omega_{ij}(\tau)\right)\right\rangle \\ &= \mu_{ij}(0)e^{-i\omega_{ij}t}\left\langle exp\left(-i\int_0^t \mathrm{d}\tau\ \delta\omega_{ij}(\tau)\right)\right\rangle \ .\end{aligned} \tag{3.14}$$

Here ensemble averaging is indicated by $\langle ... \rangle$. Eqn. 3.14 is commonly evaluated using the cumulant expansion that is truncated after the second order [106]:

$$\left\langle exp\left(-i\int_0^t \mathrm{d}\tau\ \delta\omega_{ij}(\tau)\right)\right\rangle \equiv e^{-g(t)}\ , \tag{3.15}$$

where $g(t)$ is the lineshape function:

$$g(t) = \frac{1}{2}\int_0^t\int_0^t \mathrm{d}\tau'\mathrm{d}\tau''\left\langle\delta\omega_{ij}(\tau')\delta\omega_{ij}(\tau'')\right\rangle\ . \tag{3.16}$$

It should be noted, that Eqn. 3.15 is only exact for Gaussian distributions of $\delta\omega_{ij}$ and the lineshape function $g(t)$ simplifies to:

$$g(t) = \int_0^t\int_0^{\tau'} \mathrm{d}\tau'\mathrm{d}\tau''\langle\delta\omega_{ij}(\tau'')\delta\omega_{ij}(0)\rangle \tag{3.17}$$

for stationary processes $\langle\delta\omega_{ij}(\tau')\delta\omega_{ij}(\tau'')\rangle$.
The frequency-frequency correlation function (FFCF) $C(t)$:

$$C(t) \equiv \langle\delta\omega_{ij}(\tau)\delta\omega_{ij}(0)\rangle \tag{3.18}$$

is a fundamental quantity in vibrational spectroscopy of condensed phase systems that connects the experimental observables and the microscopic molecular dynamics [113]. In a sense, the decay of the FFCF represents the memory of a molecule's vibrational frequency in the system. In the Kubo picture, the decay of $C(t)$ is described with an exponential ansatz:

$$\langle\delta\omega_{ij}(\tau)\delta\omega_{ij}(0)\rangle = \Delta\omega_{ij}^2 e^{\frac{-|\tau|}{\tau_c}}\ , \tag{3.19}$$

where $\Delta\omega_{ij}^2$ is the fluctuation amplitude and τ_c the correlation time. Integrating Eqn. 3.19 twice yields the Kubo lineshape function:

$$g(t) = \Delta\omega_{ij}^2\tau_c^2\left[e^{-\frac{t}{\tau_c}} + \frac{t}{\tau_c} - 1\right]\ . \tag{3.20}$$

In the homogeneous limit (or fast modulation limit), frequency fluctuations are very rapid or very small so that $e^{-t/\tau_c} \to 0$ and $t/\tau_c \gg 1$. We can simplify the lineshape function in Eqn. 3.20 to:

$$g(t) = \Delta\omega_{ij}^2\tau_c t \equiv \frac{t}{T_2^*}\ , \tag{3.21}$$

where T_2^* is the pure dephasing time:

$$T_2^* = \frac{1}{\Delta\omega_{ij}^2\tau_c}\ , \tag{3.22}$$

resulting in a Lorentzian lineshape with a width of $1/T_2^*$. The correlation time is much smaller than the pure dephasing time ($\tau_c \ll T_2^*$), if the fast modulation limit applies [106]. An interesting consequence is that the observed linewidth becomes narrower than the actual distribution of frequencies $\Delta\omega_{ij}$. One can think of the molecule's frequencies fluctuating so rapidly, that one only observes the average. This phenomenon is called *motional narrowing* [114].

We now consider the opposite case. Frequency fluctuations are large or very slow, so that $\Delta\omega_{ij}^2\tau_c \gg 1$. In the inhomogeneous (or slow modulation) limit the FFCF can be approximated as constant:

$$\langle\Delta\omega_{ij}(\tau)\Delta\omega_{ij}(0)\rangle = \Delta\omega_{ij}^2 \ , \tag{3.23}$$

so that the lineshape function can be written as:

$$g(t) = \frac{\Delta\omega_{ij}^2}{2}t^2 \ . \tag{3.24}$$

Without a dependence on the correlation time τ_c, Eqn. 3.24 simply represents a static distribution of frequencies. This results in a Gaussian lineshape of width $\Delta\omega_{ij}$.
In condensed-phase systems, the FFCF typically decays multiexponentially in between both limiting cases. In most systems, one finds faster components on the order of hundreds of femtoseconds and slower diffusive contributions that clock on the picosecond time scale. In other words, the frequencies of the molecules are gradually shifted over time, a process called *spectral diffusion*.
Considering homogeneous and inhomogeneous broadening mechanisms, one can approximate the lineshape function as:

$$\begin{aligned}\langle\omega_{ij}(t)\omega_{ij}(0)\rangle &= \frac{\delta(t)}{T_2^*} + \Delta\omega_{ij}^2 \\ g(t) &= \frac{t}{T_2^*} + \frac{\Delta\omega_{ij}^2}{2}t^2 \ .\end{aligned} \tag{3.25}$$

The resulting lineshape is a Voigt profile, consisting of both Lorentzian and Gaussian contributions.
In liquid environments, a clear separation of the time scales into fast and slow modulations becomes difficult, hence stationary infrared lineshapes do not reveal the mechanisms leading to ultrafast frequency fluctuations. Experimental methods, e.g., time-resolved nonlinear spectroscopy with femtosecond IR pulses, allow to monitor instantaneous frequency distributions in real time, thus providing access to the interactions that cause $\delta\omega_{ij}(t)$.

3.1.3 Nonlinear Polarization

In our nonlinear experiments (section 3.2), we investigate the properties of a material by its interactions with mid-IR laser pulses. Sufficiently strong input fields ($E \approx 5{\cdot}10^9$ V/cm [115]) generate a nonlinear macroscopic polarization $\vec{P}(\vec{r},t)$ in the material that according to the wave equation:

$$\vec{\nabla}^2\vec{E}(\vec{r},t) - \frac{1}{c^2}\frac{\partial^2\vec{E}(\vec{r},t)}{\partial t^2} = \frac{4\pi}{c^2}\frac{\partial^2\vec{P}(\vec{r},t)}{\partial t^2} \tag{3.26}$$

is the source of a new emitted field $\vec{E}_{sig}$ (with c as the speed of light in vacuum). The signal field $\vec{E}_{sig}$ contains all information about the interaction of the incident light field with the sample and thus calculating the macroscopic nonlinear polarization is at the very heart of vibrational spectroscopy:

$$\vec{E}_{sig}(\vec{r},t) \propto i\vec{P}(\vec{r},t) \ . \tag{3.27}$$

$\vec{P}(\vec{r},t)$ is directly connected to the microscopic dipole moments $\vec{\mu}$ of a material and can be expressed as the expectation value of the transition dipole $\vec{\mu}(t)$:

$$\vec{P}(\vec{r},t) \propto \langle\vec{\mu}(t)\rangle \cdot N \ . \tag{3.28}$$

The following subsection will present a treatment to calculate the nonlinear macroscopic polarization $\vec{P}(\vec{r},t)$ in Eqn. 3.28 of an ensemble of molecules.

3.1.4 Perturbative Expansion of the Density Matrix

An eligible approach to describe the response of an ensemble of molecules comes with the density matrix formalism [116, 117]. Here, the nonlinear polarization $\vec{P}$ can be expressed as the expectation value of the dipole operator times the density matrix ρ by taking the trace[1]:

$$\vec{P}(t) = Tr\left[\vec{\mu}\rho(t)\right] \equiv \langle\vec{\mu}\rho(t)\rangle \ . \tag{3.29}$$

We now write the time dependent Hamiltonian $H(t)$ as the time independent system Hamiltonian H_0 treated exactly and an interaction between a molecular dipole $\vec{\mu}$ and an external electric field $\vec{E}(t)$ accounted by $H'(t)$:

$$\begin{aligned} H(t) &= H_0 + H'(t) \\ &= H_0 - \vec{\mu}\vec{E}(t) \ . \end{aligned} \tag{3.30}$$

Assuming to know the stationary states of the molecule and that the interaction with an external electric field $-\vec{\mu}\vec{E}(t)$ is much weaker than the internal fields of the molecule, allows to treat the interaction perturbatively.
The time evolution of the density matrix is given by the Liouville von Neuman equation:

$$\begin{aligned} \frac{d}{dt}\rho(t) &= -\frac{i}{\hbar}\left[H,\rho(t)\right] \\ \Rightarrow \frac{d}{dt}\rho_I(t) &= -\frac{i}{\hbar}[H'_I(t),\rho_I(t)] \ , \end{aligned} \tag{3.31}$$

with:

$$\rho_I(t) = e^{\frac{i}{\hbar}H_0\cdot(t-t_0)}\rho(t)e^{-\frac{i}{\hbar}H_0\cdot(t-t_0)} \text{ and } H'_I(t) = e^{\frac{i}{\hbar}H_0\cdot(t-t_0)}H'(t)e^{-\frac{i}{\hbar}H_0\cdot(t-t_0)} \ . \tag{3.32}$$

In Eqn. 3.31, we have rewritten the Liouville von Neuman equation using the interaction picture.
In the interaction picture the dipole operator $\vec{\mu}$ is time dependent and the advantage over the Schrödinger picture is that the time evolution is now determined only by the interaction Hamiltonian $H'_I(t)$. We can expand the density matrix in powers of the weak perturbation $H'_I(t)$:

$$\rho_I(t) = \rho_I(t_0) + \sum_{n=1}^{\infty}\rho_I^n(t) \ , \tag{3.33}$$

[1] Definition of the density matrix of a statistical ensemble of molecules:
$\rho = \sum_i p_i|\psi_i\rangle\langle\psi_i|$ with p_i as the probability of the system being in state $|\psi_i\rangle$

Properties of the density matrix:

1. hermitian: $\rho_{nm} = \rho^*_{mn}$
2. ρ_{nm} can be viewed as the probability to find the system in state $|n\rangle$
3. diagonal elements describe the population states of a system and must be non-negative
4. off-diagonal elements describe the coherences between the states

where $\rho_I(t_0)$ is the equilibrium density matrix which does not evolve in time, so we can write the n$^{\text{th}}$-order density matrix as:

$$\rho_I^{(n)}(t) = \left(-\frac{i}{\hbar}\right)^n \int_{t_0}^{t} \mathrm{d}\tau_n \int_{t_0}^{\tau_n} \mathrm{d}\tau_{n-1} ... \times \int_{t_0}^{\tau_2} \mathrm{d}\tau_1 \left[H_I'(\tau_n), \left[H_I'(\tau_{n-1}, ... \left[H_I'(\tau_1), \rho_I(t_0)\right] ...\right]\right] \ . \tag{3.34}$$

Plugging Eqn. 3.30 into Eqn. 3.34 and making use of Eqn. 3.29 we can formulate the n$^{\text{th}}$-order nonlinear polarization for $t_0 \to -\infty$:

$$P^{(n)}(t) = \left(-\frac{i}{\hbar}\right)^n \int_{-\infty}^{t} \mathrm{d}\tau_n \int_{-\infty}^{\tau_n} \mathrm{d}\tau_{n-1} ... \int_{-\infty}^{\tau_2} \mathrm{d}\tau_1 E(\tau_n)E(\tau_{n-1})...E(\tau_1) \times \langle \mu_I(t) \left[\mu_I(\tau_n), [\mu_I(\tau_{n-1}), ... \left[\mu_I(\tau_1), \rho(-\infty)\right] ...\right]\right] \rangle \ . \tag{3.35}$$

In a last step, we want to use a different set of time variables, where τ_n are absolute time points and t_n describe time intervals[2], so that we can write the n$^{\text{th}}$-order nonlinear polarization as a convolution of n electric fields $E(t)$ with the n$^{\text{th}}$-order nonlinear response function $R^{(n)}(t)$:

$$P^{(n)}(t) = \int_0^{\infty} \mathrm{d}t_n \int_0^{\infty} \mathrm{d}t_{n-1} ... \int_0^{\infty} \mathrm{d}t_1 \times E(t-t_n)E(t-t_n-t_{n-1}...E(t-t_n-t_{n-1}-...-t_1)R^{(n)}(t_n, t_{n-1}, ..., t_1) \tag{3.36}$$

with

$$R^{(n)}(t_n, ..., t_1) = \left(-\frac{i}{\hbar}\right)^n \times \langle \mu_I(t_n + ... + t_1) \cdot \left[\mu_I(t_{n-1} + ... + t_1), ... \left[\mu_I(0), \rho(-\infty)\right] ...\right] \rangle \ . \tag{3.37}$$

One should note that the response function is only valid for positive times t_n to fulfill the requirements of causality. Interactions at times $0, t_1, ...$ and $t_{n-1} + .. + t_1$ perturb the equilibrium density matrix, hence population states generated are described by the diagonal elements of the non-equilibrium density matrix $\rho^{(n)}$. The off-diagonal elements are oscillating coherences between the states, emitting a light field at times $t_n + t_{n-1} + .. + t_1$. The third order nonlinear response functions $R^{(3)}$ relevant for the experiments of this work will be discussed in more detail in the next subsection.

3.1.5 3$^{\text{rd}}$-Order Nonlinear Response Function

We start this subsection by writing down all possible combinations of the commutator shown in Eqn. 3.37 for the third order explicitly. If we permute the various bra and ket interactions on the density matrix, we can write down 2^{n} terms, hence 16 terms for n = 3. The number reduces to eight (2^{n-1}) unique terms for the third order response function, as the other half

[2] $\tau_1 = 0,\ t_1 = \tau_2 - \tau_1,\ t_2 = \tau_3 - \tau_2,\ ...\ ,\ t_n = t - \tau_n$

is just the complex conjugate form[3]:

$$\begin{aligned}
&\langle\mu(t_3+t_2+t_1)[\mu(t_2+t_1),[\mu(t_1),[\mu(0),\rho(-\infty)]]]\rangle = \\
R_4 \quad &+\langle\mu(t_3+t_2+t_1)\mu(t_2+t_1)\mu(t_1)\mu(0)\rho(-\infty)\rangle \\
R_1^* \quad &-\langle\mu(t_3+t_2+t_1)\mu(t_2+t_1)\mu(t_1)\rho(-\infty)\mu(0)\rangle \\
R_2^* \quad &-\langle\mu(t_3+t_2+t_1)\mu(t_2+t_1)\mu(0)\rho(-\infty)\mu(t_1)\rangle \\
R_3 \quad &+\langle\mu(t_3+t_2+t_1)\mu(t_2+t_1)\rho(-\infty)\mu(0)\mu(t_1)\rangle \\
R_3^* \quad &-\langle\mu(t_3+t_2+t_1)\mu(t_1)\mu(0)\rho(-\infty)\mu(t_2+t_1)\rangle \\
R_2 \quad &+\langle\mu(t_3+t_2+t_1)\mu(t_1)\rho(-\infty)\mu(0)\mu(t_2+t_1)\rangle \\
R_1 \quad &+\langle\mu(t_3+t_2+t_1)\mu(0)\rho(-\infty)\mu(t_1)\mu(t_2+t_1)\rangle \\
R_4^* \quad &-\langle\mu(t_3+t_2+t_1)\rho(-\infty)\mu(0)\mu(t_1)\mu(t_2+t_1)\rangle\ .
\end{aligned} \tag{3.38}$$

Keeping track of the various light-matter interactions and the origin of a particular nonlinear signal proves rather difficult using nonlinear response functions. Hence one often uses double-sided Feynman diagrams for a visual representation.

Double-sided Feynman diagrams

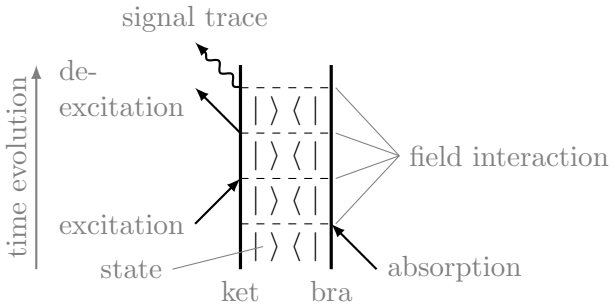

Figure 3.2: Sketch of a Feynman diagram without specified states. The two thick vertical lines represent the ket and bra side of the density matrix ρ. Dashed horizontal lines stand for field interactions that affect the states of a molecule. Absorption events are depicted by inward pointing arrows and stimulated emission by outward pointing arrows. These interactions can happen either on the ket or bra side of ρ, respectively. The signal trace is by definition always emitted on the ket side and the time evolves from bottom to top.

Feynman diagrams are an accessible way to show the explicit series of excitation and de-excitation events that appear as an action of the dipole operator on the density matrix. It is also a clear way to keep track of the contribution of each incident electric field $\vec{E}$ to the frequency ω and wavevector $\vec{k}$ of the nonlinear polarization. Fig. 3.2 shows an exemplary sketch of a Feynman diagram without specific states of the system. Thick vertical bars on the left and right represent the ket and bra side of the density matrix ρ, respectively. The dipole operator can act from both sides on ρ and each interaction is depicted as a horizontal dashed line and specified by an arrow. Time evolves from bottom to top. In-pointing arrows represent an excitation event leading to an up-climbing of the density matrix. Out-pointing

[3] Notice that we are still in the interaction picture. The indices I have been dropped for the sake of simplicity and the time dependence of the dipole operator μ is indicated by $\mu(t_n)$.

arrows represent de-excitation. The signal trace is by convention always emitted from the ket side. The emitted frequency ω_{sig} and wavevector k_{sig} are the sum of the input frequencies ω_n and wavevectors k_n. Arrows pointing to the right and left represent electric fields with $e^{-i\omega t+ikr}$ and $e^{+i\omega t-ikr}$, respectively. The sign of the diagram $(-1)^n$ is determined by the number of interactions on the bra side of the density matrix.

Pump-probe spectroscopy

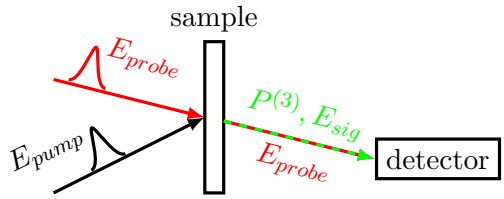

Figure 3.3: Schematic sketch of a pump-probe set-up. The pump pulse interacts with the sample before the probe pulse. The signal field E_{sig} is emitted in the direction of the probe pulse, thus the signal is self-heterodyned on the detector with the probe pulse acting as the local oscillator pulse.

In order to measure third-order nonlinear response functions, in general a pulse sequence with three light-matter interactions is required. Nonlinear pump-probe spectroscopy utilizes the simplest arrangement, where only two pulses are needed and the emitted signal field E_{sig} is detected in the same direction as the probe pulse E_{pr} (self-heterodyned detection). A schematic sketch is shown in Fig. 3.3, where we have two incident light fields (E_{pu} & E_{pr}) creating the third order nonlinear polarization $P^{(3)}$ in the sample. The detailed geometric setup will be described in subsection 3.2.2. The pump pulse E_{pu} interacts twice at the same time with the sample and generates a population. As a result, the wavevector of the third order nonlinear polarization is solely determined by the probe pulse[4].
Considering a simple three level system, we can draw the relevant Feynman diagrams that survive the rotating wave approximation and phase matching condition [106] (Fig. 3.4). Time ordering can only happen between the pump and probe interactions because the two pump interactions cannot be separated on their own. An interesting consequence is the appearance of additional diagrams when pump and probe pulses overlap, resulting in a phenomenon called the *coherent artifact* [118].
We now want to further discuss the Feynman diagrams shown in Fig. 3.4. For the diagrams on the left hand side, the two interactions with the pump pulse take the system into the first excited state $|1\rangle\langle 1|$ on both the ket and bra side of the density matrix. In other words, a diagonal density matrix is created with a probability proportional to the transition dipole moment squared ($\rho_{11}(0) \propto \mu_{10}^2$). The interaction with the probe pulse de-excites the density matrix and an off diagonal element ρ_{10} is created, hence the two diagrams describe stimulated emission. With the ρ_{10} matrix evolving in time:

$$\rho_{10}(t_3) \propto \mu_{10}^3 e^{-i\frac{(\epsilon_1-\epsilon_0)}{\hbar}t_3} e^{-\Gamma t_3} \tag{3.39}$$

[4] The pump pulse can only interact twice with the sample when it interacts with wavevectors $+k_{pump}$ and $-k_{pump}$. As a reminder, the real electrical field $E(t) = 2E_0(t) \cdot cos(\omega t - kr)$ can be separated into positive and negative frequencies $E(t) = E_0(t) \cdot (e^{-i\omega t+ikr} + e^{+i\omega t-ikr})$.

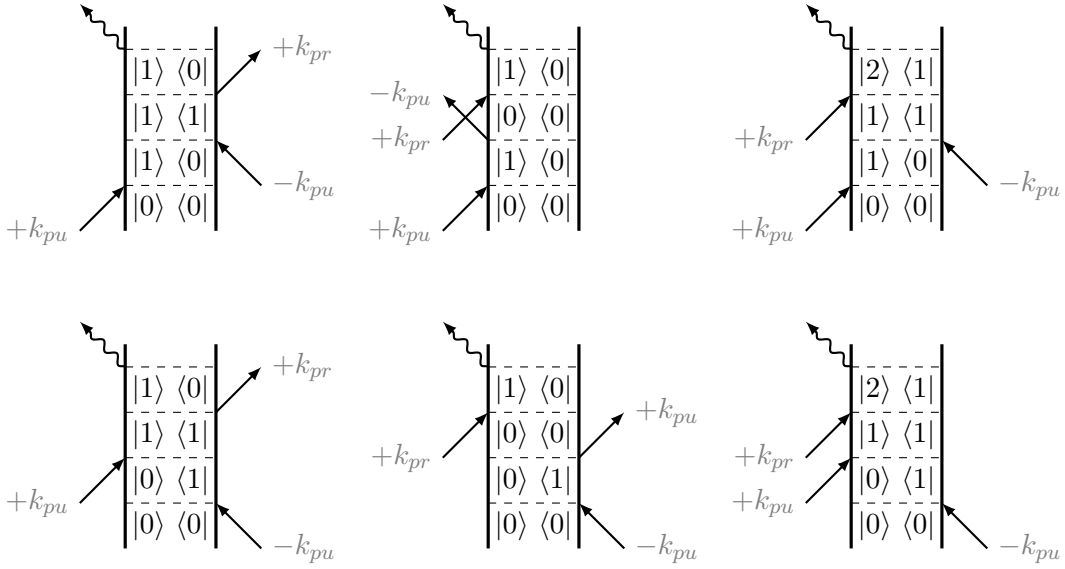

Figure 3.4: The six relevant Feynman diagrams for the third order nonlinear polarization of a three level system in a pump-probe setup. The two diagrams on the left hand side describe the stimulated emission (SE), the ones in the middle the ground state bleach (GSB) and the two on the right the excited state absorption (ESA).

we write the third order response function as:

$$R^{(3)}_{SE}(t_3, t_2, t_1) \propto \frac{i}{\hbar^3}\mu_{10}^4 e^{-i\frac{(\epsilon_1-\epsilon_0)}{\hbar}t_3} e^{-\Gamma t_3} \ . \tag{3.40}$$

The subscript *SE* denotes stimulated emission and $\epsilon_1 - \epsilon_2$ is the energy difference between the ground state and the first excited state, hence $(\epsilon_1-\epsilon_0)/\hbar$ describes the frequency ω_{10}. Eqn. 3.39 and Eqn. 3.40 do not depend on t_1 and t_2 as we assume the pump pulse to be short compared to the dephasing rate of the coherence ρ_{10}, described by the phenomenological dampening constant Γ.[5] Note that both diagrams have the same response function due to the assumption that the two pump pulse interactions at t_1 and t_2 are inseparable in time. The two diagrams in the middle describe ground state bleaching (GSB). After the second interaction with the pump pulse the system again ends up in the ground state $|0\rangle\langle 0|$. After the final interaction with the probe pulse, the density matrix ends up in the same state as for the two diagrams describing stimulated emission, consequently the response function is the same:

$$R^{(3)}_{GSB}(t_3, t_2, t_1) = R^{(3)}_{SE}(t_3, t_2, t_1) \ . \tag{3.42}$$

For the two diagrams on the right hand side, things change. After the pump pulse has created a population state $|1\rangle\langle 1|$, the interaction with the probe pulse generates a ρ_{21}

[5]

$$\begin{aligned} \Gamma_{ii} &= 1/T_1 \equiv \text{relaxation rate for state i} \\ \Gamma_{ij} &= 1/T_2 \equiv \text{dephasing rate for coherence } \rho_{\text{ij}} \\ 1/T_2 &= 1/2T_1 + 1/T_2^* \end{aligned} \tag{3.41}$$

A more sophisticated treatment, the Brownian oscillator model, is described in detail in [119, 120]

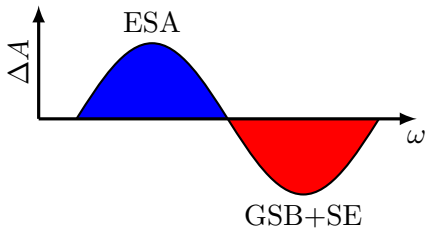

Figure 3.5: Schematic depiction of a measured absorption spectrum for the third order response functions discussed in this section.

coherence and thus the two diagrams describe the excited state absorption (ESA) with:

$$\rho^{(3)}(t_3) \propto -\mu_{10}^2 \mu_{21} e^{-i\frac{(\epsilon_2-\epsilon_1)}{\hbar}t_3} e^{-\Gamma t_3} \tag{3.43}$$

and:

$$R_{ESA}^{(3)}(t_3,t_2,t_1) \propto -\frac{i}{\hbar^2}\mu_{10}^2\mu_{21}^2 e^{-i\frac{(\epsilon_2-\epsilon_1)}{\hbar}t_3} e^{-\Gamma t_3} \ . \tag{3.44}$$

We can now pick up Fig. 3.1 again, which depicts the ground state bleach (solid blue arrow) and the stimulated emission (dashed blue arrow) between the ground state (v = 0) and first excited state (v = 1), as well as the excited state absorption between v = 1 and v = 2. A schematic depiction of a measured absorption spectrum (frequency resolved) is shown in Fig. 3.5. Since absorbance changes ΔA are measured (Eqn. 3.50 in subsection 3.2.2), the ESA appears as a positive absorption feature (blue) and is red-shifted in respect to the negative signal of the GSB & SE (red) due to the anharmonicity of the potential. Although there are 2 mechanisms (GSB & SE) contributing to the bleaching signal and only one (ESA) that contributes to the enhanced absorption signal, both features will have the same amplitude in an harmonic approximation, as the transition dipoles scale as $\mu_{12}^2 = 2\mu_{01}^2$.

Three Pulse Photon Echo Spectroscopy

Three pulse photon echo spectroscopy is a suitable method to obtain two dimensional spectra that contain additional information compared to the absorbance changes measured with a simple pump-probe set-up. In fact, a three pulse photon echo experiment is the most complete measurement of the third order response functions using $\chi^{(3)}$ processes. The trade-off however, comes with the experimental challenges that arise from the generally more complex pulse sequences and various time delays[6] between the pulses. A geometric realization of such an experiment is discussed in detail in subsection 3.2.3. It is also possible to obtain two-dimensional spectra from a pump-probe geometry, requiring phase cycling to remove the background contributions from the signal [121]. For the sake of simplicity we rely here on a schematic sketch similar to Fig. 3.3 to explain the concepts.
In Fig. 3.6 the first pulse k_1 generates a coherence that evolves freely during the time interval $\tau = \tau_i - \tau_j$ and decays with a characteristic dephasing time. A second pulse k_2 creates a population state that evolves freely in the time interval T. The third pulse k_3 generates another coherence state an the resulting third order polarization is the source for the emitted signal field in the phase matching direction $-k_1 + k_2 + k_3$. The crucial difference to pump-probe spectroscopy is the control over the time delay between the first two interactions that now arise from different pulses rather than from one pulse alone. However, the

[6] In 2D-IR spectroscopy, the time delays usually are expressed as $t_1 = \tau$, $t_2 = T$ and $t_3 = t$.

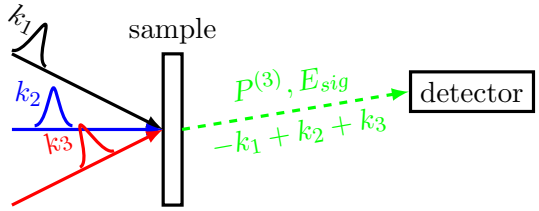

Figure 3.6: Schematic sketch of a three pulse photon echo experiment.

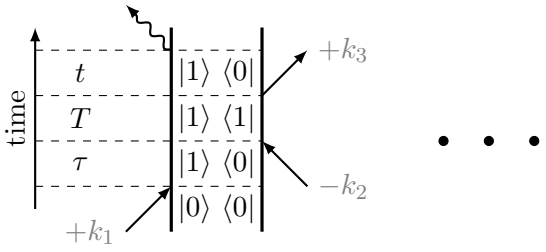

Figure 3.7: Example of a Feynman diagram for the three pulse photon echo setup. The same set of diagrams can be used as in Fig. 3.4.

relevant response functions can be described with the same set of Feynman diagrams as in Fig. 3.4. We simply change the wavevectors to k_1, k_2, k_3 and indicate that we have control over all time delays τ, T, t.
Two-dimensional correlation plots are retrieved by Fourier-transforms over the coherence time delays τ and t resulting in the excitation frequency axis ω_1 and the detection frequency axis ω_3, respectively (applying the semi-impulsive limit):

$$\begin{aligned} S(\omega_1, T, \omega_3) &= \int_0^\infty \int_0^\infty S(\tau, T, t) e^{i\omega_3 t} e^{i\omega_1 \tau} \mathrm{d}t\mathrm{d}\tau \\ &= \int_0^\infty \int_0^\infty \sum_n i R_n(\tau, T, t) e^{i\omega_3 t} e^{i\omega_1 \tau} \mathrm{d}t\mathrm{d}\tau \ . \end{aligned} \tag{3.45}$$

Scanning the waiting time T leads to a sequence of two-dimensional spectra. One should note that these so-called absorptive 2D-spectra $S(\omega_1, T, \omega_2)$ are a representation where rephasing and non-rephasing terms are added [106]:

$$S(\omega_1, T, \omega_3) = \mathbb{R}\left\{ i \left(\sum_{n=1}^{3} R_n(-\omega_1, T, \omega_3) + \sum_{n=4}^{6} R_n(+\omega_1, T, \omega_3) \right) \right\} \ . \tag{3.46}$$

We will use the level scheme for two coupled oscillators shown in Fig. 3.8 to construct an exemplary 2D-spectrum.
We first treat the oscillators independently. In both cases, the ground state bleach (solid red arrows) and the stimulated emission (dashed red arrows) between the ground and first excited state of the respective oscillator will cause a bleaching feature in the absorptive spectrum. With the frequency being the same for both the excitation and detection interactions, the positive bleaching feature[7] (peaks 2+6 & 4+8) will appear on the diagonal

[7] By convention, the sign of pump-probe and 2D-IR spectroscopy is opposite. For the sake of simplicity, 2D-signals in the following chapters will be explained with pump-probe notation, e.g. GSB & SE as negative absorbance changes and ESA as positive absorption change.

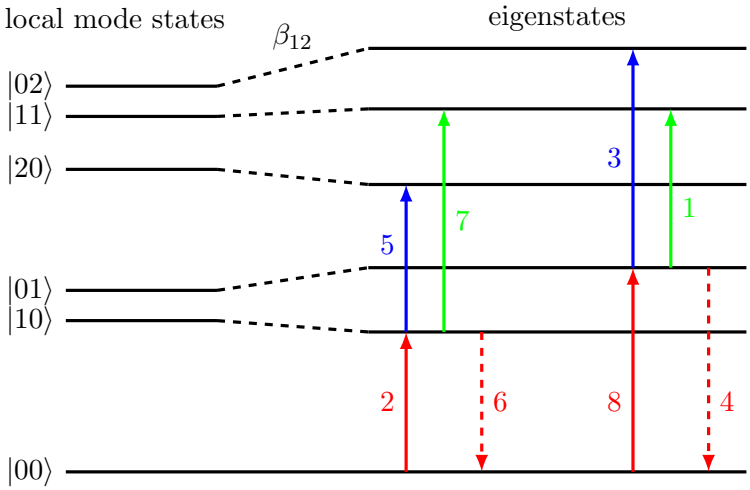

Figure 3.8: Level scheme of two coupled oscillators based on [106]. The ladder diagram shows how the energy of the states (local modes) is affected by the coupling β_{12} between the two oscillators. The energy of each state will be shifted to a new value (eigenstates). In relation to Fig. 3.1 all dipole-allowed transitions for two light interactions are shown by colored arrows. Solid and dashed red arrows depict the ground state bleach and stimulated emission between the ground and first excited state for each respective oscillator. Blue arrows indicate the absorption from the first excited state into the second excited state and green arrows show the absorption from the first excited state into a combination band that arises from the coupling of the two oscillators. Based on this level scheme, an exemplary 2D-IR spectrum is constructed in Fig. 3.9. Numbers labeling the different transitions correspond to the absorption features they cause in the 2D-IR spectrum shown in Fig. 3.9.

at the resonance frequency ω_{01} of the v = 0 to 1 transition for the respective oscillator. The excited state absorption will show up as a negative absorption feature in the spectrum (peaks 5 & 3). The excitation frequency is the same as before but the detection frequency equals now the resonance frequency ω_{12} of the v = 1 to 2 transition. For an anharmonic potential, as shown in Fig. 3.1 with $\omega_{01} > \omega_{12}$, this results in a red shift of the ESA in respect to the bleaching feature and is referred to as *diagonal anharmonicity*.
For coupled oscillators, off-diagonal pairs of cross-peaks (1,2 & 7,8) will appear. In the limit of a bilinear coupling, the frequency splitting of a pair of cross-peaks is a direct measure of the coupling strength β_{12} (cf. Eqn. 3.8) and is referred to as the *off-diagonal anharmonicity*. Further, two-dimensional spectra allow for direct interpretation of the lineshapes.
If we think of molecules in a sample that all experience a slightly different local environment, their vibrational potentials will be deformed differently and hence their vibrational frequency changes differently. At any given time we will have a distribution of transition frequencies as long as the molecules evolve slower than the time scale of the 2D-IR pulse sequence (slow modulation limit). Such distributions of frequencies result in elongated peaks along the diagonal (peaks 3 & 4+8) and one refers to them as inhomogeneously broadened. If the vibrational potentials of the molecules are not influenced by the environment, or the molecules evolve faster than the time scale of the 2D-IR pulse sequence (fast modulation limit) one would measure round and upright absorption features (peaks 5 & 2+6). These peaks are homogeneously broadened and their width is determined by the vibrational life-

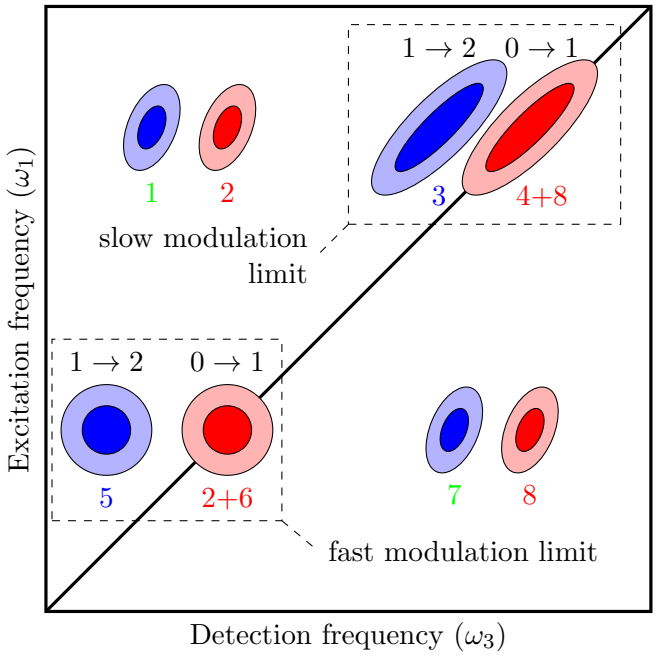

Figure 3.9: Exemplary 2D-IR spectrum constructed for the two coupled oscillators shown in the level scheme in Fig. 3.8. The ground state bleach and stimulated emission between the v = 0 to 1 transition of the respective oscillators will appear as bleaching features on the diagonal of the 2D-IR spectrum with $\omega_1 = \omega_3$. In respect to the bleaching feature, the excited state absorption will be shifted in detection frequency ω_3 due to the anharmonicity of the vibrational potential (cf. 3.1). Off-diagonal cross-peaks will appear due to the coupling β_{12} of the two oscillators.

time.

In reality, one typically measures absorption/emission features with a mixture of both broadening mechanisms. If slow and fast time scales are clearly separated, then the diagonal width represents the total linewidth and the homogeneous linewidth equals the anti-diagonal width.

Access to lineshapes and cross peaks makes 2D-IR spectroscopy an excellent tool to study structural and chemical dynamics of the system under investigation. If we initially would measure an inhomogeneous distribution of frequencies, the movement of molecules in the vicinity of the reporter groups will influence their vibrational potential and alter the observed distribution of frequencies over time. In other words the memory of the inhomogeneous distribution of frequencies gets blurred and the initially elongated absorption peaks will get more and more round and upright over time (cf. subsection 3.1.2, *spectral diffusion*) [122].

If we now consider molecules that can exist in two structures, we could measure their interconversion rate. At early waiting times T we would only measure the pairs of diagonal peaks created by each structure of the molecule. With increasing waiting time T, cross peaks will appear according to molecules that change from structure A to B. This process is called *chemical exchange* and the exchange rates can be directly read from the size and growth of the cross peaks [123].

3.2 Experimental

Parametric frequency conversion has become a standard tool to generate intense ultrashort mid-infrared (mid-IR) pulses [124]. This chapter focuses on the generation and implementation of such pulses in the experiment.

3.2.1 Generation of Femtosecond Mid-Infrared Pulses

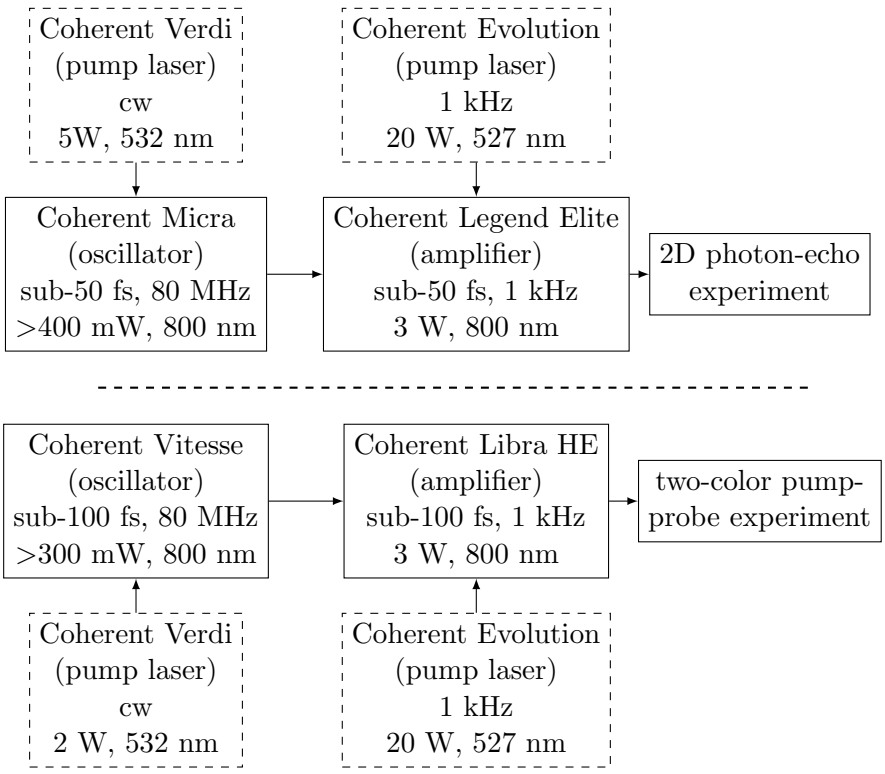

Figure 3.10: Key features of the commercial Ti:Sapphire laser systems used in the 2D-IR (upper panel) and the two-color pump-probe experiment (lower panel).

To generate intense femtosecond mid-IR pulses, home-built optical parametric amplifiers (OPAs) are driven by commercial titanium-sapphire (Ti:Sapphire/Ti:Al_2O_3) based laser systems. In our experiments, such systems reliably provide 40-60 fs pulses with high average power ($\sim$3 W) and a central wavelength of 800 nm [125, 126].
Fig. 3.10 shows a schematic sketch of the two laser systems used in this work. Because of their similar technical design, the mechanisms and concepts will be briefly explained using the upper scheme.
The Coherent Micra oscillator is pumped by a continuous wave (cw), frequency doubled Nd:YVO_4 (Vanadate) laser (Coherent Verdi). The Verdi output pumps a Ti:Sapphire crystal placed as the gain medium in the linear oscillator cavity. Passive mode-locking is achieved with the help of an optical Kerr lens that only forms upon arrival of mode-locked light pulses due to their high peak intensities. This process narrows the beam diameter of the mode-locked light with respect to cw light, resulting in the formation of a stable femtosecond pulse train. The Coherent Micra typically emits sub-50 fs, 800 nm pulses at a repetition

rate of 80 MHz and an average power that exceeds 400 mW [127].
In the chirped pulse regenerative amplifier (CPA) unit (Coherent Legend), the seed pulses first receive a positive chirp from a combination of a grating with refocusing optics elongating the pulse duration to roughly 400 ps. A first Pockels cell, that effectively acts as a $\lambda/4$ wave-plate, is used to couple a single seed pulse into the cavity of the amplifier. Here a Ti:Sapphire crystal is pumped by a Q-switched frequency doubled Nd:YLF laser (Coherent Evolution) that operates with an average power of 20 W at a repetition rate of 1 kHz. After 10-15 round trips in the resonator the seed pulse has experienced a gain of more than 10^6 and is coupled out into the compressor by a second Pockels cell. Reversing the action of the stretcher, the pulse is re-compressed close to its original duration. The CPA unit typically emits sub-50 fs, 800 nm pulses with a pulse energy of more than 3 mJ at a repetition rate of 1 kHz [125].

To generate pulses suitable for nonlinear spectroscopy in the mid-IR spectral range, the Ti:Sapphire output has to be transformed by parametric down-conversion. This was realized with help of optical parametric amplifiers. A schematic sketch of the OPAs used in the experiments is shown in Fig. 3.11.
First, roughly 1 % of the 800 nm input is used to generate a super-continuum in a thin (1 mm) sapphire (Al_2O_3) plate. The continuum generation is the result of self-phase modulation (SPM) originating from the nonlinear refractive index focusing the light (Kerr effect):

$$n(t) = n_0 + n_2 I(t) \ , \tag{3.47}$$

with the linear refractive index n_0, the nonlinear refractive index n_2 and the optical intensity $I(t)$. The pulse witnesses a phase shift according to its temporal intensity profile:

$$\phi(t) = \omega_0 t - \frac{\omega_0}{c_0} n(t) L = \omega_0 t - \frac{\omega_0}{c_0} n_0 L - \frac{\omega_0}{c_0} n_2 L I(t) \ , \tag{3.48}$$

where ω_o is the carrier frequency, c_0 the velocity of light in vacuum and L the thickness of the medium. The instantaneous frequency is the time derivative of the phase $\phi(t)$:

$$\omega(t) = -\frac{d\phi(t)}{dt} = \omega_0 - \frac{\omega_0 n_2 L}{c_0} \frac{dI}{dt} = \omega_0 \left(1 - \frac{n_2 L}{c_0} \frac{dI}{dt} \right) . \tag{3.49}$$

Eqn. 3.49 shows that the instantaneous carrier frequency of the pulse changes over time, red-shifting the leading edge of the pulse ($^{dI}/_{dt} > 0$) for $n_2 > 0$ and blue-shifting the tail of the pulse ($^{dI}/_{dt} < 0$). This leads to a spectrum that spans from the visible (down to ~ 0.4 μm) to the near infrared (up to ~ 1.5 μm) when generated with sub-50 fs 800 nm pulses [128].
The white light passes a long-pass filter and is focused onto a 4 mm BBO crystal acting as a seed pulse for a first amplification process (type II phase-matching). 800 nm pump pulses ($\sim$ 9 % of the pump input) are overlapped in space and time with the seed pulse leading to an amplification of the signal and the generation of a so called "idler" frequency at $\omega_3 = \omega_1 - \omega_2$ [129]. The signal frequency is retro-reflected onto the BBO crystal for a second pass and again overlapped with 800 nm pump pulses ($\sim$ 90 % of the pump input) in space and time. After the second amplification, the intense signal and idler pulses (pulse energy 120 μJ) with wavelengths between 1200-1600 nm and 1600-2400 nm are used for difference-frequency mixing in either GaSe (type II, 0.5-1 mm, 1000-2500 cm^{-1}) or $AgGaS_2$ (type I, 0.5-1 mm, 2500-4000 cm^{-1}). This setup leads to mid-IR pulses with energies of 1-3 μJ

and 60-200 fs duration, depending on the output frequencies. In the two-color pump-probe setup, two independent OPA sources are implemented for the generation of independently tunable pump and probe pulses.
The optical parametric amplifier used in the 2D-IR experiment has an additional third amplification step in a 2 mm BBO crystal, ramping up signal and idler pulses to roughly 350 μJ. Subsequent difference-frequency generation in GaSe leads to mid-IR pulses with 6-9 μJ and $\sim$100 fs duration tunable between 1000-1300 cm^{-1}.

3.2.2 Two-Color Pump-Probe Setup

Two-color pump-probe spectroscopy is a powerful tool to monitor dynamic properties of molecular systems. Its great tunability and excellent time resolution provide the necessary means to follow energy relaxation and redistribution processes in real time [26, 130].
The setup of the experiment is depicted in Fig. 3.12. Pump pulses first pass a chopper running at half the repetition rate of the pulse train (500 Hz) before they are delayed by a movable mirror mount. The pump pulses are then focused (focal diameter $\sim$100 μm) into the sample volume and blocked with a beam dump afterwards.
Probe pulses initially double pass a BaF_2 wedge resulting in two identical replica that are attenuated by a factor of 100 compared to the incident pulse. We call these replicas probe and reference pulses. The probe pulse is focused into the sample and interacts with the volume excited by the pump pulse. The reference pulse is horizontally displaced and focused into the sample outside of the excitation volume. Transmitted probe and reference pulses are dispersed with help of a grating and detected with a 64-pixel mercury-cadmium-telluride (MCT) double array detector (spectral resolution 2 cm^{-1}).
The absorbance change ΔA, as a function of the probe frequency ω_{pr} and the time delay τ between pump (chopped at 500 Hz) and probe pulses, is given by:

$$\Delta A(\omega_{pr},\tau) = -log\left(\frac{I^{pr}_{pump}(\omega_{pr},\tau)}{I^{pr}_{0}(\omega_{pr},\tau)}\cdot\frac{I^{ref}_{0}(\omega_{pr},\tau)}{I^{ref}_{pump}(\omega_{pr},\tau)}\right) . \tag{3.50}$$

Here I_{pump} and I_0 are the intensities with and without pump excitation for the probe pulses (pr) and the reference pulses (ref), respectively. The reference beam allows for shot to shot referencing of laser intensity fluctuations, increasing the signal to noise ratio by almost an order of magnitude.
The signal can also be detected in a polarization resolved way by adding a $\lambda/2$-wave plate to the probe beam, setting its polarization under an angle of 45° with respect to the pump beam. A polarizer in front of the monochromator is then used to select the desired polarization of the probe beam. This allows to calculate the pump-probe anisotropy:

$$r(\tau) = \frac{\Delta A_{\parallel}(\tau) - \Delta A_{\perp}(\tau)}{\Delta A_{\parallel}(\tau) + 2\cdot\Delta A_{\perp}(\tau)} \tag{3.51}$$

and the isotropic signal:

$$\Delta A_{iso}(\tau) = \frac{\Delta A_{\parallel}(\tau) + 2\cdot\Delta A_{\perp}(\tau)}{3} , \tag{3.52}$$

where $\Delta A_{\parallel}(\tau)$ and $\Delta A_{\perp}(\tau)$ denote absorbance changes with parallel and perpendicular polarization between pump and probe pulses, respectively.
In this setup, the time resolution is determined by the cross-correlation (XC) between

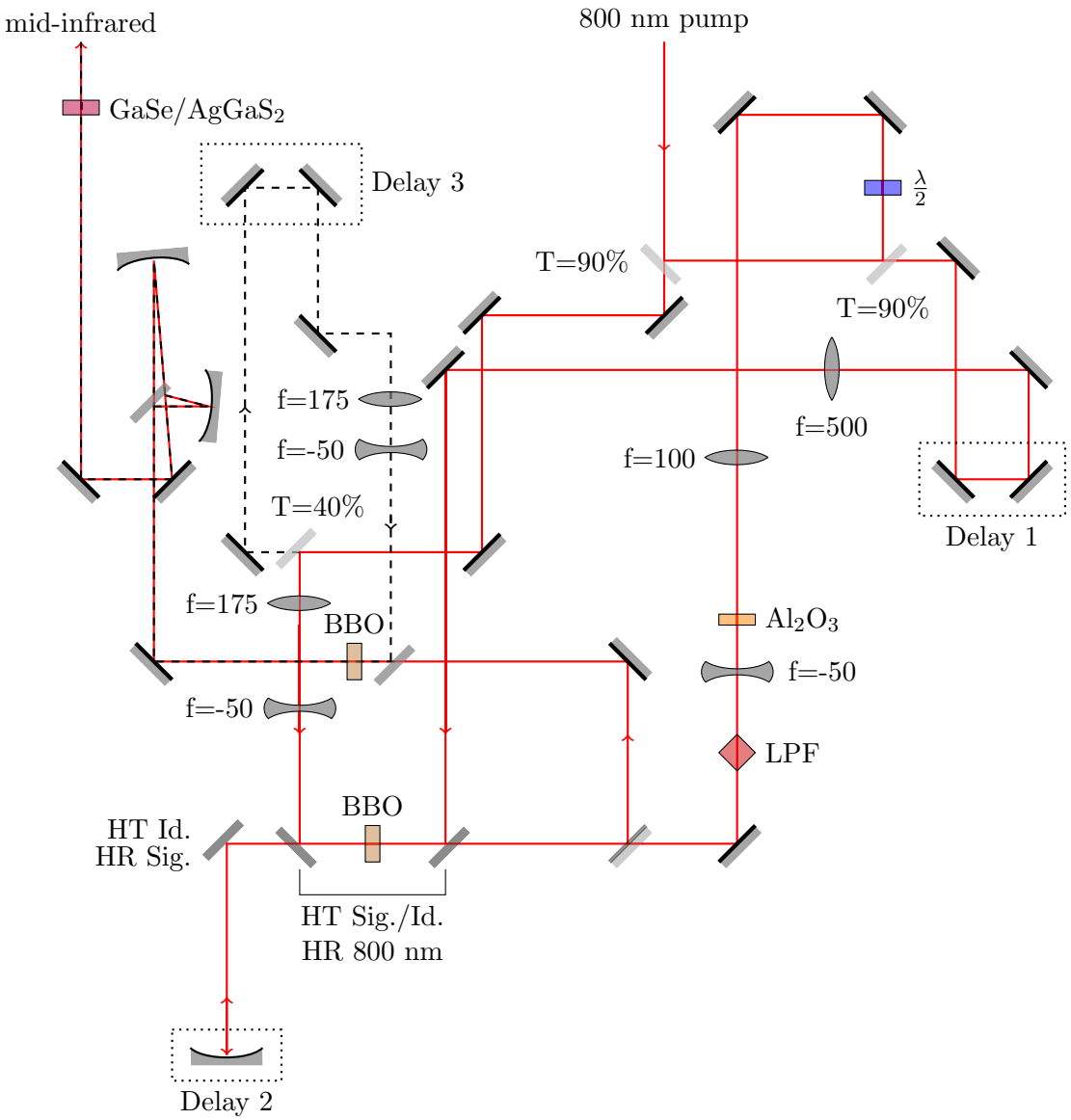

Figure 3.11: Optical parametric amplifier (OPA) setup used in the two-color pump-probe experiment. Initial white light generation in a 1 mm sapphire (Al_2O_3) plate and two subsequent amplification steps in a 4 mm BBO crystal lead to intense (>120 μJ) signal and idler radiation with wavelengths between 1200-1600 nm and 1600-2400 nm, respectively. Difference-frequency generation in GaSe or $AgGaS_2$ leads to femtosecond mid-IR pulses with energies of 1-3 μJ. Frequency tunability is realized by tilting the birefringent BBO and GaSe/$AgGaS_2$ crystals. The optical parametric amplifier used in the 2D-IR experiment has a third amplification step (black dotted light path) leading to signal and idler radiation on the order of 350 μJ. Difference-frequency generation in GaSe results in ∼100 fs mid-IR pulses with energies of 6-9 μJ tunable between 1000-1300 cm^{-1}.
Abbreviations: T – transmission, HT/HR – high transmission/ high reflection, LPF – long-pass filter.

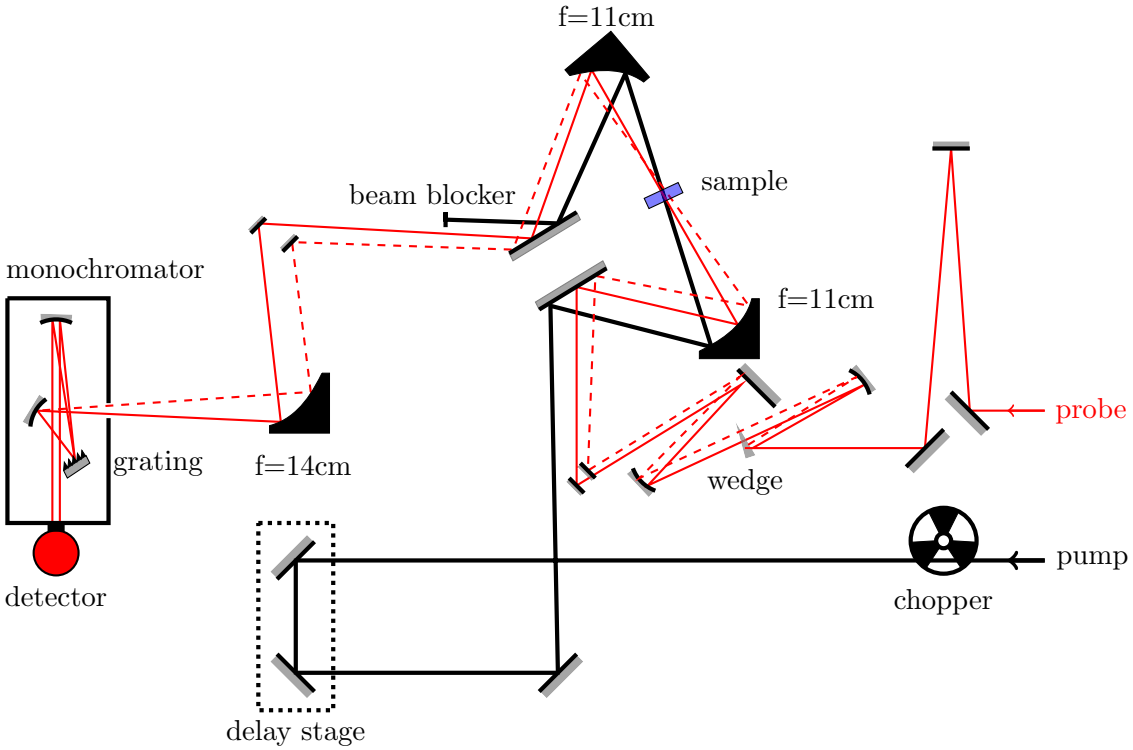

Figure 3.12: Schematic representation of the two-color pump-probe setup, driven by two independently tunable OPAs for pump and probe pulses. Pump pulses (solid black line) are chopped at 500 Hz and delayed in time by a translation stage that can produce delays greater than 100 ps between pump and probe pulses. Pump pulses are then focused into the sample and blocked afterwards. In a separate arm of the setup, a BaF_2 wedge is used to generate two identical attenuated replicas of the input pulse from the second OPA, called probe and reference. Probe pulses (solid red line) are focused into the excitation volume and spectrally dispersed onto a 64 pixel MCT-array detector to record pump induced absorbance changes. Reference pulses (dashed red line) are horizontally displaced and transmit the sample outside of the excitation volume. They are spectrally dispersed onto a second array of the detector to correct for intensity fluctuations. The experimental setup is enclosed by Plexiglas and can be purged with gaseous nitrogen to eliminate signal contributions due to atmospheric water.

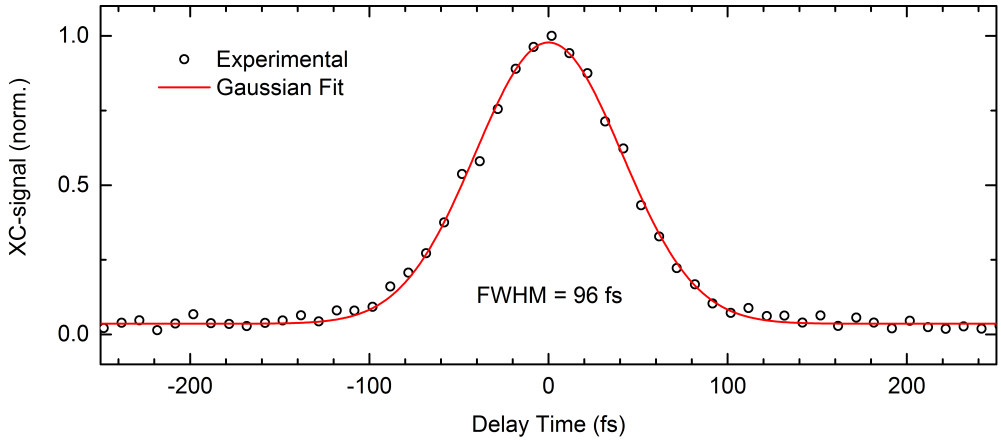

Figure 3.13: Measured cross-correlation signal of pump and probe pulses centered around 2100 cm^{-1} and 3400 cm^{-1}, respectively. The experimental data (open circles) can be simulated by a Gaussian pulse shape with a full width at half maximum (Δt) of 96 fs (red line).

pump and probe pulses. The XC is measured with help of the two-photon absorption nonlinearity in indium arsenide (band gap $\approx$ 2903 cm^{-1} at T = 300 K) or germanium (band gap $\approx$ 5323 cm^{-1} at T = 300 K). After proper attenuation of the intense pump pulse with copper meshes, one measures a Gaussian XC function as is shown in Fig. 3.13. The measured cross-correlation signal I_{XC} is of time-integrated second order with intensity:

$$\begin{aligned} I_{XC}(\tau) &\propto \int_{-\infty}^{+\infty} |E_{pump}(t) \cdot E_{probe}(t-\tau)|^2 \mathrm{d}t \\ &= \int_{-\infty}^{+\infty} I_{pump}(t) \cdot I_{probe}(t-\tau) \mathrm{d}t \ , \end{aligned} \tag{3.53}$$

where $E_{pump/probe}$ are the electric fields and $I_{pump/probe}$ the intensities of the pump and probe pulses, respectively. In this measurement procedure, any phase information is lost. Assuming equal pulse widths for pump and probe pulses one can determine the time resolution from a Gaussian fit of the XC-signal.
The data in Fig. 3.13 display a measured XC-signal with the full width at half maximum (FWHM) of the Gaussian fit of 96 fs − corresponding to a pulse duration of ∼68 fs after deconvolution.

3.2.3 Heterodyne Detected Photon-Echo Setup

Two-dimensional infrared (2D-IR) spectroscopy spreads the nonlinear vibrational spectrum over two frequency axes, allowing the interpretation of time-dependent environmental influences on lineshapes, such as spectral diffusion or the coupling and orientation of vibrational modes via cross-peaks.
In this work, a specially tailored four pulse sequence (cf. Fig. 3.15) is used to induce a third-order nonlinear response in the sample, which allows for background free detection of photon echoes.
The experimental setup is sketched in Fig. 3.14. Initially, the OPA input pulse is split

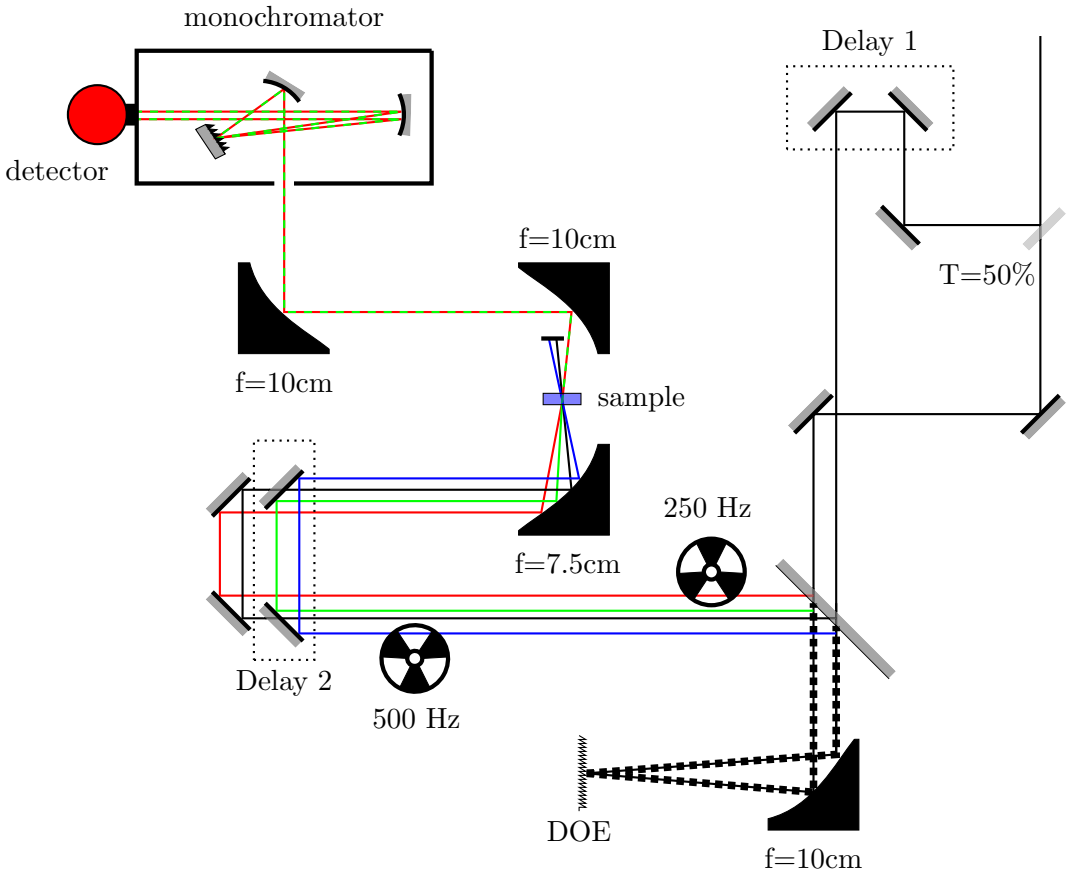

Figure 3.14: Schematic representation of the heterodyne detected photon-echo setup. OPA input pulses are first split 50 : 50 by a beam-splitter. Both of the pulse replica are focused on a diffractive optic element (DOE), while one of them experiences a time delay T. The retro-reflected +1 and -1 diffraction-order pulses of each incident pulse form the so-called BOXCARS beam-geometry and travel collinearly until they are focused into the sample with help of an off-axis parabolic mirror (for details cf. subsection 3.2.3 and cf. Fig 3.15). The signal field is heterodyned by a local oscillator pulse and recorded with a 64 pixel mercury cadmium telluride detector array.

with a 50 : 50 ratio into two pulses A and B with the help of a beam-splitter. Pulse A is delayed by a translation stage before being focused onto a diffractive optic element (DOE), introducing a first time delay T with respect to pulse B. The waiting time T defines a time interval in which the population of the system evolves freely (cf. Fig. 3.15b). B is focused onto the DOE directly.
After interaction and retro-reflection from the DOE, the +1 and -1 diffraction order pulses of A and B are selected with help of a mirror mount. We further define the first pulse pair stemming from A as k_1 (black) and k_2 (blue) and the second pulse pair from B as k_3 (red) and k_{LO} (green). Due to the use of a DOE these pulse pairs are inherently phase-locked (passive phase stabilization) [131]. The four pulses define the corners of a square (cf. Fig. 3.15a), the so called BOXCARS beam-geometry [132].
All four pulses travel collinearly onto an off-axis parabolic mirror and are focused into the sample (focal diameter ~200 μm). Before interaction with the sample, k_2 and k_3 are

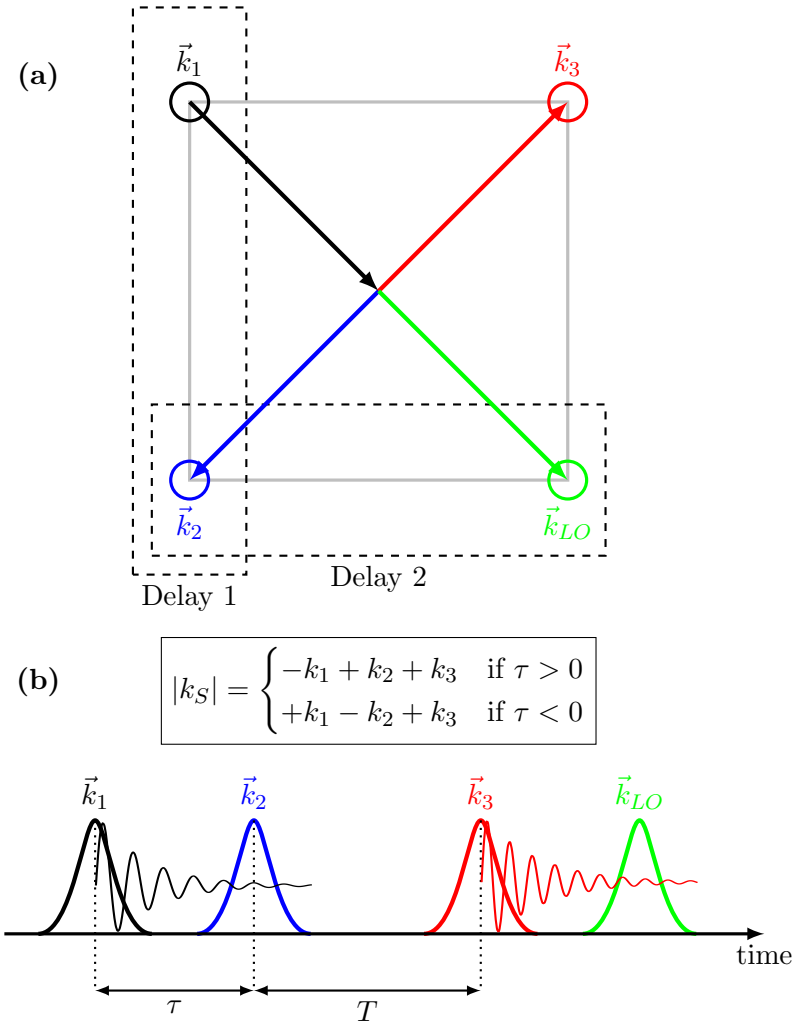

Figure 3.15: **(a)** Schematic sketch of the BOXCARS beam-geometry used in the heterodyne-detected photon-echo experiment. The four pulses ($\vec{k_1}, \vec{k_2}, \vec{k_3}, \vec{k_{LO}}$) form the corners of a square (light gray line). The pulse pair $\vec{k_1}$ and $\vec{k_2}$ experiences a first time delay Δt_1 setting the waiting time T whereas the pulse pair $\vec{k_2}$ and $\vec{k_{LO}}$ experiences a second time delay Δt_2 setting the coherence time τ in the experiment. **(b)** Typical pulse sequence used in the experiment with variable time delays τ and T. The rephasing signal contributions are measured for $\tau > 0$. Negative values of τ correspond to a change in time-ordering where $\vec{k_2}$ precedes $\vec{k_1}$ and the non-rephasing signal contributions are measured (cf. Eqn. 3.57).

chopped at 500 Hz and 250 Hz, respectively. Pulses k_2 and k_{LO} experience an additional time delay τ by a translation stage whereas k_3 is retarded by a thin (0.5 mm) zinc selenide (ZnSe) plate for a fixed time delay (t_{ref}) of approximately 2.6 ps.
The coherence time τ defines the time interval between k_1 and k_2 (cf. Fig. 3.15b). The signal is emitted in the (rephasing) phase matching direction $\vec{k}_S = -\vec{k}_1 + \vec{k}_2 + \vec{k}_3 = \vec{k}_{LO}$ so that the signal and local oscillator pulses coincide collinearly (cf. Fig. 3.15) on the detector for frequency-resolved heterodyne detection (monochromator MCT detector-array, spatial resolution 2 cm^{-1}).
The intensity I_{sig} of the interferogram between the electric fields of the signal E_{sig} and the local oscillator E_{LO} are recorded as a function of detection frequency ω_{det}:

$$I_{sig}(\omega_{det}) = |E_{LO}(\omega_{det}) + E_{sig}(\omega_{det})|^2 \ . \tag{3.54}$$

Considering that the signal field is small compared to the local oscillator, Eqn. 3.54 can be written as:

$$\begin{aligned} I_{sig}(\omega_{det}) &= |E_{LO}(\omega_{det})|^2 + 2\mathbb{R}[E^*_{LO}(\omega_{det})E_{sig}(\omega_{det})] \\ &\approx |E_{LO}(\omega_{det})|^2 + 2|E_{LO}(\omega_{det})||E_{sig}(\omega_{det})| \cdot cos(\phi_{sig} - \phi_{LO}) \ , \end{aligned} \tag{3.55}$$

meaning that the strong contribution $|E_{LO}(\omega_{det})|^2$ must be efficiently filtered out in order to retrieve the signal from the nonlinear interaction in the sample. This is done by chopping k_2 at 500 Hz and forming the differential signal of consecutive pulses so that the contribution of the local oscillator spectrum is eliminated.
A consequence of Eqn. 3.55 is the phase dependence of the retrieved signal field:

$$\begin{aligned} \Phi_{signal} - \Phi_{LO} &= (-\Phi_1 + \Phi_2) + (\Phi_3 - \Phi_{LO}) + \phi_{signal} \\ &= (-\Phi_1 + \Phi_3) + (\Phi_2 - \Phi_{LO}) + \phi_{signal} \ , \end{aligned} \tag{3.56}$$

with ϕ_{signal} being the phase related to the nonlinear response function of the system and $\Phi_{1,2,3,LO}$ being the phases of the pulses $k1$, $k2$, $k3$ and k_{LO}, respectively. This is a non-trivial problem that can be solved with different approaches [133–136]. Here we generate phase-locked pulse pairs with the DOE which then travel along very similar optical paths. Phase fluctuations between the individual pulse pairs (k_1/k_2 ; k_3/k_{LO}) before the DOE cancel, as is evident from the first line in Eqn. 3.56. A consequence of the correlated time delays used in the experiment is the elimination of the τ-dependence in the measured third order response functions:

$$\begin{aligned} R_{reph.}(\tau,T,t) &= -\frac{2i}{\hbar^3}\mu_{01}^4 \left(e^{-i\omega_{01}(t-\tau)} - e^{-i[(\omega_{01}-x)t-\omega_{01}\tau]}\right) e^{-\tau+t/2T_1} \\ &\quad e^{-T/T_1} \cdot e^{-g(\tau)+g(T)-g(t)-g(\tau+T)-g(T+t)+g(\tau+T+t)} \\ R_{non-reph.}(\tau,T,t) &= -\frac{2i}{\hbar^3}\mu_{01}^4 \left(e^{-i\omega_{01}(t+\tau)} - e^{-i[(\omega_{01}-x)t+\omega_{01}\tau]}\right) e^{-\tau+t/2T_1} \\ &\quad e^{-T/T_1} \cdot e^{-g(\tau)-g(T)-g(t)+g(\tau+T)+g(T+t)-g(\tau+T+t)} \ , \end{aligned} \tag{3.57}$$

with the anharmonicity $x = \omega_{01} - \omega_{12}$. The relative phase-shifts $-\omega\tau$ for rephasing contributions and $+\omega\tau$ for non-rephasing contributions cancel (cf. Eqn. 3.57), so that proper phase factors have to be multiplied in the evaluation procedure in order to yield correct 2D spectra.
To retrieve such phase factors, pump-probe spectra are recorded for the same waiting time

T. The 2D spectra are integrated along the excitation frequency and "fit" to the pump probe data. The retrieved phase factors can then be multiplied with the spectral interferogram in order to yield the corrected 2D spectra.
Pulse characterization is directly accessible in this passively phase locked three-pulse photon echo setup by measuring a transient grating (TG) frequency resolved optical gating (FROG) trace [137].
Here three pulses in total are required. Two of them are overlapped in time and space in a medium with a third-order nonlinearity (ZnSe) to induce a transient refractive index grating. A third pulse with variable time delay (τ) is diffracted by the induced grating. We record the intensity spectrum:

$$I_{\mathrm{FROG}}^{\mathrm{TG}}(\omega,\tau) = \left| \int_{-\infty}^{+\infty} E_1(t) E_2^*(t-\tau) E_3(t) \cdot exp(-i\omega t) \mathrm{d}t \right|^2 , \tag{3.58}$$

where E_i indicates the electric field of the i-th pulse. In this example the second pulse experiences the time delay τ. Assuming identical pulses, Eqn. 3.58 can be simplified to:

$$I_{\mathrm{FROG}}^{\mathrm{TG}}(\omega,\tau) = \left| \int_{-\infty}^{+\infty} E(t)^2 E^*(t-\tau) \cdot exp(-i\omega t) \mathrm{d}t \right|^2 . \tag{3.59}$$

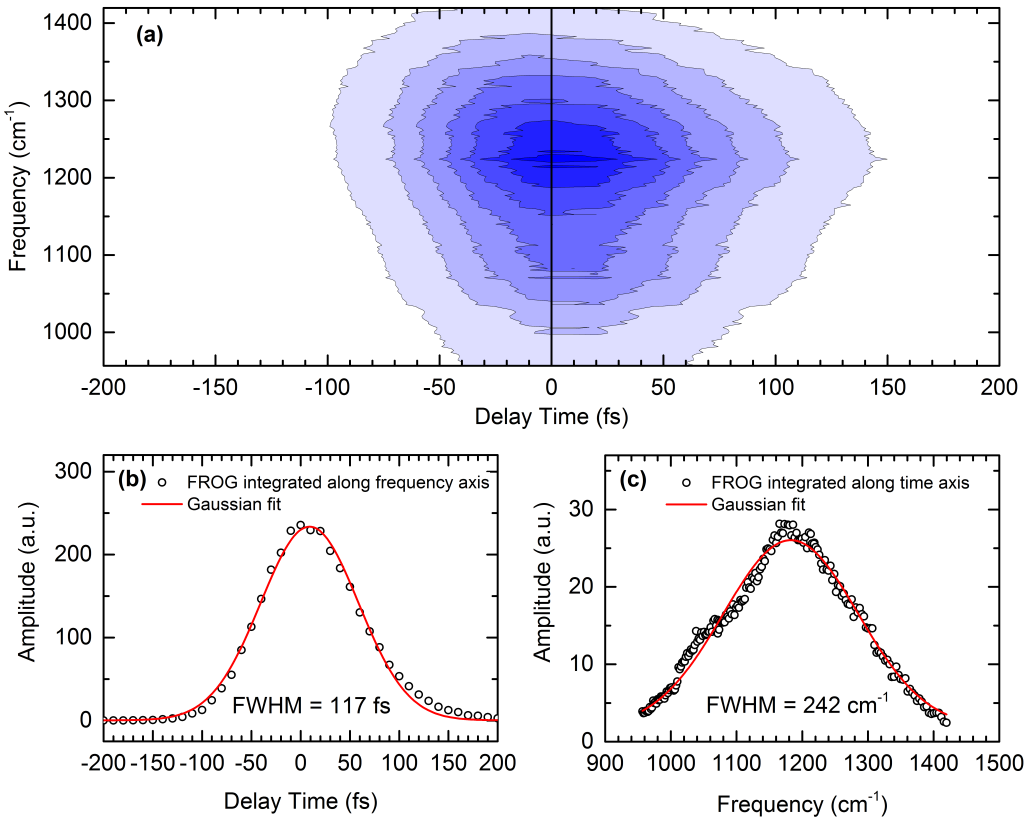

Figure 3.16: **(a)** Measured TG-FROG trace for a pulse centered around 1200 cm^{-1} used in the experiments on the hydrated excess proton samples. Vertical and horizontal cuts are taken to deduce the spectral width and pulse duration. **(b)** Gaussian fit of the vertical cut taken at 10 fs with a FWHM of 255 cm^{-1}. **(c)** Gaussian fit of the horizontal cut taken at 1228 cm^{-1} with a FWHM of 125 fs.

A TG-FROG trace measured in this setup is shown in Fig. 3.16(a). Fig. 3.16(b) and (c) display the FROG trace integrated along the frequency and time axis, respectively. The complete spectral amplitude and phase can be recovered from a FROG measurement with help of complex algorithms [137].
Assuming a Gaussian pulse shape, the pulse duration τ_p can be estimated from the spectrogram with:

$$\tau_p = \frac{\Delta t}{\sqrt{3/2}} \ . \tag{3.60}$$

For the TG-FROG shown in Fig. 3.16a we derive a Δt of 117 fs (cf. Fig. 3.16b) corresponding to a pulse duration of ∼95 fs. The time-bandwidth product is 0.69 considering the spectral width of 242 cm^{-1} (cf. Fig. 3.16c).

3.2.4 Sample Preparation

The concept of this study is based on the predominant preparation of Zundel cations in solution. In the following, the composition of the sample solutions is discussed in respect of their Eigen to Zundel ratios. Furthermore, the realization of thin samples in a nanofluidic cell will be presented.

Triflic Acid in Water/Acetonitrile Mixtures

Similar to ref [30] we performed steady state absorption measurements for triflic acid (HCF_3SO_3) in different water/acetonitrile mixtures to quantify the amount of Zundel vs. Eigen geometries in our sample solutions. Triflic acid is commercially available in its anhydrous form and thus enables the measurement of a concentration-dependent series starting with very low amounts of water. Acetonitrile is especially suitable as a solvent. It mixes in any proportion with water to form a highly polar solution and mineral acids completely dissociate even for small acid:water ratios [30, 138–140].

$$AH + (H_2O)_n \rightleftharpoons A^- + (H_2O)_nH^+ \tag{3.61}$$

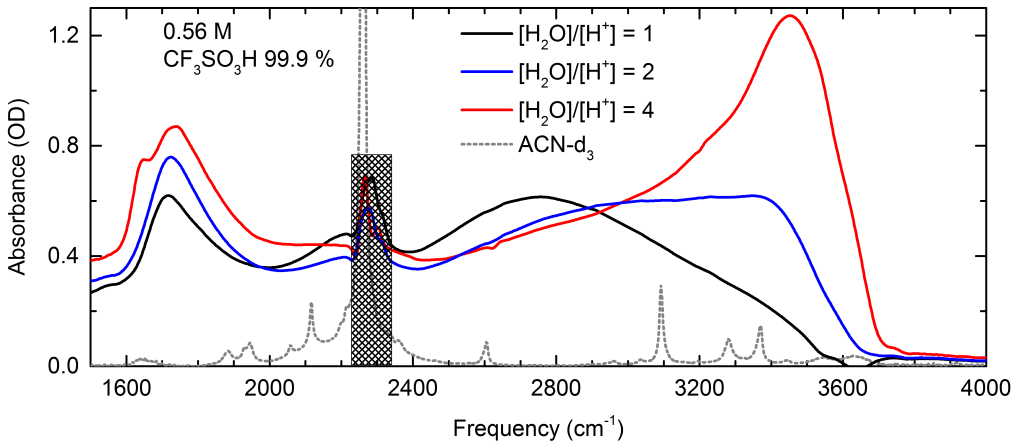

Figure 3.17: Steady state absorption spectra of 0.56 M triflic acid (CF_3SO_3H) diluted in water/acetonitrile mixtures for 1:1, 1:2 and 1:4 ratios of H^+:H_2O. The deuterated acetonitrile ($ACN\text{-}d_3$) background has been subtracted (gray dashed line).

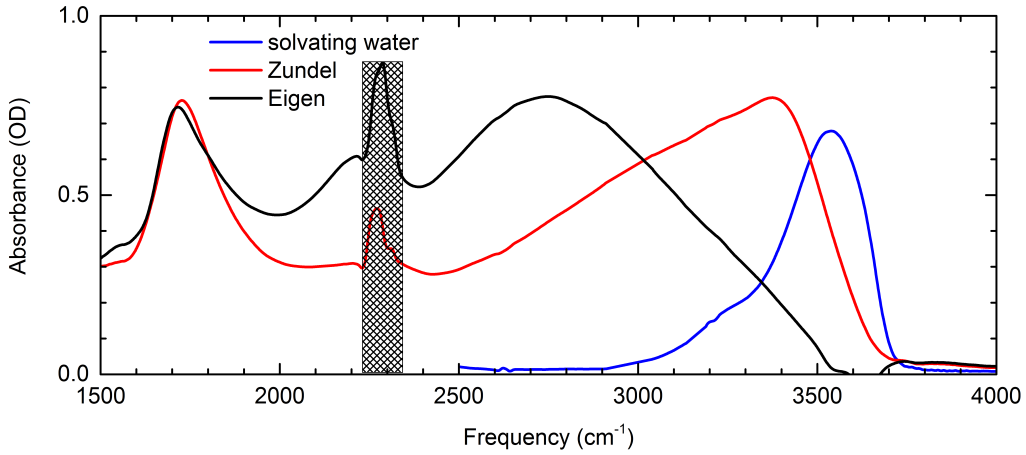

Figure 3.18: Steady state absorption spectra of the Eigen core (black line) and the Zundel cation in acetonitrile (red line) derived from the 1:1 and 1:2 H^+:H_2O solutions. The contribution of water molecules in the first solvation shell of the Zundel cation is shown in blue.

The water molecules in the mixture will be protonated over acetonitrile upon acid dissociation due to the stronger Brønsted basicity of H_2O compared to CH_3CN [141, 142].
Steady state absorption spectra for three H^+:H_2O ratios (1:1, 1:2, 1:4) are shown in Fig. 3.17, where the deuterated acetonitrile (ACN-d_3) background has been carefully subtracted (gray dashed line in Fig. 3.17). According to ref. [30], higher H^+:H_2O ratios do not change the observed spectral features of the hydrated proton up to 10 M of water and thus are not considered in this analysis. The acid concentration was kept constant at 0.56 M.
For a 1:1 ratio of protons and water in ACN-d_3 one expects the formation of the hydronium (H_3O^+) molecule as the water content is too low to form any larger clusters. This hydronium core forms three hydrogen bonds to ACN-d_3 molecules in its vicinity and resembles an Eigen cation, from here on referred to as an "artificial Eigen" (exchanging the three water molecules in the first hydration shell of H_3O^+ to ACN-d_3 in Fig. 2.3 on page 19).
The linear absorption of these cations is shown as the black trace in Fig. 3.17. We can identify three very broad absorption features at ∼1720 cm^{-1}, ∼2200 cm^{-1} and ∼2700 cm^{-1}. The origin of the ∼1720 cm^{-1} band remains controversial and no clear designation has been made until now. It also appears in gas phase clusters of the Eigen cation [27] but is not expected from calculations on the harmonic level. The absorption at ∼2200 cm^{-1} can be attributed to combination band of frustrated rotations of the hydronium core with the bending motions of H_3O^+ and the bending modes of the H_2O molecules in the first solvation shell [143]. McCoy et al. explained the relative strong absorption of these combination modes by a very strong non-Condon effect [144]. Further Yu and Bowman stressed the coupling of these combination bands to the asymmetric OH stretching vibrations of the hydronium core [143]. The most prominent feature of the spectrum is the broad absorption band at ∼2700 cm^{-1} that can be assigned to the symmetric and asymmetric OH stretching vibrations of H_3O^+ [27].
With the addition of another water molecule per proton (blue solid line in Fig. 3.17) a new spectral feature rises around ∼3400 cm^{-1} that can be attributed to the OH stretching vibrations of two water molecules sharing the excess proton in a Zundel configuration

Table 3.1: Abundance of H_3O^+ and $H_5O_2^+$, derived from a spectral decomposition analysis for the investigated triflic acid in water/acetonitrile mixtures [146].

H^+:H_2O	H_3O^+ (%)	$H_5O_2^+$ (%)
1:1	90 ± 5	10 ± 5
1:2	29 ± 5	71 ± 5
1:4	8 ± 5	92 ± 5

($H_5O_2^+$) [145]. Additionally, the features characteristic for the Eigen cations at ∼2200 cm^{-1} and ∼2700 cm^{-1} decrease in intensity, while the absorption at ∼1720 cm^{-1} gains intensity and shifts by about 10 cm^{-1} to higher frequencies. These changes indicate that the addition of water, after a 1:1 ratio of water and protons, causes the artificial Eigen cations to convert to Zundel cations. For the protonated water dimer, the strong absorption at ∼1730 cm^{-1} can be explained by the OH bending motion of the flanking water molecules [27, 145].
With further addition of water (cf. red line in Fig. 3.17) one starts to observe a sharp peak at ∼1630 cm^{-1} that is attributed to the OH bending vibration of water molecules in the solution that are not directly solvating the proton. Additionally, the OH stretching vibration of these molecules add to the absorption in the 3400-3500 cm^{-1} range (cf. blue line Fig. 3.18).
Compared to the absorption of water monomers in acetonitrile (cf. Fig 4.1 on page 54), one observes a red shift of the OH stretching vibrations by approximately 50 cm^{-1}. Consequently, excess water molecules in the 1:4 H^+:water solution that are not directly solvating the proton can exchange the acetonitrile molecules in the first solvation shell of the Zundel cation. The red shifted absorption indicates stronger hydrogen bonding of the Zundel solvation shell water molecules to the acetonitrile environment compared to water monomers in acetonitrile [26].

With these results and assuming that all water molecules in the 1:1 and 1:2 H^+:H_2O solutions directly solvate the proton (as H_3O^+ or $H_5O_2^+$) we can derive the characteristic absorption spectra of the Eigen core (black line in Fig. 3.18) and the Zundel cation in acetonitrile (red line in Fig. 3.18). With the species dependent spectra, we can obtain the relative abundances of Eigen and Zundel geometries in the measured acid/water mixtures diluted in ACN-d_3 applying the following equilibrium conditions:

$$\begin{aligned} AH + (H_2O)_n &\overset{K_1}{\rightleftharpoons} A^- + H_3O^+ + (H_2O)_{n-1} \overset{K_2}{\rightleftharpoons} A^- + H_5O_2^+ + (H_2O)_{n-2} \\ &\overset{K_3}{\rightleftharpoons} A^- + H_5O_2^+(H_2O) + (H_2O)_{n-3} \ . \end{aligned} \tag{3.62}$$

Here, we made use of the fact that Kalish et al. [30] showed that the proton in water/acetonitrile mixtures is preferably solvated by two water molecules even for larger water contents up to 10 M, hence further addition of water retains the Zundel motif.
The relative abundance of H_3O^+ and $H_5O_2^+$ in the investigated triflic acid in water/acetonitrile mixtures is summarized in table 3.1.

Time-Resolved Experiments

In the ultrafast pump-probe and 2D-IR experiments, several different acid/water mixtures diluted in acetonitrile were used to complement the spectroscopic method and spectral range

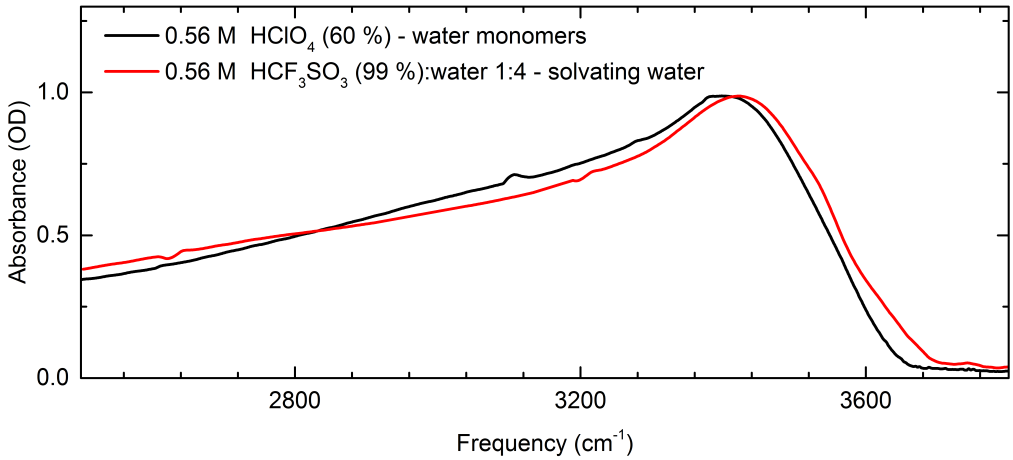

Figure 3.19: Steady state absorption spectra of 0.56 M $HClO_4$ (60-62 %) in ACN-d_3 (black line) and 0.56 M HCF_3SO_3 together with 2.24 M H_2O in ACN-d_3 (red line). Contributions of water molecules not directly solvating the proton were subtracted with a reference measurement of water monomers in acetonitrile for the $HClO_4$ spectrum and with help of the spectrum derived earlier for the water molecules in the first solvation shell of $H_5O_2^+$ for the HCF_3SO_3 spectrum, respectively.

of investigation. Triflic acid (HCF_3SO_3) was not used in the time-resolved experiments due to its inferior long time stability in the sample solutions compared to perchloric acid ($HClO_4$) or hydroiodic acid (HI).
We found that the linear absorption spectrum of 60-62 % $HClO_4$ diluted in acetonitrile (red line Fig. 3.19), which translates roughly to a 1:3.4 ratio of protons to water molecules, is extremely similar to the analyzed 1:4 triflic acid:water solution (black line Fig. 3.19). For the sake of simplicity, we have subtracted a measured reference of water monomers in acetonitrile in case of the solution containing $HClO_4$ rather than dividing it into contributions of water molecules solvating the Zundel cations and monomeric waters. Still, the similarities of both spectra are striking and we assume the same sample composition of 8 $\pm$ 5 % H_3O^+ and 92 $\pm$ 5 % $H_5O_2^+$ that we found for the 1:4 triflic acid:water mixture.
The results by Kalish et al. [30] demonstrate, that interchanging mineral acids e.g. $HClO_4$, HCl, HBr, HI, HCF_3SO_3 does not show a noticeable effect on the observed absorption spectrum, thus solutions containing HI have the same composition of Eigen and Zundel cations.
In detail, sample solutions were prepared by diluting 0.26 M $HClO_4$ (Alfa Aesar, 60-62 % wt. in H_2O) in deuterated acetonitrile (Deutero GmbH, anhydrous 99.8 %). To investigate the spectral region below 1500 cm^{-1}, we prepared sample solutions with hydroiodic acid (HI) rather than perchloric acid ($HClO_4$), to avoid strong signal contributions of the perchlorate (CLO_4^-) absorption bands in this spectral region.
0.6-1 M HI (Sigma-Aldrich, 57 % wt. in H_2O or 67 % wt. in H_2O) was diluted in acetonitrile (Alfa Aesar, anhydrous, 99.8+%) resulting in a 1:5.4 ratio of H^+:H_2O (57 %) and a 1:3.5 ratio of H^+:H_2O (67 %), respectively. As demonstrated by Kalish et al. [30], stochiometric differences in this range do not influence the absorption spectrum exhibited by the solvated protons.
For the experiments on excess protons in water, 0.6-1 M HI (Sigma-Aldrich 67 % wt. in

H_2O) was diluted in water (Acros Organics, extra pure, deionized). The strong mineral acids completely dissociate under the present conditions (cf. paragraph: "Triflic Acid in Water/Acetonitrile Mixtures"), thus the proton concentration equals the acid concentration in all our sample solutions. Sample solutions were checked before and after each time-resolved experiment to assure their chemical stability.

Sample-Holder

Working with extremely strong acids ($HClO_4$, HI) poses special demands on the materials used to store the sample solution for the duration of the experiment. Conventional and commercially available options either do not withstand the acid corrosion or do not meet the experimental requirements.
We made use of a home-made nanofluidic cell that is based on a simple concept, where two silicon-nitrite (SiN_3) windows are sandwiched with the help of a solid front- and back-plate (Fig. 3.20). The front plate is forged out of PEEK (polyetheretherketone) [147] or Teflon (polytetrafluoroethylene, PTFE) [148] for their excellent chemical resistances. The front-plate contains two small tubes, made from the same material, to conveniently inject the sample solutions. The tubes can be sealed off with glass plugs. The back-plate, although not in direct contact with the sample solution, is forged out of corrosive-resistant stainless steel (V2A, 1.4301) [149]. Five small bolts assure that the silicon-nitrite windows rest in a fixed position while sandwiched. The two Si_3N_4 windows are separated by a Teflon spacer, and the sample thickness can be varied between 10-200 μm. Over the course of this work different batches of windows were used, with 500-1000 nm membrane thickness, to avoid nonlinear artifacts due to window signals.

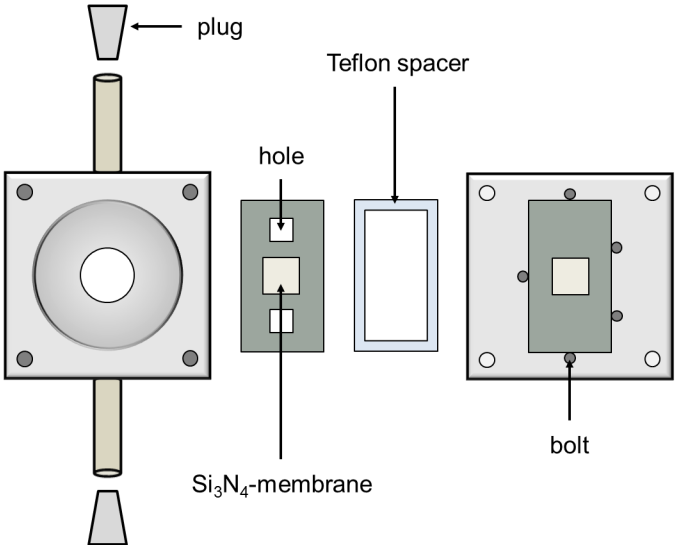

Figure 3.20: Nanofluidic cell used in the time-resolved experiments. Two silicon-nitrite membranes (500-1000 nm thickness) are sandwiched with the help of a solid front- and back-plate. Sample thickness is controlled by Teflon spacers (10-200 μm). The nanofluidic cell is injected with sample solution and sealed off with two glass plugs.

4

H_2O-Monomers in Acetonitrile

We start by investigating the properties of water monomers in acetonitrile to benchmark our measurements on hydrated excess protons in acetonitrile. In such systems, the water content can be controlled precisely and hydrogen bonding to acetonitrile occurs in the form of CN$\cdots$HO, thus bridging the gap between water monomers in non-polar, non-hydrogen bonding solvents and bulk water. These intermediate systems are helpful to describe the properties of water in biological environments with partial hydration, such as surface areas of proteins and membranes.
As outlined in subsection 2.1.2, the femto- to picosecond dynamical processes of bulk water are fairly well understood and one has mapped particular structural rearrangements and vibrational relaxation processes in real time [26, 44].
Acetonitrile represents an environment that preserves, to a certain extent, the time scales of structural fluctuations compared to bulk water. Does the vibrational relaxation scheme of bulk H_2O [52] apply for water monomers in acetonitrile?
The anharmonic coupling between the OH stretching vibrations and the bending vibration of water monomers in non-polar environments has been addressed by picosecond two-color pump-probe studies [150]. In such systems, a similar relaxation pathway as in bulk water was suggested, where the OH stretching population decays via the OH bending overtone and fundamental. However, limited time resolution has made it difficult to directly map transient populations of the OH bending vibration and discern them from the response due to anharmonic coupling to the OH stretching modes.
Moreover, Cringus et al. investigated the effect of hydrogen bonding and intramolecular coupling on the energy relaxation rates of the symmetric and asymmetric OH stretching vibrations of water monomers diluted in acetonitrile [151, 152]. They demonstrated that vibrational excess energy equilibrates on a 200 fs time scale between the OH stretching vibrations in water monomers diluted in ACN. Furthermore, they showed that hydrogen bonding to neighboring water molecules in acetonitrile/water mixtures facilitates vibrational energy relaxation (VER).
We use femtosecond two-color pump-probe spectroscopy to identify vibrational lifetimes of water monomers in acetonitrile, which are substantially faster than for water monomers in a non-polar, non-hydrogen bonding environments. We further investigate the coupling between the OH stretching and bending vibrations and separate it from population kinetics. The graphics in this chapter are based on [153].

4.1 Steady State Absorption Spectrum

The steady state absorption spectrum of 1.28 M H_2O diluted in ACN-d_3 (Fig. 4.1) is less complex and convoluted compared to bulk water (cf. Fig. 2.2 on page 17). The ratio of

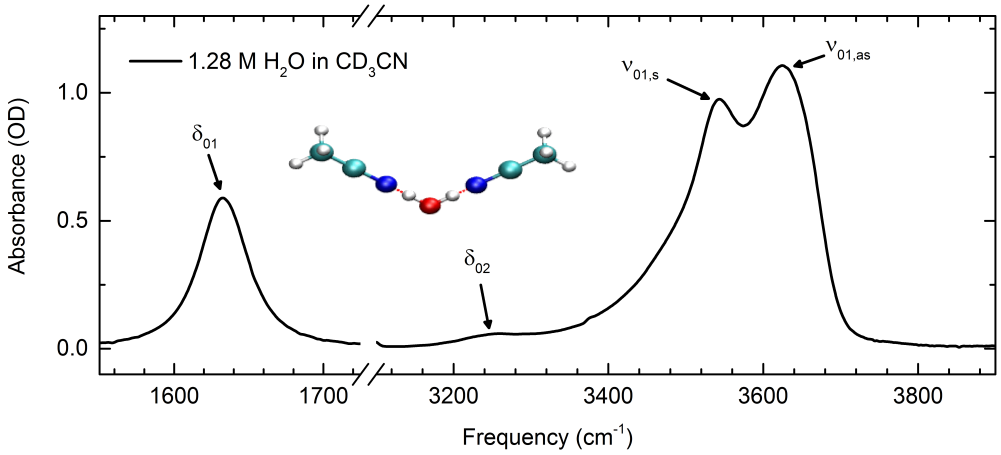

Figure 4.1: Steady state absorption spectrum of 1.28 M H_2O diluted in deuterated acetonitrile (ACN-d_3/CD_3CN) after subtraction of the solvent. Four distinct absorption features can be assigned in a range from 1000-4000 cm^{-1} – the OH bending vibration (δ_{01}) at ~1630 cm^{-1}, its overtone transition (δ_{02}) at ~3250 cm^{-1} and the symmetric ($\nu_{s,01}$) and asymmetric ($\nu_{as,01}$) OH stretching vibrations at ~3545 cm^{-1} and ~3625 cm^{-1}, respectively.

H_2O to CD_3CN molecules is 1:15 and the water molecules are present in the monomeric form bound to two acetonitrile molecules (cf. sketch in Fig. 4.1) [151]. One identifies four distinct absorption features in a range from 1000-4000 cm^{-1}. The fundamental OH bending vibration (δ_{01}) at 1630 cm^{-1} with a FWHM of approximately 40 cm^{-1}, its overtone (δ_{02}) at ~3250 cm^{-1} and the symmetric ($\nu_{s,01}$) and asymmetric ($\nu_{as,01}$) OH stretching vibrations at 3545 cm^{-1} and 3625 cm^{-1}, respectively. In comparison to bulk water, the symmetric and asymmetric OH stretching vibrations of H_2O-monomers in ACN-d_3 are identified and have distinct maxima in the steady state absorption spectrum.

4.2 OH Stretching Vibrations

Transient infrared absorption spectra in the range of the symmetric (ν_s) and asymmetric (ν_{as}) OH stretching vibrations of 1.28 M H_2O in ACN-d_3 for excitation centered at 3600 cm^{-1} are shown in Fig. 4.2a. The absorbance change $\Delta A = -\log_{10}(T/T_0)$ is plotted as a function of probe frequency (T, T_0: transmission of the sample with and without excitation) for fixed pump-probe delays in a range from 0.1-50 ps. One observes a broad negative absorption feature for the frequency interval ~3580-3740 cm^{-1} due to the ground state bleach on the v = 0 to 1 transition and stimulated emission on the v = 1 to 0 transition of the asymmetric OH stretching oscillator. As a consequence of the relatively broad excitation pulse (FWHM = 235 cm^{-1}), both the symmetric and asymmetric OH stretching oscillators are vibrationally excited and contribute to the observed absorbance changes below ~3580 cm^{-1}. The positive excited state absorption signal (v = 1 to 2) of the asymmetric stretching vibration overlaps with the negative GSB & SE signal of the symmetric stretching vibration, resulting in a small positive signal at early delay times (<1 ps) for frequencies in the range ~3550-3580 cm^{-1} and a negative signal for delay times longer than 1 ps. Due to the partial compensation of these components, the observed absorbance change for frequencies below ~3580 cm^{-1} is small compared to the signal caused by the

fundamental transition of ν_{as}. The ESA of the symmetric OH stretching oscillator is not observed in the measured frequency range.
Transient absorption changes for fixed probe frequencies are plotted as a function of pump-probe delay in Fig 4.2b. The kinetic transient taken at 3570 cm^{-1} shows the complex convoluted dynamics of the overlapping signals of the ESA of ν_{as} with the GSB & SE of ν_s. Deciphering such kinetic transients proves difficult, thus we derive characteristic time constants from the bleaching signal of ν_{as} (blue symbols) above 3580 cm^{-1} , as it does not overlap with other transient signals. The data decays biexponetially, revealing a fast initial decay with a 0.6 ± 0.1 ps time constant and a slower 6.4 ± 1 ps decay. According to Cringus et al. [152], this fast component is due to energy transfer between the two OH stretching oscillators and rotational relaxation. The 6.4 ± 1 ps is attributed to the vibrational lifetime of the v = 1 state of the OH stretching modes of water monomers diluted in ACN-d_3. We assume the same v = 1 lifetime for both ν_s and ν_{as}, since equilibration between them is

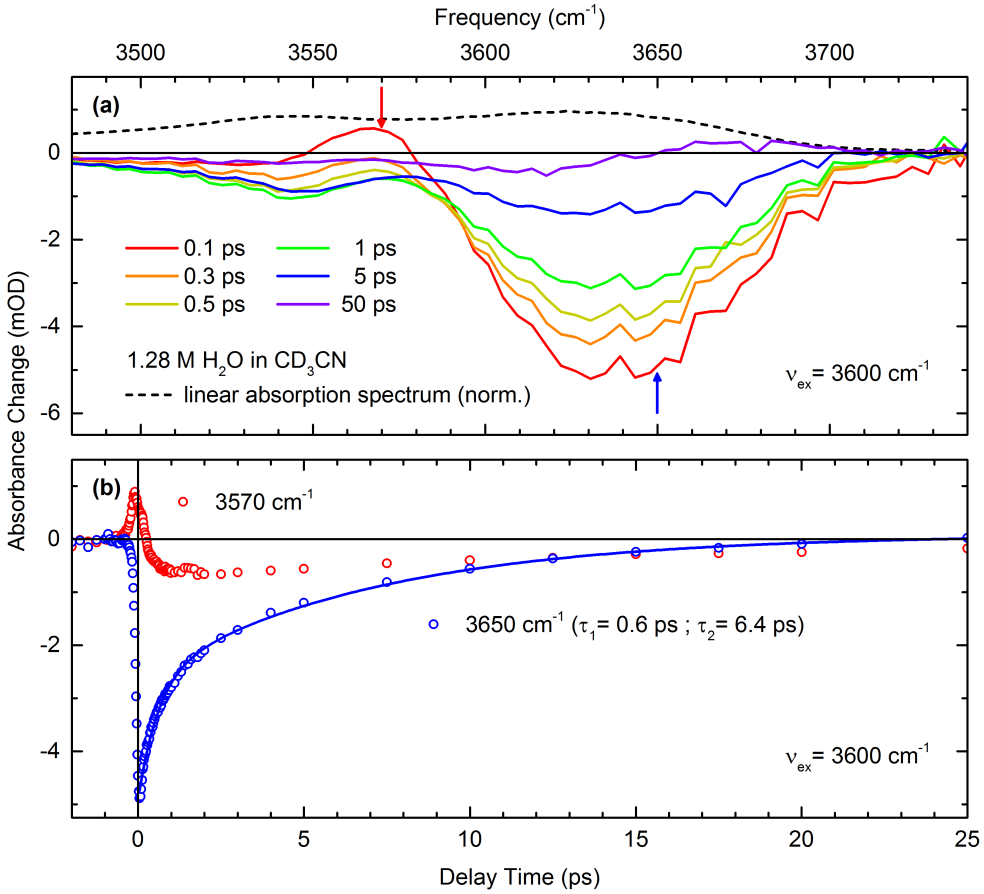

Figure 4.2: **(a)** Transient infrared absorption spectra (colored lines) of the OH stretching vibrations of water monomers in ACN-d_3 for fixed pump-probe delays in a range from 0.1-50 ps. The steady state absorption spectrum (normalized) of 1.28 M H_2O in ACN-d_3 is shown by the dashed black line. The pump pulse was centered around 3600 cm^{-1}. **(b)** Time-resolved absorbance changes $\Delta A = -\log_{10}(T/T_0)$ (symbols) at probe frequencies of 3570 cm^{-1} and 3650 cm^{-1} are plotted as a function of pump-probe delay (T, T_0: transmission of the sample with and without excitation).

much faster than their population decay [152].

4.3 OH Bending Vibration

4.3.1 H_2O in CD_3CN

We performed polarization resolved pump-probe experiments with a time resolution of ∼105 fs on the OH bending vibration (δ_{01}) of water monomers in deuterated acetonitrile. Transient infrared absorption spectra after resonant OH bending excitation (ν_{ex} = 1630 cm^{-1}) are shown in Fig. 4.3a. The absorbance change ΔA is plotted as a function of probe frequency for fixed pump-probe delays in a range from 0.1-50 ps.
The negative absorption feature for the frequency interval ∼1620-1670 cm^{-1} is caused by the ground state bleach and stimulated emission between the v = 0 to 1 transition of the bending oscillator. The positive absorption feature for frequencies smaller than 1620 cm^{-1} originates from the excited state absorption between the v = 1 to 2 transition of the bending oscillator.
Kinetic transients taken at frequency positions indicated by the colored arrows are summarized in Fig. 4.3b. The absorbance change ΔA is plotted as a function of pump-probe delay. Kinetic transients taken at 1590 cm^{-1} and 1635 cm^{-1} represent the vibrational dynamics of the ESA and GB & SE, respectively. The data acquired for parallel (blue) and perpendicular (red) polarization between pump and probe pulses reveal a fast (0.4 ± 0.1 ps) and a slow (4 ± 0.5 ps) component. The latter is the vibrational lifetime of the v = 1 state and describes the population relaxation of the excited bending oscillator into the ground state (v = 1 to 0).
The fast component has no intuitive interpretation, so we calculated the isotropic decay $\Delta A_{iso}(\tau)$ (Eqn. 3.52 on page 40) (black), which only contains population relaxation dynamics. We derived a mono-exponential decay with a 4 ps time constant, thus the fast component can be attributed to a decay of pump-probe anisotropy.
Fig. 4.3c shows the calculated anisotropy $r(\tau)$ (Eqn. 3.51 on page 40) for probe frequencies of 1590 cm^{-1} (black) and 1635 cm^{-1} (red) with monoexponential decays of 0.5 ± 0.1 ps and 0.4 ± 0.1 ps, respectively. Cringus et al. [152] have found a biexponential decay of the pump-probe anisotropy for their pump-probe measurements on the OH stretching oscillators of water monomers in acetonitrile. They attributed the fast 0.2 ± 0.1 ps component to intramolecular energy transfer and the slower 2.2 ± 0.5 ps component to the reorientation of the water molecules within the ACN environment. Just recently, Carpenter et al. [154] found the same time scales for their polarization resolved 2D-IR measurements on the OH bending vibration of water monomers in acetonitrile and assigned them to the same processes as Cringus et al. Cringus et al. [152].
In consideration, that similar times cales were found for the OH stretching and bending region of water monomers in acetonitrile, it is probable that the fast 0.4 ± 0.1 ps component found in our measurements on the OH bending vibration of water monomers in ACN-d_3 is due to intramolecular energy transfer. The slower initial decay of pump-probe anisotropy for water monomers in ACN-d_3 compared to ACN (0.4 ± 0.1 ps vs. 0.2 ± 0.1 ps), goes in line with the observation that vibrational relaxation of the OH bending oscillator is twice as fast for H_2O-monomers in ACN compared to ACN-d_3 (cf. Table 4.1). It should be noted that we did not observe a slower time scale in the decay of pump-probe anisotropy, that would describe the reorientation of the water molecules in ACN-d_3.

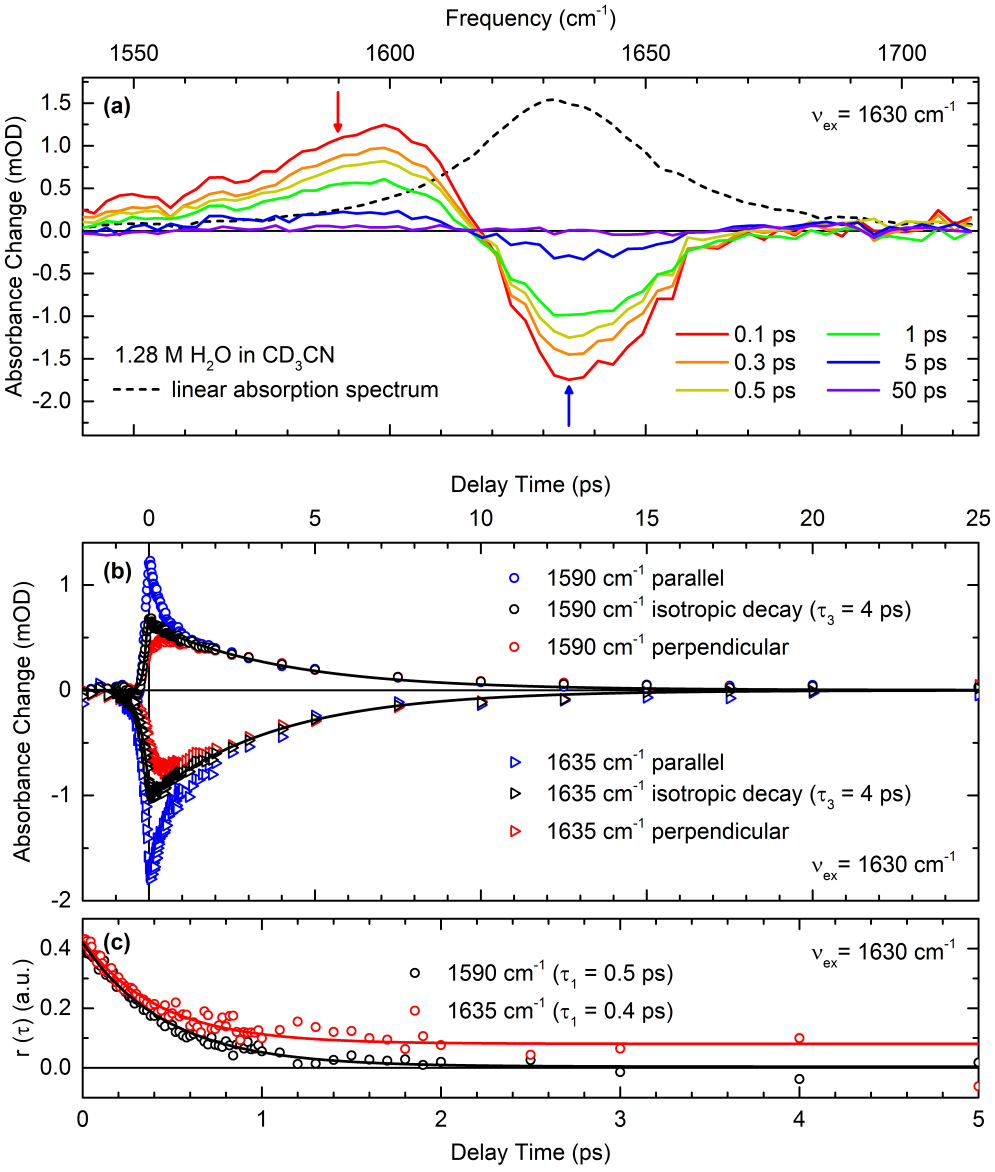

Figure 4.3: **(a)** Transient infrared absorption spectra (colored lines) of the OH bending vibration of water monomers in ACN-d_3 for fixed pump-probe delays in a range from 0.1-50 ps. The steady state absorption spectrum (scaled) of 1.28 M H_2O in ACN-d_3 is shown by the dashed black line. The pump pulse was centered around 1630 cm^{-1}. **(b)** Time-resolved absorbance changes ΔA (symbols) at fixed probe frequencies are plotted as a function of pump-probe delay. The absorbance changes at probe frequencies of 1590 cm^{-1} and 1635 cm^{-1} were measured for parallel (blue symbols) and perpendicular (red symbols) polarization between pump and probe pulses. The calculated isotropic signal (black symbols) decays for both frequencies with a 4 ps time constant (black lines). **(c)** Calculated anisotropy at probe frequencies of 1590 cm^{-1} and 1635 cm^{-1} as a function of pump-probe delay.

4.3.2 H_2O in CH_3CN

In order to investigate the effect of solvent deuteration on the vibrational relaxation of water monomers in ACN-d_3 in more detail, we have also performed pump-probe experiments on H_2O in CH_3CN.
Transient infrared absorption spectra after resonant OH bending excitation are shown in Fig. 4.4a. The absorbance change ΔA is plotted as a function of probe frequency for fixed pump-probe delays in a range from 0.3-50 ps. The transient absorption spectra look very similar to those obtained for H_2O-monomers in deuterated acetonitrile. We observe the negative absorption feature caused by the ground state bleach and stimulated emission between the v = 0 and 1 state of the OH bending oscillator, as well as the positive absorption feature due to the ESA between the v = 1 to 2 transition at nearly identical frequency positions.
Kinetic transients taken at fixed frequency positions are shown in Fig. 4.4b. The absorbance

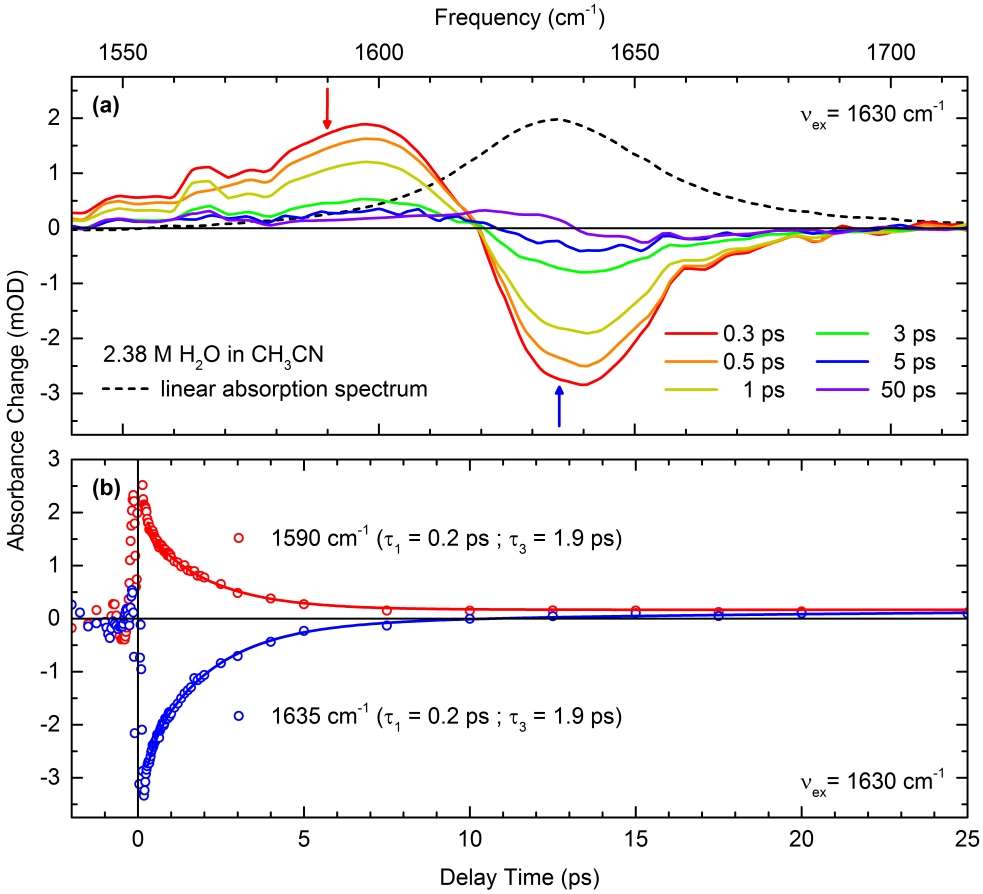

Figure 4.4: **(a)** Transient infrared absorption spectra (colored lines) of the OH bending vibration of water monomers in ACN for fixed pump-probe delays in a range from 0.3-50 ps. The steady state absorption spectrum (scaled) of 2.38 M H_2O in ACN is shown by the dashed black line. The pump pulse was centered around 1630 cm^{-1}. **(b)** Time-resolved absorbance changes ΔA (symbols) at probe frequencies of 1590 cm^{-1} and 1635 cm^{-1} are plotted as a function of pump-probe delay.

change ΔA is plotted as a function of pump-probe delay. Both the transient at 1590 cm^{-1} and 1635 cm^{-1} exhibit a biexponential decay with a 0.2 ± 0.1 ps and a 1.9 ± 0.5 ps time constant. In accordance with our measurements on water monomers in deuterated acetonitrile, the fast component is due to the decay of pump-probe anisotropy and has a similar value as the anisotropy decay for the OH stretching vibrations of H_2O-monomers in CH_3CN found by Cringus et al. [152] and the anisotropy found for the OH bending vibration by Carpenter et al. [154]. The slower component is attributed to the vibrational lifetime of the v = 1 state of the OH bending oscillator, decaying twice as fast compared to water monomers in deuterated acetonitrile (see paragraph: "OH bending relaxation" on page 65).

4.4 Anharmonic Couplings and Vibrational Energy Relaxation

4.4.1 OH Stretch to Bend coupling

Now that we have characterized the vibrational dynamics of the OH stretching and bending vibrations of water monomers in ACN-d_3 after resonant excitation, we want to investigate their anharmonic coupling. To do so, we performed two-color pump-probe measurements with resonant excitation of the OH stretching oscillators, while probing the vibrational response in the range of the bending fundamental (δ_{01}).

Transient infrared absorption spectra are shown in Fig 4.5a. The measured absorption changes look similar to those observed with excitation centered around 1630 cm^{-1}. The enhanced absorption for frequencies below 1635 cm^{-1} however, shows clear spectral reshaping with increasing delay time between pump and probe pulses. The initial maximum is centered around ∼1610 cm^{-1} and shifts to lower frequencies over time until it is at similar values compared to the measured transients with resonant OH bending excitation.

Kinetic transients, taken at the frequency positions indicated by the colored arrows in Fig. 4.5a are plotted in Fig. 4.5b as a function of pump-probe delay. It is immediately evident, that the vibrational dynamics are markedly different from the experiment with resonant OH bending excitation.

The kinetic transients were analyzed by a rate-equation model based on the level scheme shown in Fig. 4.7 including the time constants derived from the one-color pump-probe experiments (cf. Table 4.1).

The bleaching signal (blue symbols) shows an instantaneous rise of signal strength within the time resolution of the experiment and a subsequent slower rise in signal strength. The instantaneous rise is the direct manifestation of the anharmonic coupling between OH stretching and bending modes of water monomers in deuterated acetonitrile. This signal decays with the vibrational lifetime of the OH stretching modes. The second component rises with a 6.4 ps time constant and decays with the vibrational lifetime of the v = 1 state of the OH bending oscillator. This behavior accounts for population transfer from the OH stretching modes to the OH bending mode and shows excellent agreement with the experimental data. It should be noted that a perturbed free induction decay [118] is observed for negative time delays.

The kinetic transients taken at 1610 cm^{-1} and 1590 cm^{-1} display a similar behavior. For both frequencies one has to include an initial 0.6 ps time constant in order to simulate the data, which corresponds to the fast component observed in the one-color pump-probe experiments. Furthermore, it is evident, that the signal for population transfer is less pronounced for the kinetic transient taken at 1590 cm^{-1} compared to the one taken at 1610 cm^{-1} and 1635 cm^{-1}. This characteristic is correlated to the spectral reshaping observed in the tran-

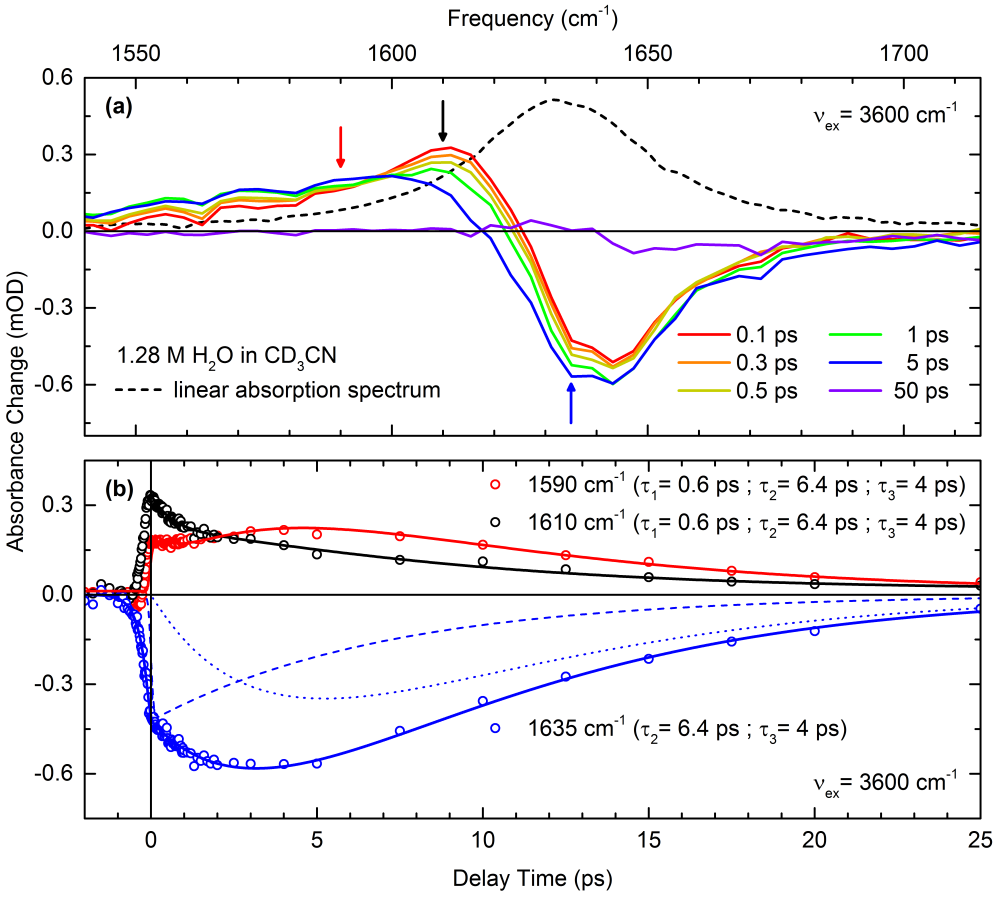

Figure 4.5: **(a)** Transient infrared absorption spectra (colored lines) of the OH bending vibration of water monomers in ACN-d_3 for fixed pump-probe delays in a range from 0.1-50 ps. The steady state absorption spectrum (scaled) of 1.28 M H_2O in ACN-d_3 is shown by the dashed black line. The pump pulse was centered around 3600 cm^{-1}. **(b)** Time-resolved absorbance changes ΔA (symbols) at probe frequencies of 1590 cm^{-1}, 1610 cm^{-1} and 1635 cm^{-1} are plotted as a function of pump-probe delay. The dashed and dotted blue line represent the decomposition of the numerical fit for the probe frequency of 1635 cm^{-1} (blue line) into its two major components.

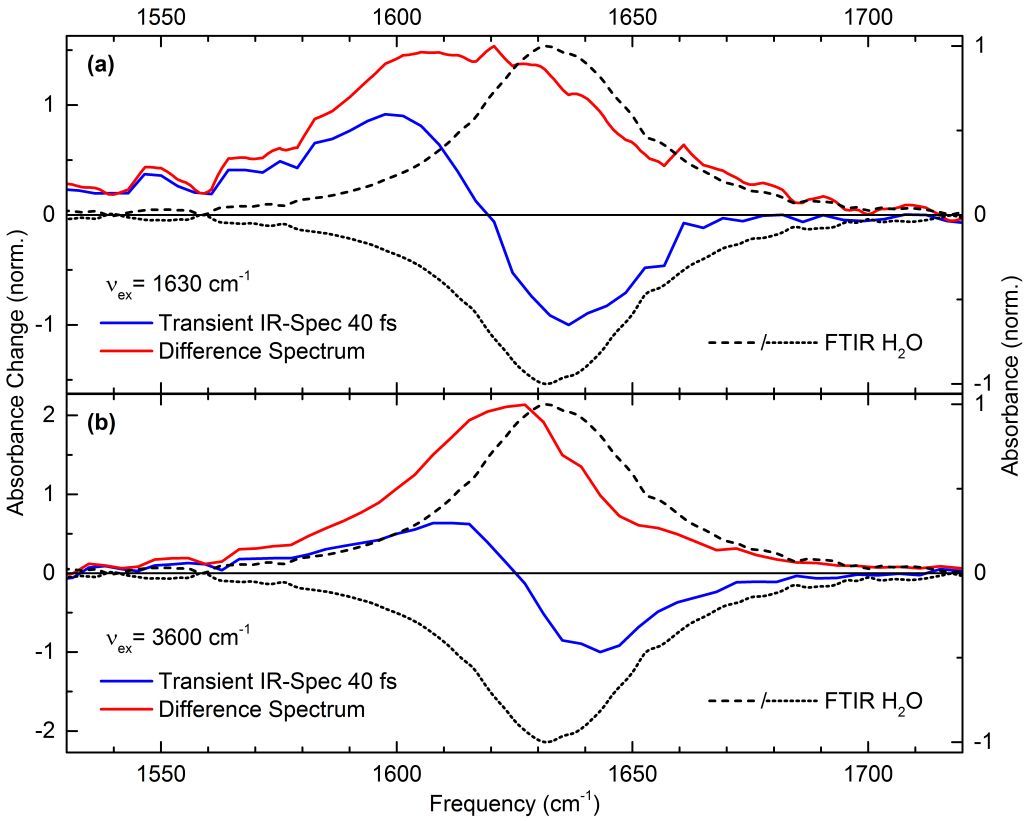

Figure 4.6: **(a)** Normalized transient infrared absorption spectrum of the OH bending vibration of water monomers in ACN-d_3 at 40 fs pump-probe delay (blue line). The absorption signal of the v = 1 to 2 transition is shown in red after subtraction of the scaled and inverted steady state absorption spectrum of H_2O-monomers to approximate the contribution of the v =0 to 1 transition. The maximum of the excited state absorption signal is at 1605 ±5 cm^{-1}. The pump pulse was centered around 1630 cm^{-1}. **(b)** Same as (a) but for excitation at ν_{ex} = 3600 cm^{-1}. The maximum of the excited state absorption signal is at 1620 ±5 cm^{-1}.

sient infrared absorption spectra shown in Fig. 4.5a and can be linked to different values for the diagonal and non-diagonal anharmonicity.

We analyze the positive absorption signal in the transient spectra of the OH bending vibration at early delay times obtained for both resonant (ν_{ex} = 1630 cm^{-1}) and off-resonant (ν_{ex} = 3600 cm^{-1}) excitation, in order to quantify the diagonal and non-diagonal anharmonic shift. In the case of resonant OH bending excitation, the ESA appears at lower frequencies due to the anharmonicity of the vibrational potential. To determine the diagonal anharmonicity, we subtracted the contributions of the v_δ = 0 to 1 transition from the transient spectrum taken at 40 fs, in order to retrieve the "pure" lineshape of the v_δ = 1 to 2 transition (Fig. 4.6a). This is done by subtracting the scaled and inverted linear absorption spectrum (dotted black line), that approximates the v_δ = 0 to 1 transition. The retrieved "pure" lineshape of the ESA (red line) shows a maximum at ∼ 1605 ± 5 cm^{-1} compared to 1630 ± 5 cm^{-1} of the fundamental transition (dashed black line) and thus we retrieve a diagonal anharmonic shift of 25 ± 5 cm^{-1} for the bending oscillator.

In the same way, we have analyzed the shift of the enhanced absorption signal compared to

Table 4.1: Time constants derived from a rate-equation analysis of the measured pump-probe transients (ν_{ex}: pump frequency, ν_{pr}: probe frequency). The upper part relates to data measured with resonant excitation of the OH stretching modes, the lower part to resonant OH bending excitation. The components with decay times τ_1 account for the fast rotation/redistribution signal after OH stretching excitation and the anisotropy decay after OH bending excitation. The time constants τ_2 and τ_3 represent population decay times.

	CD_3CN			CH_3CN		
	τ_1 (ps)	τ_2 (ps)	τ_3 (ps)	τ_1 (ps)	τ_2 (ps)	τ_3 (ps)
$\nu_{ex} = 3600$ cm^{-1}						
$\nu_{pr} = 3600$ cm^{-1}	0.6 ± 0.1	6.4 ± 1	-	-	-	-
$\nu_{pr} = 1635$ cm^{-1}	-	6.4 ± 1	4.0 ± 0.5	-	-	-
$\nu_{pr} = 1610$ cm^{-1}	0.6 ± 0.1	6.4 ± 1	4.0 ± 0.5	-	-	-
$\nu_{ex} = 1630$ cm^{-1}						
$\nu_{pr} = 1635$ cm^{-1}	0.4 ± 0.1	-	4.0 ± 0.5	0.2 ± 0.1	-	1.9 ± 0.5
$\nu_{pr} = 1590$ cm^{-1}	0.4 ± 0.1	-	4.0 ± 0.5	0.2 ± 0.1	-	1.9 ± 0.5

the fundamental transition of the OH bending oscillator after excitation of the OH stretching vibrations (Fig. 4.6b). The enhanced absorption signal after subtraction (red line) of the inverted and scaled steady state absorption spectrum (dotted black line) shows a maximum at ∼1620 ± 5 cm^{-1}, thus we retrieve a non-diagonal anharmonic shift of 15 ± 5 cm^{-1}. It should be noted, that the lineshape of the enhanced absorption feature at early delay times is close to that of the fundamental transition and clearly different from the one observed for resonant OH bending excitation (Fig. 4.6a).

4.4.2 Vibrational Relaxation Pathway

A scheme of the vibrational relaxation pathway of water monomers in acetonitrile after OH stretching excitation derived from experimental results is shown in Fig. 4.7. It includes the $v_{\nu,s/as} = 0$ and $v_{\nu,s/as} = 1$ state of the symmetric and asymmetric OH stretching vibrations, the $v_\delta = 0$, $v_\delta = 1$ and $v_\delta = 2$ state of the OH bending vibration as well as the three states (v_L = 0-3) of the librational mode highest in frequency for the water monomer in ACN-d_3.

OH stretching relaxation

Simultaneous excitation of the symmetric and asymmetric OH stretching vibrations is shown by the blue upward oriented arrow between the $v_\nu = 0$ and $v_{\nu,s/as} = 1$ states (Fig. 4.7). Equilibration between the the OH stretching vibrations occurs on a much shorter time scale than their population relaxation [152] and is not included in the relaxation scheme. The OH stretch oscillators transfer their population with a 6.4 ± 1 ps time constant to the OH bending overtone ($v_\delta = 2$). This process involves an effective mechanism that bridges the energy mismatch between the excited OH stretching vibrations and the OH bending overtone of roughly 350 cm^{-1}.
For bulk water, the v = 1 states of the OH stretching vibrations appear at lower frequencies (∼3400 cm^{-1}) due to the stronger hydrogen bonding between different water molecules

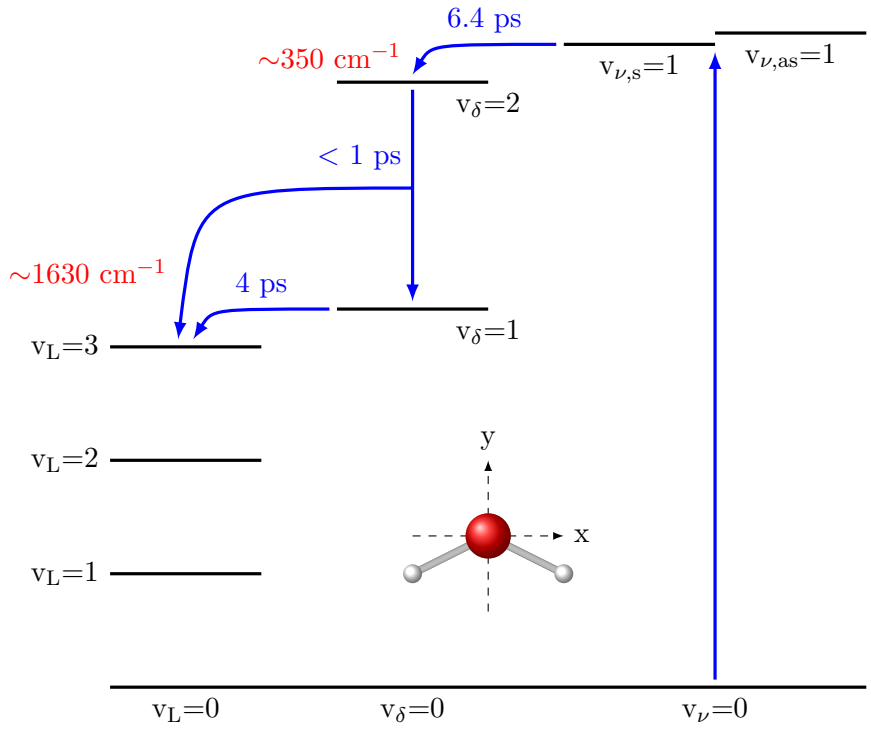

Figure 4.7: Vibrational relaxation scheme of water monomers in acetonitrile. Following vibrational excitation of the symmetric ($v_{\nu,s} = 1$) and asymmetric ($v_{\nu,as} = 1$) OH stretching vibrations the vibrational energy is transferred to the OH bending overtone ($v_\delta = 2$) with a 6.4 ps time constant. The population of the OH bending overtone ($v_\delta = 2$) relaxes in less then 1 ps to the first excited state of the OH bending vibration ($v_\delta = 1$). Subsequently the $v_\delta = 1$ state of the OH bending vibration relaxes with a 4 ps time constant into the ground state ($v_\delta = 0$). The excess energy is in both steps transferred to librational motions of the water monomer in ACN-d_3 ($v_L = 3$).

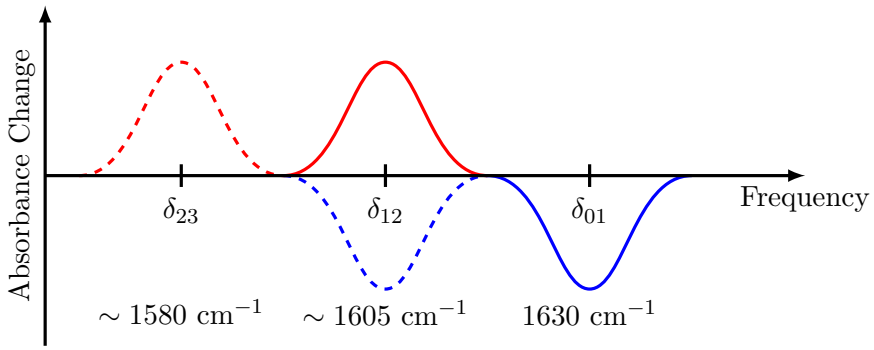

Figure 4.8: Schematic representation of the absorption features between the v = 0 to 1, v = 1 to 2 and v = 2 to 3 transition of the OH bending oscillator. The ground state bleach and stimulated emission of the respective transition are shown in blue and the excited state absorption is shown in red.

compared to the hydrogen bonding between H_2O and ACN-d_3. This reduces the energy mismatch between $v_{\nu,s} = 1$ and $v_\delta = 2$. Additionally, structural fluctuations of the hydrogen bond network lead to femtosecond spectral diffusion of the OH stretching excitations, thus exploring the frequency range of the $v_\delta = 2$ transiently [53]. This increases the OH stretch-bend transfer rate dramatically, leading to the observed 200 fs lifetime of the $v = 1$ state of the OH stretching vibrations in bulk water [52]. For water monomers in ACN-d_3 however, the bending overtone is clearly separated form the OH stretching vibrations leading to much smaller transition rates and picosecond lifetimes.
For our analysis we want to embark on an approach outlined by Rey and Hynes for the vibrational energy relaxation of HDO in liquid D_2O [155] and translate their principles to H_2O-monomers in ACN-d_3.
The system Hamiltonian can be described as:

$$H = H_{H_2O} + H_{coupling} + H_{bath} \ , \tag{4.1}$$

where H_{H_2O} is the quantum mechanical anharmonic Hamiltonian of the H_2O molecule including static effects of the solvent, $H_{coupling}$ the Hamiltonian describing the coupling between vibrational modes of the H_2O molecule and the solvent and H_{bath} is the Hamiltonian of the ACN-d_3 solvent including rotations and translations of the H_2O molecule. The coupling Hamiltonian:

$$H_{coupling} = H_{V-B} + H_{cor} + H_{cen} \ , \tag{4.2}$$

consists of the coupling between the vibrational coordinates of H_2O and ACN-d_3 (H_{V-B}), Coriolis coupling between the intramolecular normal modes of H_2O (H_{cor}) and centrifugal coupling between the vibrational and rotational modes (H_{cen}). The transition rate of a transition i to j depends critically on the coupling of the intramolecular anharmonic potential to solvent modes and is described by [43, 155]:

$$W_{ij} = C|H_c|^2 \cdot \int_{-\infty}^{+\infty} \mathrm{d}t \ e^{(-i\omega_{ij}t)} \langle f(0)f(t)\rangle \ . \tag{4.3}$$

This integral represents the Fourier amplitude of the fluctuating force at $\omega_{\nu(01)-\delta(02)} \approx 300$-$380$ cm^{-1} acting on the OH bending oscillator. C is a constant, $H_c = \langle f|q_\delta|i\rangle$ the matrix element with the bending normal coordinate q_δ and the initial and final states i and f, respectively. $|i\rangle$ and $|f\rangle$ are coupled by the vibrational coupling factors arising from H_{V-B} in accordance to the anharmonicity of the intramolecular vibrational potential. This allows transitions such as $v_\nu = 1$ to $v_\delta = 2$ that would be forbidden in the harmonic approximation and gives rise to the Fourier factor $exp(-i\omega_{ij}t)$. $\langle f(0)f(t)\rangle$ is the time correlation function of the fluctuating force.
A suitable mode to accept the excess energy upon $v_\nu = 1$ to $v_\delta = 2$ relaxation is the C$-$C$\equiv$N bending motion of acetonitrile, which shows pronounced spectral density at 380 cm^{-1} [156]. This mode is expected to be stochastically populated under ambient conditions (T = 300 K) and is a major contributor to the fluctuating force on the intramolecular bending vibrations of water monomers in ACN, thus facilitating OH stretch to bend relaxation. Further librational motions of the excited H_2O molecule can add to this fluctuating force, especially the hindered rotation around the y-axis as we see from a simple approximation.
We neglect a different effect of the hydrogen bonding to ACN for hindered rotations around the x and y-axis of the H_2O-monomer (cf. inset in Fig. 4.7). We further assume that the moments of inertia for hindered rotations around the x and y-axis of H_2O, with a ratio of

$\sim$1.74 : 1, directly correlate with the frequency of such motions. Consequently, we deduce a frequency of approximately 290 cm^{-1} for the libration around the y-axis (with 500 cm^{-1} for the libration around the x-axis from [157]). The value of 290 cm^{-1} lies in close proximity to the energy mismatch for the OH stretch to bend relaxation of $\sim$300-380 cm^{-1} and may play an important role as an energy acceptor.

OH bending relaxation

The OH stretching vibrations relax via the OH bending overtone, leading to transient populations of the $v_\delta = 2$ state of the bending oscillator. Such populations give rise to a positive absorption feature corresponding to the $v_\delta = 2$ to 3 transition, which according to the diagonal anharmonicity of the bending oscillator is expected at $\sim$1580 cm^{-1} (red dashed line in Fig. 4.8). Additionally, one would observe a decreased absorbance change in the $\sim$1605 cm^{-1} range, due to the stimulated emission between the v = 2 and v = 1 state of the bending oscillator (dashed blue line in Fig. 4.8). However, in our two-color pump-probe measurements (Fig. 4.5) we did not observe such features, thus transient populations of the $v_\delta = 2$ state must be negligible small. Further, the kinetic transients shown in Fig. 4.5 can be reproduced with just the vibrational lifetimes of the OH stretching vibrations and the lifetime of the v = 1 state of the bending oscillator.
A possible explanation is a substantially shorter vibrational lifetime of the $v_\delta = 2$ state compared to the vibrational lifetime of the v = 1 state of the OH stretching oscillators, thus leading to very small transient populations of $v_\delta = 2$. The smallest detectable absorbance change in our experiments was 0.1 mOD and thus one expects a depopulation rate of the $v_\delta = 2$ state to be at least 6 times faster than for the stretching oscillators ($1/6.4$) ps^{-1}. This results in an upper limit of $\sim$1 ps for the vibrational lifetime of the v = 2 state of the bending oscillator (blue downwards oriented arrow between $v_\delta = 2$ and $v_\delta = 1$ in Fig. 4.7). In the vibrational relaxation process from the v = 2 to 1 state of the bending oscillator, an energy excess of approximately 1620 cm^{-1} must be accepted by other modes of the molecule or the solvent (blue arrow to $v_L = 3$ from $v_\delta = 2$ in Fig. 4.7). A suitable acceptor might be the v = 3 state of the libration (L) of the excited water molecule around its x-axis (cf. inset in Fig. 4.7) with $v_L = 1$ at 500 cm^{-1} [157]. Here, centrifugal coupling H_{cen} in Eqn. 4.2 is the dominant term and the theoretical treatment is similar to Eqn. 4.3.
The v = 1 state of the bending oscillator relaxes with a 4 $\pm$ 0.5 ps time constant into the ground state $v_\delta = 0$ (blue downwards oriented arrow between $v_\delta = 1$ and $v_\delta = 0$ in Fig. 4.7). The excess energy that gets released in this process is comparable to the one for the $v_\delta = 2$ to 1 transition and thus we assume the same channels to accept the energy, e.g. librations of the excited water molecule and low frequency solvent modes.
We expect a very similar relaxation scheme for the VER of H_2O-monomers in CH_3CN after resonant OH stretching excitation. Our reference measurements on the OH bending vibration (Fig. 4.4) revealed a population decay of the $v_\delta = 1$ state twice as fast in CH_3CN compared to CD_3CN. A possible explanation is the weak spectral density of the CH_3 deformation vibration of ACN in the range of the v = 1 state of the bending vibration (1600-1650 cm^{-1}) [158]. This spectral overlap is absent in CD_3CN as molecular vibrations involving the hydrogen atoms shift to lower frequencies upon deuteration. The CH_3 deformation vibration in ACN represents an additional channel for the vibrational excess energy that gets released in the decay of the OH bending oscillator, thus increasing the depopulation rates and resulting in a shorter v = 1 lifetime of the OH bending oscillator for H_2O-monomers in CH_3CN compared to H_2O-monomers in CD_3CN.

"To raise new questions, new possibilities, to regard old problems from a new angle, requires creative imagination and marks real advance in science."

– Albert Einstein (1879-1955)

5 Zundel Cations in Acetonitrile

Chapter 2 outlined the elusiveness of hydrated protons in liquid water, a system intensely studied [20, 22, 94]. Current pictures of proton transport in water are dominated by theoretical studies while experimental verification has lagged behind.
Investigating excess protons in bulk liquid water at ambient conditions has proven difficult and the relative abundance and stability of Zundel and Eigen complexes has remained ambiguous. The proton motifs are subject to strong structural modulations exerted by the fluctuating character of the environment − bulk water − and arise from librational motions of the water molecules, hydrogen bond stretch motions and rearrangements in the hydrogen bond network. Inter-conversion of different proton species is expected on the picosecond time scale, closely linked to hydrogen bond breaking and reforming events in the second solvation shell [66].
These complicating matters are circumvented by the selective preparation of Zundel cations in an acetonitrile environment. At low molar ratios of acid and water, Zundel cations are the predominant species embedded in an acetonitrile solvent cage.
The polar solvent acetonitrile undergoes structural fluctuations on a multitude of time scales, with strong contributions in the sub-100 fs range [31], thus retaining the fluctuating character of the proton environment in this model system when compared to bulk water.
Besides the outstanding qualities as a benchmark system to characterize a prototypical species in a fluctuating environment, it mimics less polar biological environments with partial hydration better than protons in bulk water. Among such systems are reactive sites of enzymes, proton channels or the surface area of proteins where the hydrated H^+ plays a key role.
In the following, the term "Zundel-cation" is used to describe the solvated $H_5O_2^+$ moiety. It is not meant as a static structure by any means, but rather has a fluctuating character to it. A more thorough definition will be given in chapter 6 of this thesis.

5.1 Steady State Absorption Spectrum

The steady state absorption spectrum of 0.5 M HI (57%) diluted in CH_3CN in a range from 800-4000 cm^{-1} is shown in Fig. 5.2 (red dashed line). HI was chosen as the proton donor, as the iodine counterion does not show any absorption in the investigated spectral range. The prototypical absorption spectrum of a Zundel cation (black line) is derived by subtraction of the acetonitrile background (gray line) and the contributions of water molecules not directly solvating the proton, estimated by the absorption spectrum of water monomers in ACN (blue line; cf. subsection 3.2.4).
Zundel cations predominantly prepared in acetonitrile absorb continuously in a range from 800-3700 cm^{-1} with three distinct maxima at ∼1150 cm^{-1}, ∼1740 cm^{-1} and ∼3400 cm^{-1}.

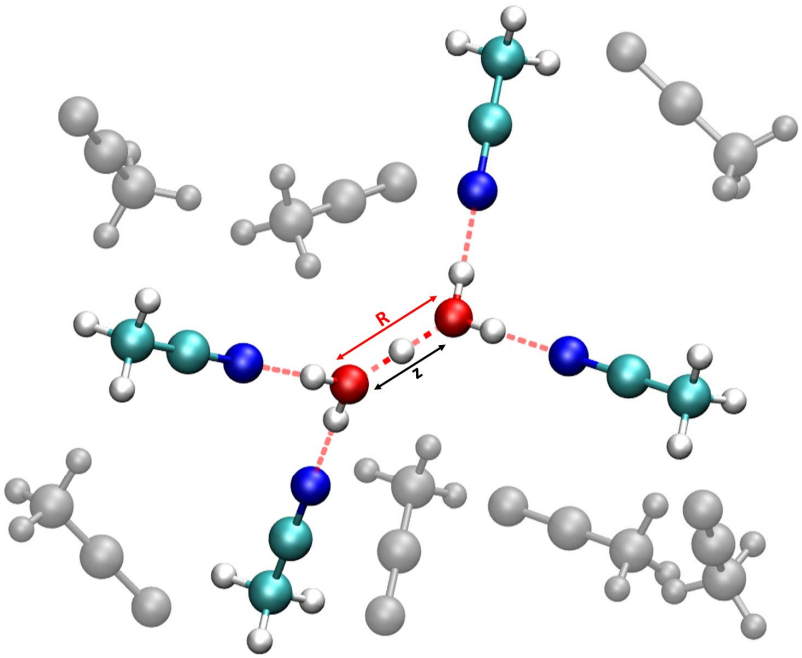

Figure 5.1: Schematic sketch of the Zundel cation in acetonitrile. The proton transfer vibration z and the O$\cdots$O mode R are indicated by the black and red double sided arrow, respectively.

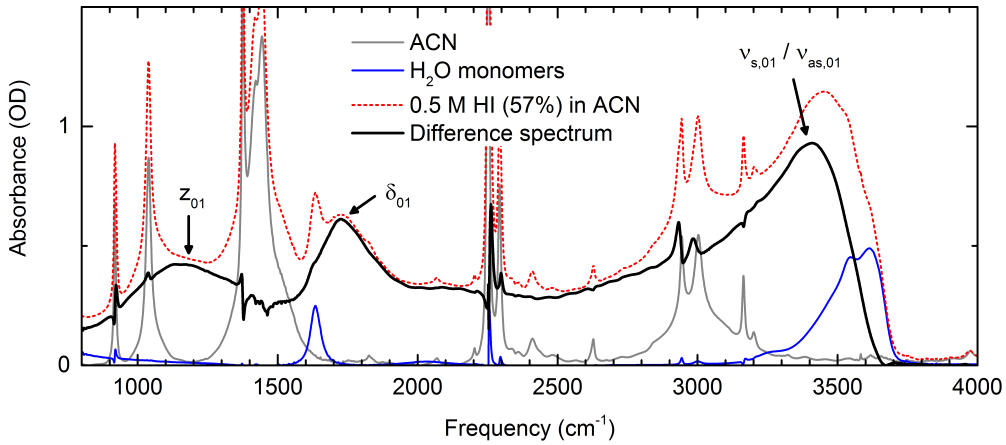

Figure 5.2: Steady state absorption spectrum of 0.5 M HI (57%) diluted in CH_3CN (red dotted line). The absorption spectrum of the Zundel cation ($H_5O_2^+$) is shown in black after subtraction of the acetonitrile solvent (gray line) and the contribution of water monomers in the sample (blue line). Zundel cations show continuous absorption in a range from 800-3700 cm^{-1} with absorption maxima at $\sim$1150 cm^{-1}, $\sim$1740 cm^{-1} and $\sim$3400 cm^{-1}. These features are assigned to the H^+ transfer mode (z), the OH bending (δ) and the symmetric and asymmetric OH stretching modes ($\nu_{s,as}$) of the flanking water molecules.

The absorption feature at ∼1150 cm^{-1}, with a spectral width of ∼500 cm^{-1}, is assigned to the fundamental transition (v = 0 to 1) of the proton transfer mode (z) between the flanking oxygen atoms (cf. Fig. 5.1) [159]. This assignment is in qualitative agreement with state of the art, full dimensional quantum-dynamical simulations of the gas phase protonated water dimer [145] and is regarded as a marker mode for the Zundel cation. The band at ∼1740 cm^{-1} is assigned to the (ungerade) OH bending vibration (δ_{01}) of the flanking water molecules and is substantially broader and blue shifted compared to water monomers in acetonitrile (cf. blue line Fig. 5.2). Symmetric and asymmetric OH stretching vibrations ($\nu_{s,01}/\nu_{as,01}$) on the other hand are red shifted compared to water monomers in ACN and appear as one broad absorption band at ∼3400 cm^{-1}.

5.2 Time-Resolved Experiments and Theoretical Simulations

5.2.1 The Proton Transfer Mode

Investigating the proton transfer vibration (z) by means of ultrafast nonlinear vibrational spectroscopy allows to observe the proton dynamics in Zundel cations directly. We employ two-dimensional mid-infrared and ultrafast pump-probe spectroscopy to map vibrational dynamics and characterize the contributing mechanisms to the observed transient lineshapes.

2D-IR experiments

Absorptive 2D-IR spectra recorded in the range of the fundamental proton transfer vibration are shown in Fig. 5.3. The 2D-IR signal is plotted as a function of excitation (ω_1) and detection frequency (ω_3) for different waiting times T (0, 25, 50, 100 fs). The excitation pulse was centered around 1180 cm^{-1} and has a FWHM of ∼240 cm^{-1}. It should be noted that the pulse width is not sufficient to capture the full spectral width of the absorption band of the z-mode (cf. Fig 5.3a). Red to yellow and blue contour lines in Fig. 5.3 correspond to negative and positive absorption changes, respectively[1]. The intensity difference between neighboring contour lines is 10 %.
The negative absorption feature in the detection frequency interval from ∼1050-1150 cm^{-1} is caused by the ground state bleach of the v = 0 state and the stimulated emission from the v = 1 state of the proton transfer mode. We observe an enhanced absorption feature at higher detection frequencies (1150-1330 cm^{-1}) due to the excited state absorption on the v = 1 to 2 transition of z. Both absorption features span the entire observable excitation frequency range and the contour lines are essentially parallel to the ω_1-axis even for the earliest waiting time $T = 0$. This behavior indicates ultrafast spectral diffusion, where correlations between excitation and detection frequencies are lost very rapidly, resulting in homogeneous lineshapes.
In order to verify this observation, cuts through the maxima of the bleaching (solid lines) and the enhanced absorption (dashed lines) along the diagonal and anti-diagonal direction of our 2D-IR spectra are presented in Fig. 5.4. Cuts taken along the diagonal (black) contain both contributions from homogeneous and inhomogeneous broadening while cuts taken along the anti-diagonal (red) are dominated by homogeneous contributions.

[1] Note that for the sake of comparison pump-probe convention is used for the sign of the transient signals throughout this thesis; cf. subsection 3.1.5 on page 34.

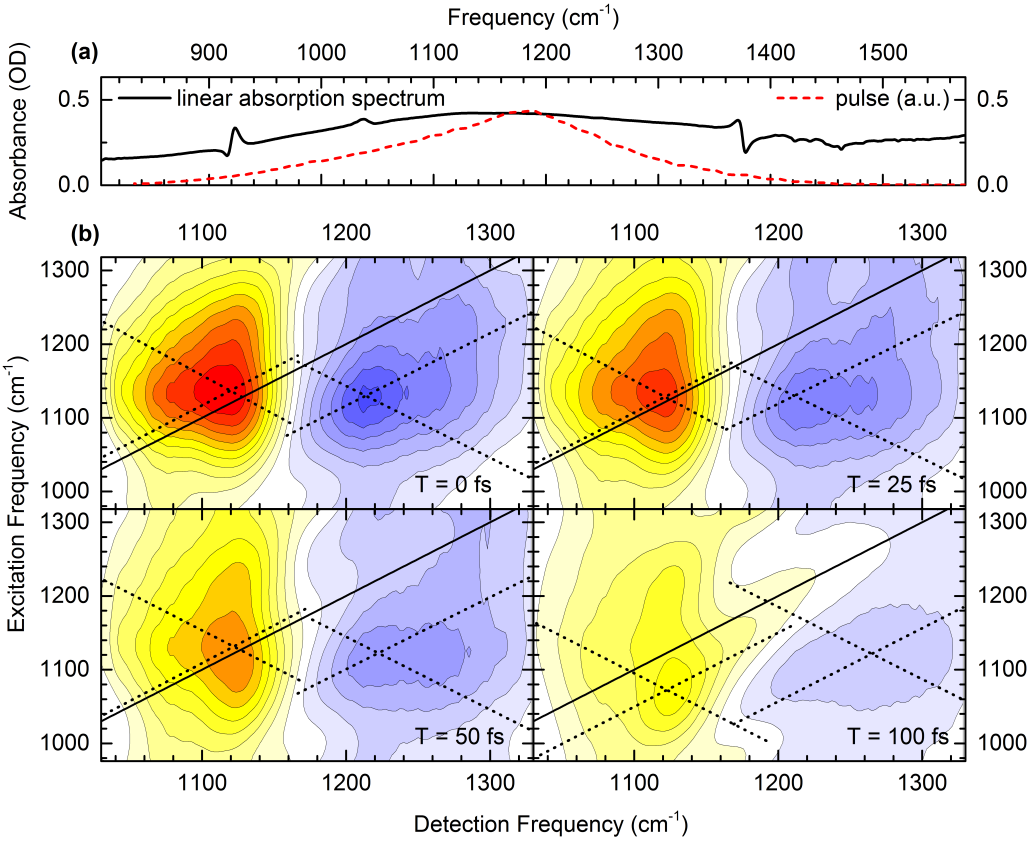

Figure 5.3: **(a)** Excerpt of the linear absorption spectrum shown in Fig. 5.2 in the range of the proton transfer mode z (black line). The mid-IR pulse used in the 2D-IR experiments is indicated with the red dotted line. **(b)** Absorptive 2D-IR spectra in the range of the proton transfer mode (z) with excitation centered around 1180 cm^{-1}. The 2D-IR signal is plotted as a function of excitation frequency (ω_1) and probe frequency (ω_3) for different waiting times T (0, 25, 50, 100 fs). Red to yellow and blue contour lines represent negative and positive absorbance changes, respectively. The intensity change between neighboring contour lines is 10 %.

For the bleaching feature, both cuts are identical for all waiting times T in the accuracy of our experiments. Cuts through the maximum of the enhanced absorption feature display a different behavior. For detection frequencies above ~1250 cm^{-1}, the cuts taken along the diagonal show an increased 2D-signal amplitude compared to the cuts along the anti-diagonal. This difference disappears with increasing waiting time (cf. $T = 0$ fs vs. $T = 100$ fs) and indicates an inhomogeneous contribution on the high frequency wing of the ESA that disappears over time due to spectral diffusion. The origin of this inhomogeneity is not clear yet and needs further investigation.
The measured 2D signals show a fast decay with increasing waiting time T and display basically no signs of spectral reshaping. In order to investigate the population relaxation of the proton transfer mode in more detail, we performed complementary pump-probe measurements covering a much wider frequency range (cf. Fig. 5.5).

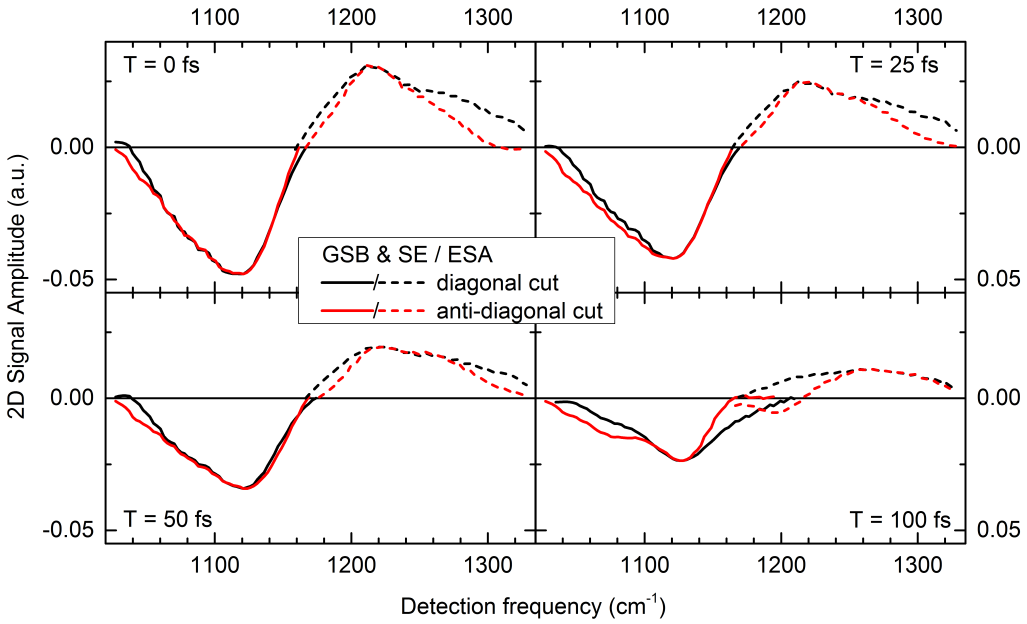

Figure 5.4: Diagonal (black) and anti-diagonal cuts (red) taken along the maximum signal of the GSB & SE (solid lines) and the ESA (dashed lines) in Fig. 5.3b, respectively. The spectral cuts presented in this figure correspond to the dotted black lines in the respective (T = 0, 25, 50, 100 fs) absorptive 2D-IR spectra in Fig 5.3b.

Pump-probe experiments

We applied two-color pump-probe spectroscopy in the range of the v = 1 to 2 transition of z to determine the vibrational lifetime of the v = 1 state. Transient infrared absorption spectra for fixed pump-probe delays in a range from 25 fs to 10 ps are shown in Fig. 5.5a. The absorbance change $\Delta A = -log_{10}(T/T_0)$ is plotted as a function of probe frequency. Excitation pulses were centered at 1200 cm^{-1} with a FWHM of 130 cm^{-1}.
A negative absorption feature is recorded for probe frequencies smaller than 1150 cm^{-1}, and in agreement with our 2D-IR measurements presented in Fig. 5.3, is caused by the ground state bleach and stimulated emission between the v = 0 to 1 transition of the proton transfer mode z. The blue shifted positive absorption changes due to the excited state absorption between the v = 1 and 2 state cover a range from 1150 cm^{-1} to approximately 1500 cm^{-1}.

Fig. 5.5b displays the kinetic transient taken at the maximum position of the ESA indicated by the black arrow in Fig. 5.5a. In order to retrieve characteristic time constants, the experimental data (open circles) was numerically fit to a rate-equation model (black line) that consists of sequential exponentially rising and decaying components, i.e., the rise time of the subsequent component equals the decay time of the prior. For more detail see section 9.1 of the Appendix. Dashed colored lines represent the components used in this model.
The population relaxation of the v = 1 state is faster than our time resolution (sub-100 fs) and follows essentially the cross-correlation of pump and probe pulses (green dashed line). The depopulation of the v = 1 state triggers rapid energy redistribution processes (red dashed line) in the excited molecule, where it is likely that several intramolecular modes

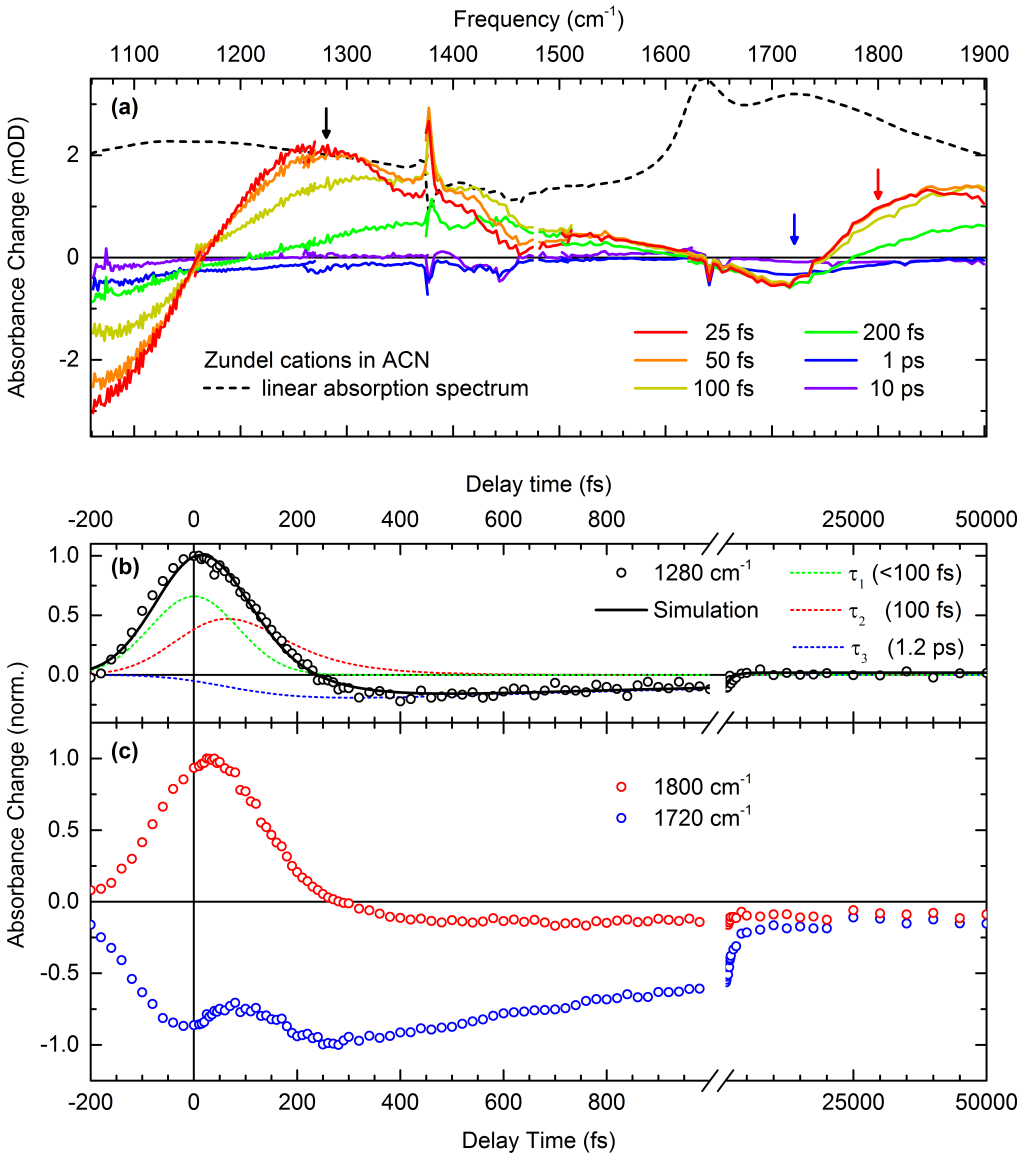

Figure 5.5: **(a)** Transient infrared absorption spectra (colored lines) of Zundel cations in acetonitrile for fixed pump-probe delays in a range from 25 fs to 10 ps. The absorbance change ΔA is detected for probe frequencies from 1060-1900 cm^{-1}. The scaled steady state absorption spectrum of 0.5 M HI (57%) diluted in ACN, after solvent subtraction, is shown by the dashed black line. **(b)** Kinetic transient taken at the maximum position of the ESA signal indicated by the black arrow in (a). The absorbance change is plotted as a function of pump-probe delay. The experimental data (open circles) was fit to the rate-equation model described in section 9.1 of the Appendix (black line). De-convolution of the simulation into the contributing components is shown by the dashed colored lines. **(c)** Kinetic transients taken at 1720 cm^{-1} and 1800 cm^{-1} indicated by the blue and red arrow in (a), respectively.

become transiently populated. The energy is eventually "dumped" into low frequency modes of the Zundel cation, such as the O· · ·O mode R, an a locally hot ground state is formed within ∼100 fs. The locally hot ground state, after resonant excitation of z, is characterized by an increase of vibrational temperatures of approximately 300 K ($k_BT = 208$ cm^{-1}). The locally hot ground state decays due to excess energy transfer from the excited molecule to the acetonitrile environment on a 1.2 ps time scale (dashed blue line).
The transient two-color pump-probe spectra show an interesting behavior for frequencies above 1500 cm^{-1}. We observe a comparably small bleaching signal at frequencies close to the Zundel OH bending vibration (at 1730 cm^{-1}). The temporal evolution of this feature displays both an instantaneous and a delayed response. Frequencies above 1750 cm^{-1} show an instantaneous response followed by a fast decay of the comparably large positive absorption feature.
Kinetic transients taken at 1720 cm^{-1} and 1800 cm^{-1} are summarized in Fig. 5.5c. The instantaneous response of the bleaching signal (blue symbols) indicates an anharmonic coupling of the OH bending vibration δ and the Proton transfer mode z. The delayed growth in signal strength is a consequence of the energy redistribution within the molecule after the initial population decay of z. The transient taken at 1800 cm^{-1} shows a markedly different kinetics that are very similar to the transient taken at 1200 cm^{-1}, indicating, that frequencies above 1750 cm^{-1} contain vibrational character of the proton transfer mode. These observations are in qualitative agreement with our picture of proton hydration in the $H_5O_2^+$ moiety, that will be explained in the following subsections.

Theoretical model: Ultrafast proton rattling and the origin of the absorption continuum

We now discuss the experimental results in terms of a 2D model that accounts for a fluctuating environment and the resulting forces imposed on the proton transfer mode[2]. The two-dimensional potential energy surface (2D-PES) of the proton transfer mode z and the O· · ·O mode R is displayed in Fig. 5.6a. An important observation, is the increasingly bimodal character of the 2D-PES with growing O· · ·O distance due to highly correlated motions of R and z. Fig. 5.6b shows cuts taken along z for different values of R in a range from 2.39-2.69 Å. The double minimum well potential shows no central barrier for R = 2.39 Å. If the O···O distance increases, a central barrier appears and grows quickly for larger O· · ·O separations. Consequently, R has a drastic effect on the shape of the proton potential, more precisely, R determines the height of the central barrier.
The observed blue shift of the v = 1 to 2 transition compared to the fundamental transition (v = 0 to 1) in our time-resolved experiments (cf. Fig. 5.3 & Fig. 5.5) is different from the behavior of a typical anharmonic oscillator (cf. Fig. 3.1 on page 24 and Fig. 3.5 on page 34) and is a direct manifestation of the proposed double minimum well character of the proton potential.
Fig. 5.7a shows the calculated vibrational potential of an isolated Zundel cation including the lowest four quantum state wavefunctions. Unlike an anharmonic potential, where the energy splitting ΔE of consecutive states becomes narrower according to the anharmonicity of the potential, in a double minimum well potential the energy splitting increases with each

[2] The theoretical results shown in this paragraph (Figs. 5.7-5.9 & Fig. 5.11) are evaluated on the CCSD(T)/aug-cc-pVTZ level of theory. Simulations have been performed in collaboration with the theory group of Dr. Benjamin Fingerhut. For more detail on the theoretical model see section 9.2 of the Appendix and references [146, 160] (supplementary information).

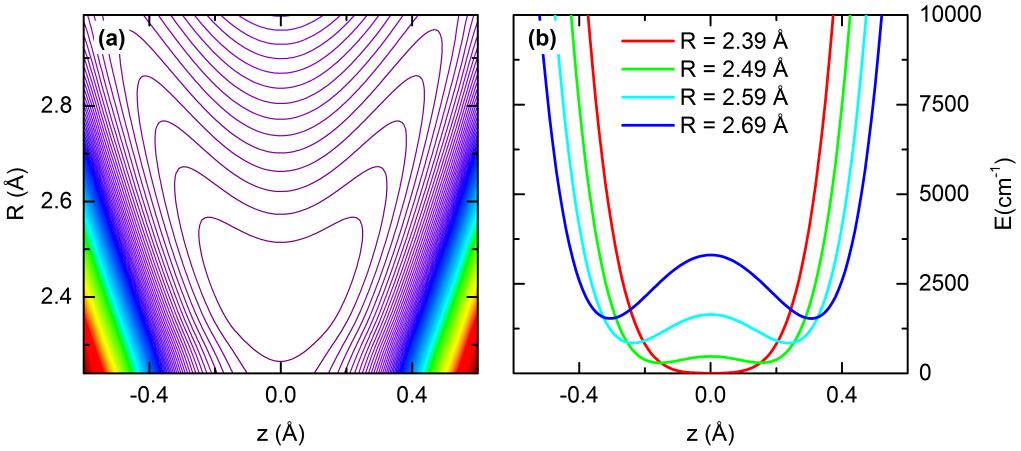

Figure 5.6: **(a)** Two-dimensional potential energy surface of the proton transfer mode z and the O···O mode R. **(b)** Cuts taken along the z axis of the 2D PES for different values of R. The central barrier of the potential rises with increasing O···O distance.

higher lying state according to the slope of the potential barriers. In the limiting case of a rectangular potential, consecutive states would split with n^2. Consequently, the energy difference ΔE for the v = 1 to 2 transition is larger than for the v = 0 to 1 transition and the ESA is blue shifted compared to the GSB & SE.
As evident from the calculated potential in Fig. 5.7a for an O···O distance R = 2.45 Å, even the vibrational ground state lies clearly above the potential barrier, resulting in the delocalization of the quantum state wavefunction of the v = 0 state of z. In other words, the proton H^+ can move barrier-less between the two flanking oxygen atoms in a Zundel cation $H_5O_2^+$ and the average position is exactly in the middle for the isolated molecule.

We now want to consider the fluctuating environment, acetonitrile, which undergoes structural fluctuations on a multitude of time scales with dominant contributions in the sub-100 fs range [161]. Such changes in the structure of the polar ACN environment translate into fluctuating electrical forces. Typical electrical fields that ACN exerts on the Zundel cation along the z-mode are reported in a range up to E_z = 30 MV/cm [162]. Due to the high polarizability of $H_5O_2^+$ [59], electrical fields perturb and deform the proton potential drastically.
The calculated vibrational potential for a static electric field of E_z = 25.7 MV/cm is shown in Fig. 5.7b. The shape of the potential displays a pronounced asymmetry but still retains the double-well character with a low barrier. For such asymmetric potentials, the central proton is in closer proximity to one of its flanking oxygen atoms compared to the other. Considering, that the electrical fields along z change on the femtosecond time scale, in accordance to the structural fluctuations of the polar acetonitrile, the proton rattles in between the two flanking water molecules of the Zundel cation very rapidly. These proton motions manifest in the broad and homogeneous bands observed in our 2D-IR experiments (Fig. 5.3b).
We further explore the effect of the solvent driven proton rattling and concomitant modulation of the potential energy surface of z and R on the transition frequency of different intramolecular vibrational modes. Calculated transition frequencies and IR cross sections

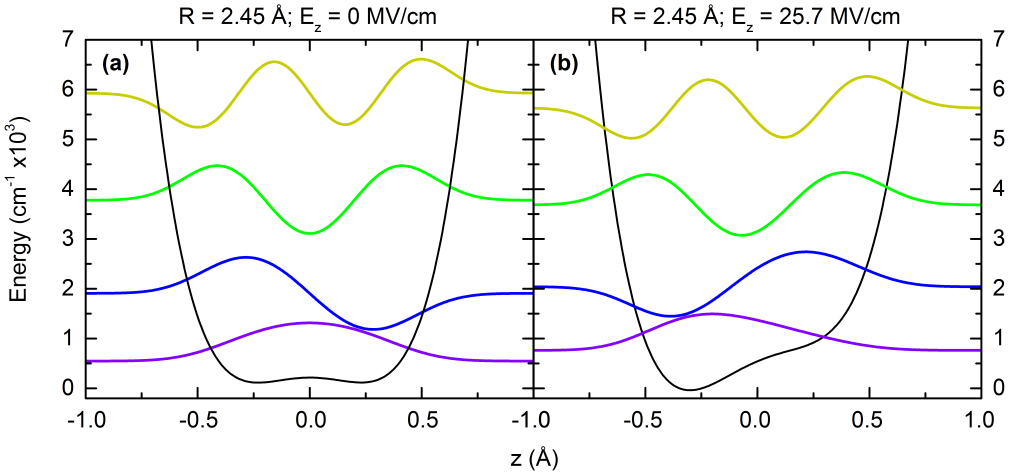

Figure 5.7: Calculated potential of a proton shared in a $H_5O_2^+$ moiety for an O···O distance R = 2.45 Å, including the first four quantum state wave functions: **(a)** for the isolated molecule; **(b)** for an external field of E_z = 25.7 MV/cm.

for several vibrational transitions are displayed in Fig. 5.8b and c as a function of the external field E_z in the direction of z, respectively.
Distortions of the proton potential by fluctuating electrical forces (Fig. 5.8a) are linked to strong frequency excursions of the fundamental transition of the proton transfer mode ($z_{0\to1}$, red line), its overtone transition ($z_{0\to2}$, orange line) as well as a combination tone (CT) ($zR_{0\to CT}$, blue line) with the O···O mode fundamental R. These transitions have appreciable IR cross sections with a limited change (less than 30 %) over the investigated range of E_z (red, orange and blue dashed lines). However, the IR intensity of the CT transition ($zR_{0\to CT}$) diminishes for external fields larger than 15 MV/cm. The fundamental ($R_{0\to1}$, yellow line) and overtone transition ($R_{0\to2}$, green line) of R show a negligible field dependence and IR cross sections.
At this point it should be made clear that the proton, whilst approaching one of the oxygen atoms temporarily, does not localize in the form of H_3O^+. In order to form the hydronium core, the central barrier must be higher in energy than the vibrational ground state of the proton transfer mode z, creating a minimum configuration for the proton to reside in. The height of the barrier depends critically on the distance of the two oxygen atoms and the v = 0 state remains above the barrier for $R \leq 2.5$ Å. Our theoretical results for $H_5O_2^+$ in acetonitrile determine an equilibrium average of $R \leq 2.5$ Å and agree well with the values of R = 2.40-2.55 Å reported in [23, 102] for the Zundel cation in the liquid phase.
We further investigated the influence of the environment on the O···O mode by calculating the field-fluctuation correlation function (FFCF) of acetonitrile (black line) and the time correlation function (TCF) of R (red line) from a 320 ps QM/MM trajectory (Fig 5.9a). The FFCF of the electrical field E_z that ACN exerts on the excess proton H^+ displays a fast initial decay within 200 fs followed by slower kinetics extending into the picosecond regime. Our simulations of the FFCF are in excellent agreement with the experimental data acquired by Ruthmann et al. [31]. The TCF of the O···O mode (red line) shows large amplitude oscillations with its intrinsic oscillation period of 55 fs, that become strongly damped after the initial decay of the FFCF of ACN. This behavior indicates that R is

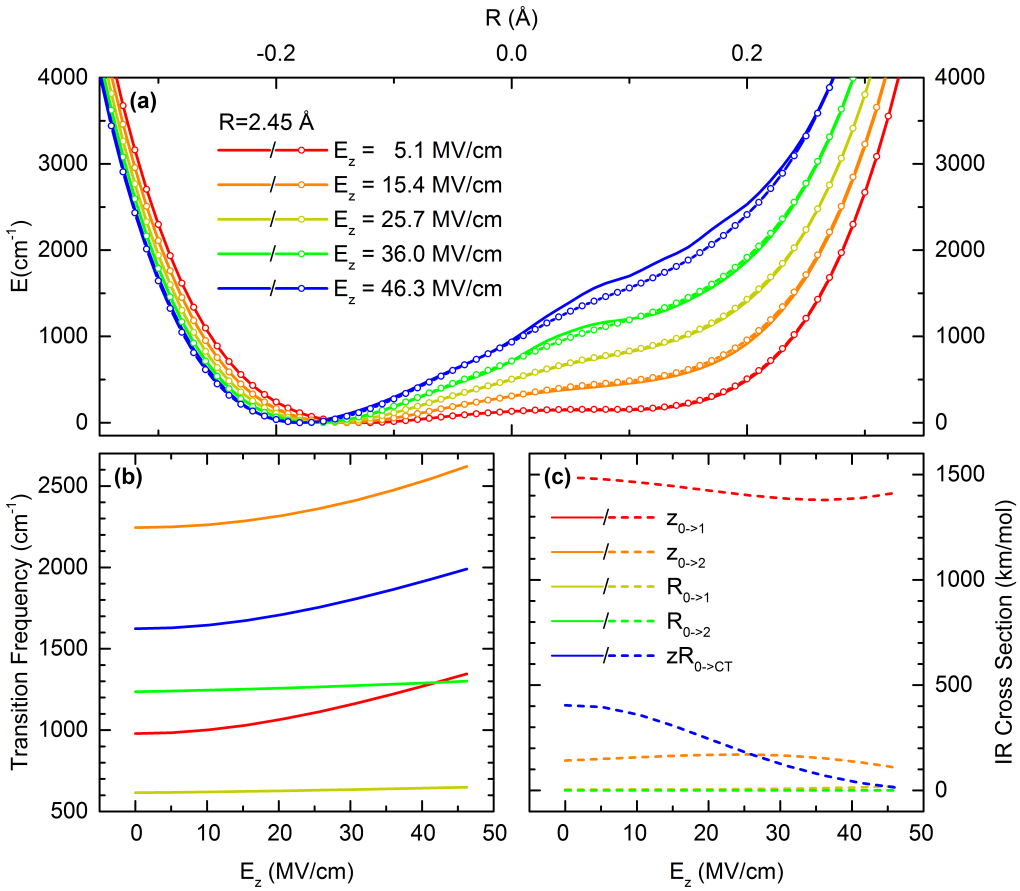

Figure 5.8: **(a)** Calculated potential of the shared proton in a $H_5O_2^+$ moiety for a fixed O$\cdots$O distance $R = 2.45$ Å and varying external field strengths E_z. Results obtained from a perturbative approach (solid lines) are plotted versus results obtained from a non perturbative approach (symbol lines). **(b)** Calculated transition frequencies for different intramolecular vibrational transitions including z and R (legend in (b)) plotted as a function of external field E_z along the proton transfer mode. **(c)** Calculated IR cross sections for the vibrational transitions shown in (a) plotted as a function of E_z.
Abbreviations: CT − combination tone

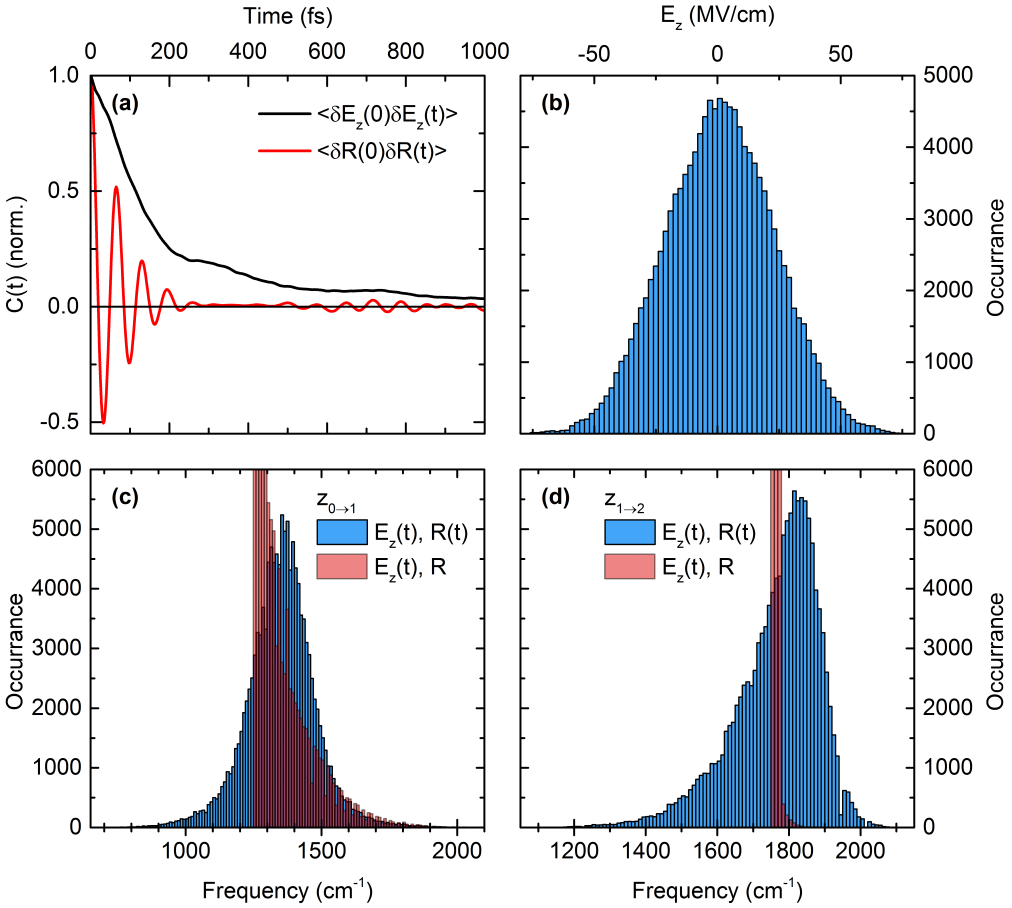

Figure 5.9: **(a)** Field-fluctuation correlation function (black line) of the external electrical field E_z that the polar acetonitrile molecules exert on the position of the shared proton, calculated from the QM/MM trajectory. **(b)** QM/MM trajectory averaged distribution of E_z at the position of the shared proton. **(c, d)** Frequency distributions of the fundamental transition z_{01} and excited state absorption z_{12} of the proton transfer mode z calculated including fluctuations in E_z and R (blue distribution) and calculated including fluctuations in E_z with a static O···O distance $R = 2.43$ Å (red distribution).

coupled to the environment. Further, changes in the O···O distance R are dictated by the acetonitrile molecules surrounding the Zundel cation.
Modulations in the O···O distance amplify the frequency excursions shown in Fig. 5.8a due to the strong impact on the shape of the proton potential (cf. Fig. 5.6). At ambient conditions, stochastic thermal excitation of R will lead to a change in the O···O distance of approximately 0.1 Å.
In combination with the strong frequency excursions due to fluctuations in E_z, these two effects lead to continuous absorption in a range from 1000-2600 cm^{-1}, thus explaining the observed absorption continuum of Zundel cations in acetonitrile (cf. Fig. 5.2).
It should be noted that the transition frequencies of $z_{0\to1}$, $z_{0\to2}$ and $zR_{0\to CT}$ shift almost identically with increasing external field (cf. Fig. 5.8b), thus the overtone and combination tone transition inherit the field dependence from the fundamental transition of z. As a result, the excited state absorption transition of z ($z_{1\to2} = z_{0\to2} - z_{0\to1}$) does not show a de-

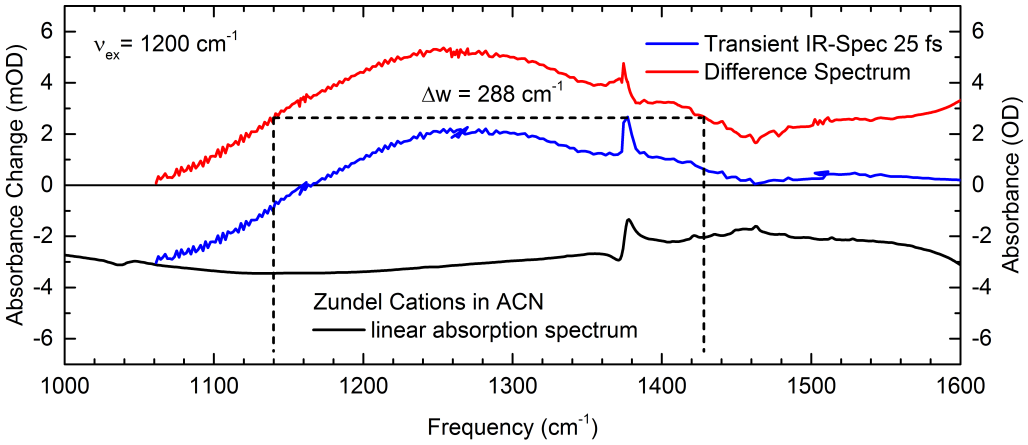

Figure 5.10: Adapted from [160]. Contributions from the fundamental transition of z are subtracted from the transient infrared absorption spectrum taken at a pump-probe delay time of 25 fs (blue line), estimated by the scaled and inverted linear absorption spectrum (black line). The "pure" lineshape of the ESA has an estimated FWHM of Δw = 288 cm^{-1}.

pendence on the external field E_z and as an important consequence, the measured transient lineshape in our time-resolved experiments is in a first approximation lifetime broadened.

In order to verify this assumption, we calculate the frequency distribution for the fundamental ($z_{0\to1}$) and excited state absorption ($z_{1\to2}$) transition of z including fluctuations in E_z and R and compare these results to calculations with a static O$\cdots$O distance of 2.43 Å (Fig. 5.9c,d). For the fundamental transition , frequency excursions are to a large extent caused by the fluctuating electrical forces along z and broadening due to fluctuations in the O$\cdots$O distance R are minor (Fig. 5.9c, blue vs. red distribution). The $z_{1\to2}$ transition displays a different behavior. For a static O$\cdots$O distance of 2.43 Å almost no frequency broadening occurs (red distribution in Fig. 5.9d), thus frequency broadening is caused by varying distances in R.
These results suggest that inhomogeneities of O$\cdots$O arrangements are more clearly revealed in the ESA component, in agreement with the observations of Fig. 5.3 & Fig. 5.4 on pages 70 & 71, respectively.
As discussed in the prior section, the ESA transition of z is insensitive to the external field fluctuations, thus variances in E_z do not contribute to the observed transient lineshape. Assuming pure lifetime broadening of the ESA allows us to derive a lower bound for the vibrational lifetime of the v = 1 state of the proton transfer mode.
Similar to Fig. 4.6 on page 61, we subtract the scaled and inverted linear absorption spectrum (black line in Fig. 5.10) from the transient infrared absorption spectrum taken at a delay time of 25 fs to estimate the contribution of the GSB & SE between the v = 0 to 1 transition to the lineshape of the ESA. From the "pure" lineshape of the ESA we deduce a width of Δw = 288 cm^{-1}. In the homogeneous limit (cf. subsection 3.1.2 on page 26), lifetime and linewidth are connected by:

$$\tau_1 = \frac{1}{2\pi\Delta w} \ , \tag{5.1}$$

leading to a lower bound of the vibrational lifetime of ∼20 fs. For the upper bound of τ_1,

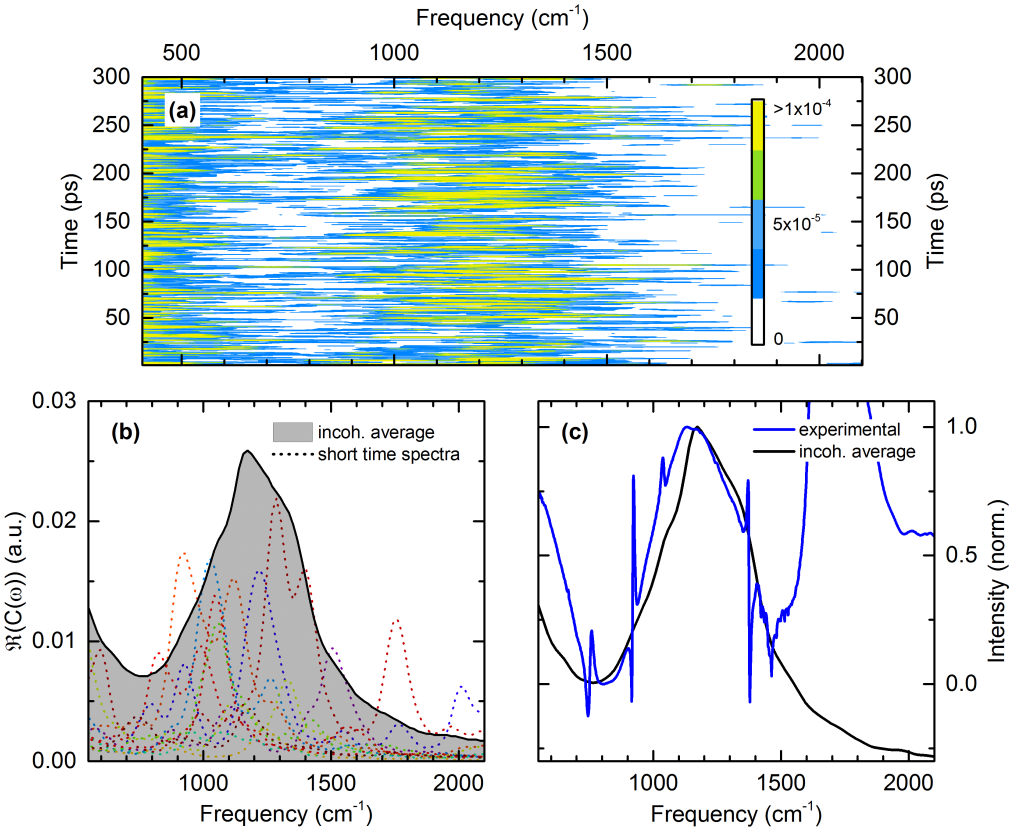

Figure 5.11: **(a)** Short time spectra calculated from the QM/MM trajectory for Δt = 1 ps segments plotted as a function of time and frequency. **(b)** Short time spectra taken from (a) and plotted as a function of $\Re(C(\omega))$ and frequency (colored dotted lines). The incoherent average of 300 short time spectra is shown by the gray area. **(c)** Comparison of the experimental steady state absorption spectrum of Zundel cations in ACN (blue line) and the incoherent average of 300 short time spectra (black line) taken from (b).

limited spectral diffusion caused by fluctuations in R is considered. The Voigt profile of the v = 1 to 2 transition of the proton transfer mode shown in Fig. 5.9d is deconvoluted into homogeneous and inhomogeneous contributions, resulting in a homogeneous width of 150 cm^{-1} and an upper bound for the vibrational lifetime of ∼40 fs.
Short time spectra calculated from our QM/MM trajectory allow to map the influence of the femtosecond proton movement and changes in the O$\cdots$O distance on the vibrational spectrum of the fundamental transition (z_{01}) of z.
A series of short time spectra covering an interval Δt of 1 ps each, are shown as a function of frequency in Fig. 5.11b and are taken from different segments of the QM/MM trajectory. The spectral position, width and intensity of the short time spectra are strongly modulated by the influence of the ACN environment and represent particular arrangements of the $H_5O_2^+$ geometry.
An important finding is that the v = 0 to 1 transition of the proton transfer mode explores most of the linewidth within 1 ps, the typical lifetime of a hydrogen bond in bulk water [26]. Comparing the incoherent average of 300 short time spectra (solid black line in Fig. 5.11b,c)

with the experimental steady state absorption spectrum, displays good agreement in frequency position and to a large extent in spectral width.

5.2.2 Vibrational Dynamics of the Flanking Water Molecules in the Zundel Cation

In the previous subsection, the genuine proton degree of freedom was investigated by means of 2D-IR spectroscopy, two-color pump-probe spectroscopy and theoretical simulations. The absorption continuum of Zundel cations in ACN was explained by fluctuating electrical forces exerted by the acetonitrile environment modulating the proton potential on the femtosecond time scale, leading to strong frequency excursions of associated vibrational transitions. Additionally, fluctuations in the O$\cdots$O distance R in the $H_5O_2^+$ moiety contribute to the line broadening by their impact on the shape of the proton potential.
The model described above predicts a different vibrational character of the continuum absorption compared to the OH stretching and bending vibrations of the flanking water molecules in $H_5O_2^+$. This can be tested by two-color pump-probe experiments in the range of the OH stretching and OH bending vibrations of Zundel cations in ACN, where characteristic transient vibrational signatures are mapped in time.

OH stretching vibration and absorption continuum

Resonant excitation of the symmetric and asymmetric OH stretching vibrations of Zundel cations in ACN (cf. Fig 5.2) leads to the transient infrared absorption spectra shown in Fig. 5.12b. It should be noted that the symmetric and asymmetric OH stretching vibrations cannot be discerned in the IR experiments contrary to water monomers diluted in ACN (chapter 4) and for the sake of simplicity are from now on referred to as OH stretching vibration. A strong bleaching feature is observed in the frequency interval ~3250-3600 cm^{-1} due to the ground state bleach and stimulated emission between the v = 0 to 1 transition of the OH stretching oscillator. The excited state absorption on the v = 1 to 2 transition is observed at frequencies below 3250 cm^{-1}.
Fig. 5.13a displays the kinetic transients taken at the maximum of the bleaching (black arrow in Fig. 5.12b) and enhanced absorption feature (red arrow in Fig. 5.12b). The experimental data was numerically fit to a rate-equation model, accounting for population relaxation of the OH stretching vibration, energy redistribution within the molecule leading to the formation of a locally hot ground state and the energy transfer from the excited Zundel cation to the acetonitrile environment (cf. section 9.1 of the Appendix).
The ESA signal (red circles) displays an initial population relaxation within the time resolution of the experiment, setting an upper limit of $\tau_1 = 50$ fs for the vibrational lifetime of the v = 1 state of the OH stretching oscillator. Subsequent energy redistribution in the Zundel cation leads to the formation of a locally hot ground state within a few hundred femtoseconds (cf. Table 5.1) followed by slower kinetics on the picosecond time scale. The decay of the locally hot ground state with a $\tau_2 = \sim 2.5$ ps time scale accounts for the transfer of excess energy to acetonitrile molecules in the environment of the excited Zundel cation. We find similar kinetics for the time evolution of the bleaching signal (black open circles, cf. Table 5.1) with the thermal contributions more pronounced. It should be noted that in case of the bleaching signal an additional component was added to the model accounting

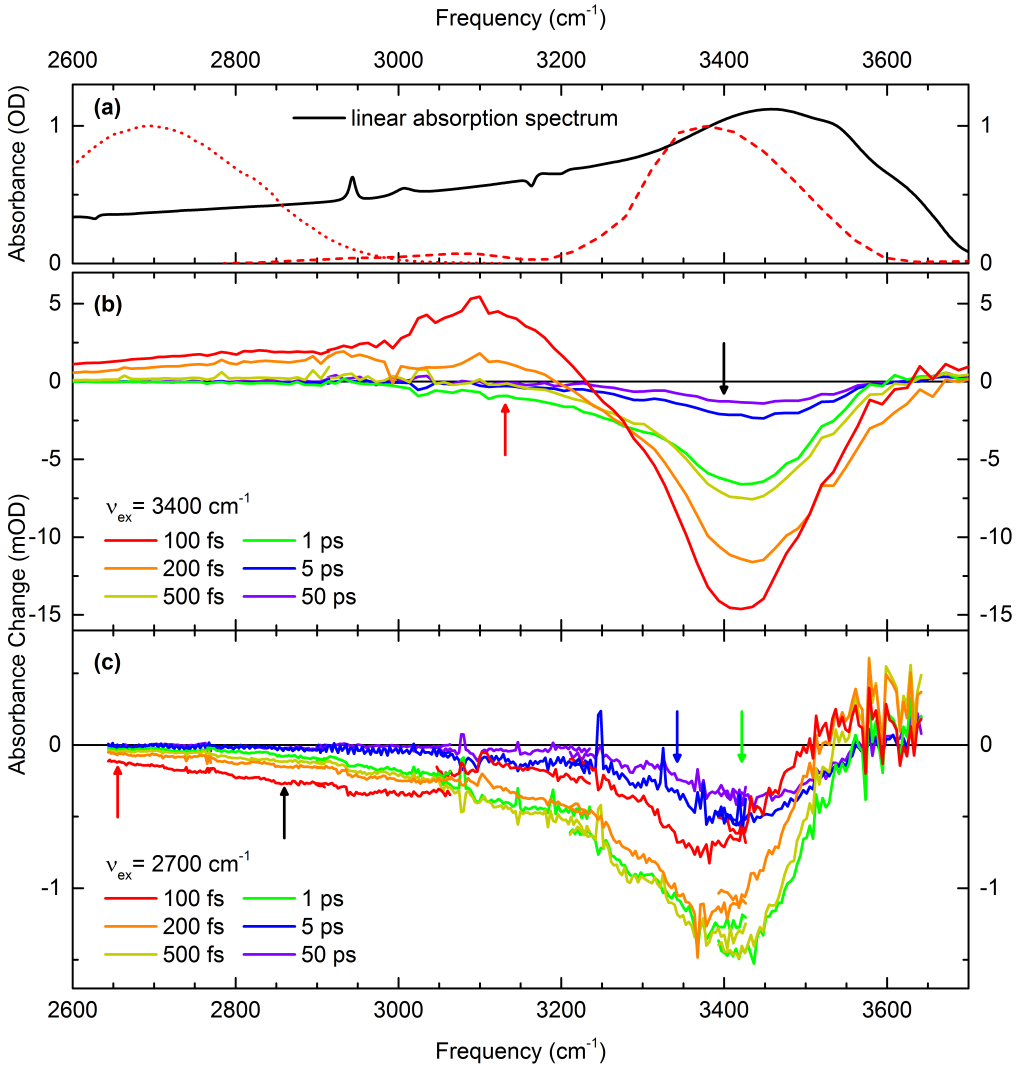

Figure 5.12: Adapted from [146]. **(a)** Steady state absorption spectrum (black line) in the range of the OH stretching vibration of Zundel cations selectively prepared in acetonitrile . Excitation of the Zundel continuum with pump pulses centered at 2700 cm^{-1} and the OH stretching vibration with pump pulses centered at 3400 cm^{-1} are indicated by the dotted and dashed red line, respectively. **(b)** Transient infrared absorption spectra after resonant OH stretching excitation. The absorbance change ΔA is plotted as a function of probe frequency for fixed pump-probe delay times in a range from 100 fs to 50 ps. **(c)** Same as (b) but for excitation of the Zundel continuum with pulses centered at 2700 cm^{-1}. Colored arrows in (b) and (c) indicate the frequency positions of the kinetic transients displayed in Fig. 5.13a and (b), respectively.

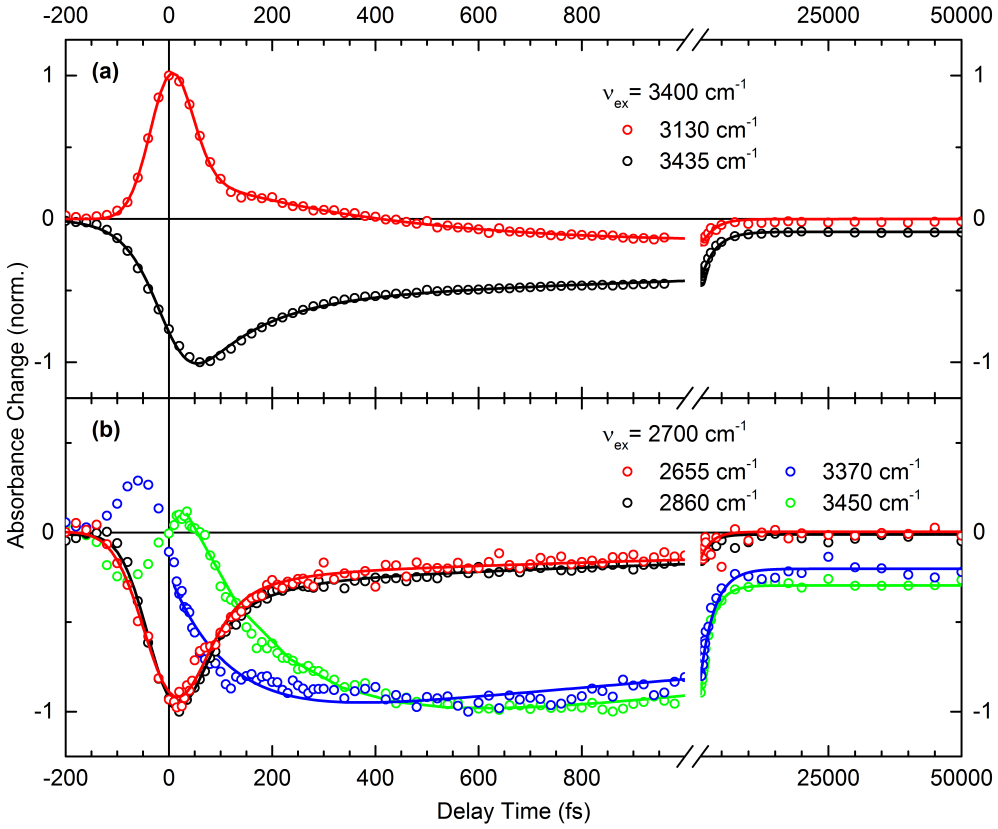

Figure 5.13: Adapted from [146]. **(a)** Kinetic transients taken at the maximum signal position of the enhanced absorption (red symbols) and bleaching feature (black symbols) after resonant OH stretching excitation (indicated by the colored arrows in Fig. 5.12b). The absorbance change ΔA (normalized) is plotted as a function of pump-probe delay and characteristic time constants are retrieved by numerical fits (solid lines) with the rate-equation model described in section 9.1 of the Appendix. **(b)** Same as (a) but for excitation of the Zundel continuum with pulses centered at 2700 cm^{-1}. Frequency positions are indicated by the colored arrows in Fig. 5.12c)

for a perturbed free induction decay at negative delay times [118].
In order to verify the vibrationally different character of the OH stretching vibration at approximately 3400 cm^{-1} and the continuous absorption below 3000 cm^{-1}, we performed a second set of measurements with the excitation pulse centered at 2700 cm^{-1}. Transient infrared absorption spectra are shown in Fig. 5.12c. We observe a quasi instantaneous absorption decrease for frequencies below ∼3100 cm^{-1} and a delayed absorption decrease for the frequency interval 3100-3500 cm^{-1}. Enhanced absorption is observed for frequencies above 3500 cm^{-1}.
In order to understand the different transient signatures we investigate the dynamic transients taken at different frequency positions indicated by the colored arrows in Fig. 5.12c. The quasi instantaneous signal for frequencies below 3100 cm^{-1} decays within the time resolution of the experiment ($\tau_1 < 65$ fs) followed by fast energy redistribution within the molecule ($\tau_2 = \sim$85 fs) and energy transfer to the solvent with a 2 ps time constant (τ_3). Frequencies higher than 3100 cm^{-1} show an increasingly more delayed rise in signal strength

until 3500 cm^{-1} and end up in long-lived heating signals. Both the kinetic transients taken at 3370 cm^{-1} and 3450 cm^{-1} show a sub-picosecond rise in signal strength reflecting intramolecular energy redistribution and the formation of a locally hot ground state and slower kinetics on the picosecond time scale accounting for energy transfer to the environment.
This delayed response discerns the vibrational character of the continuous absorption below 3000 cm^{-1} from the OH stretching vibration at 3400 cm^{-1}, the latter not directly excited by the pump pulses centered at 2700 cm^{-1}. The sub-picosecond rise of signal strength for frequencies above 3100 cm^{-1} is a hallmark of the locally hot ground state where low-frequency modes of the Zundel cation, such as the O···O mode R are populated. These modes couple anharmonically to the OH stretching vibration of $H_5O_2^+$, leading to a blue shifted v = 0 to 1 transition of the latter as evident from the delayed bleaching signal and especially from the enhanced absorption for frequencies above 3500 cm^{-1}.
The absorbance change for frequencies above 3500 cm^{-1} is positive, as we measure differential signals in our time-resolved experiments and due to the blue shift of the v = 0 to 1 transition we now have a higher fraction of species absorbing at frequencies above 3500 cm^{-1}, thus leading to an enhanced absorption feature (cf. Fig. 5.12b vs. Fig. 5.12c).

OH bending vibration

Transient infrared absorption spectra with resonant excitation of the OH bending mode δ of the water molecules in $H_5O_2^+$ (cf. Fig 5.2) are displayed in Fig. 5.14a.
An instantaneous bleaching feature is observed for the frequency interval 1630-1850 cm^{-1} due to the ground state bleach on the v = 0 state and the stimulated emission from the v = 1 state of the OH bending oscillator. Enhanced absorption is observed for frequencies below 1630 cm^{-1} due to the excited state absorption on the v =1 to 2 transition. Additionally, frequencies above 1850 cm^{-1} show unstructured enhanced absorption that has no intuitive interpretation in regards of the OH bending motion.
To investigate the vibrational energy relaxation of the OH bending oscillator in $H_5O_2^+$ and to characterize the enhanced absorption above 1850 cm^{-1}, kinetic transients taken at the maximum of the ESA, GSB & SE and in the enhanced absorption at 2000 cm^{-1} are compared in Fig. 5.14b. In agreement with our prior investigations on the proton transfer mode and the OH stretching vibration in $H_5O_2^+$, we are able to simulate the experimental data for the kinetic transients taken at 1585 cm^{-1} and 1725 cm^{-1} with 3 time constants. Population relaxation of the OH bending oscillator is faster than our time resolution, setting an upper limit of $\tau_1 = 60$ fs. Subsequent energy redistribution occurs on a 300 fs (τ_2) time scale, leading to a locally hot ground state that decays on a $\tau_3 = 1.6$ ps time scale where the energy is transferred from the excited Zundel cation to the acetonitrile environment. We find nearly identical time constants for the ESA and GSB & SE signals, with the thermal contributions more pronounced in the latter. Additionally, a perturbed free induction decay was added at negative delay times for the kinetic transient taken at 1725 cm^{-1}.
The enhanced absorption at 2000 cm^{-1} displays a rise in signal strength until ∼150 fs followed by a mono exponential decay with a $\tau_3 = 1.5$ ps time constant. This dynamic behavior can be explained as follows. The population relaxation of the v = 1 state of the bending oscillator after resonant excitation leads to rapid energy redistribution processes within the molecule transiently populating the proton transfer mode z. This behavior manifests in the delayed rise of signal strength until ∼150 fs for frequencies above 1900 cm^{-1}, as the Zundel continuum is directly connected with the proton transfer mode z. The mono

exponential decay of the signal reflects the energy transfer from the excited Zundel cation to the ACN environment.

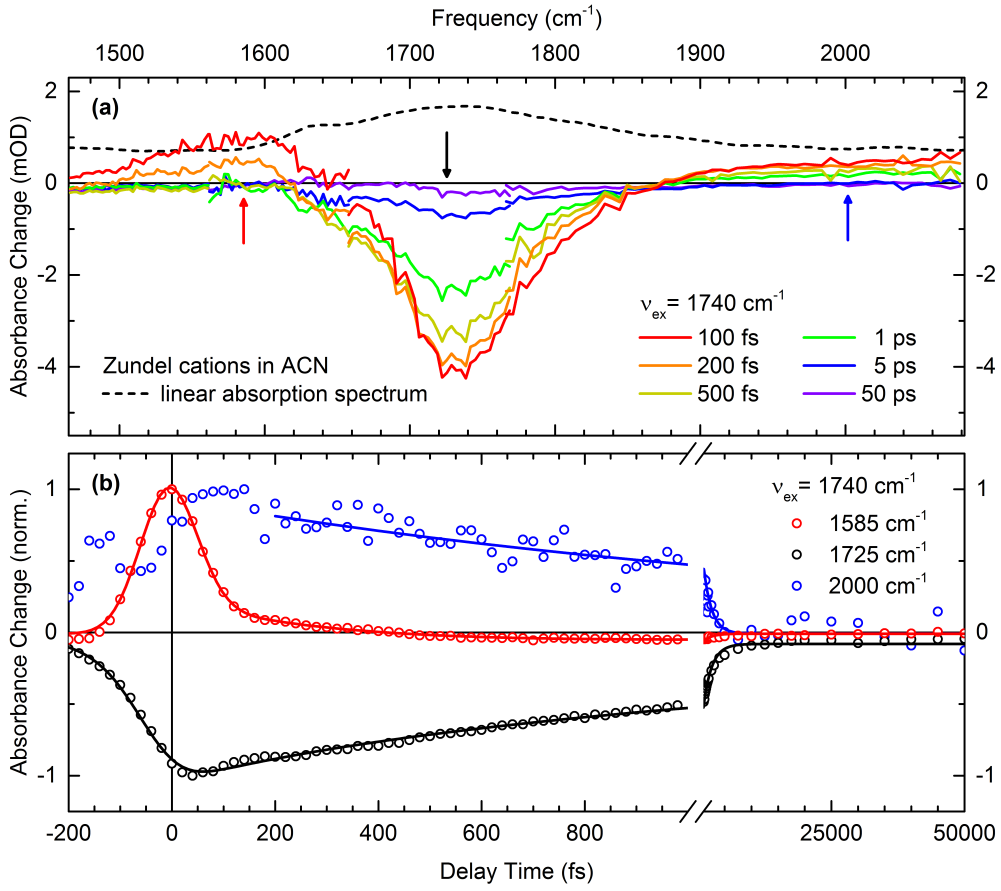

Figure 5.14: Adapted from [146]. **(a)** Transient infrared absorption spectra after resonant OH bending excitation. The absorbance change ΔA is plotted as a function of probe frequency for fixed pump-probe delay times in a range from 100 fs to 50 ps. **(b)** Kinetic transients taken at the frequency positions indicated by the colored arrows in (a)). The absorbance change ΔA (normalized) is plotted as a function of pump-probe delay and characteristic time constants are retrieved by numerical fits (solid lines).

OH stretch to bend coupling

In accordance with chapter 4, OH stretch to bend relaxation was investigated by means of two-color pump-probe spectroscopy. As discussed in subsection 2.1.2 on page 16, the OH stretching vibration of bulk liquid water relaxes after resonant excitation in a cascade like mechanism including the OH bending overtone, the bending fundamental transition and the librational manifold. We have shown that a very similar mechanism explains the vibrational energy relaxation in water monomers diluted in acetonitrile (subsection 4.4.2 of chapter 4).

For water monomers in ACN, the symmetric and asymmetric OH stretching vibrations are clearly distinguishable in the steady state absorption spectrum and an energy gap of approximately 350 cm^{-1} between the bending overtone and the symmetric OH stretching

vibration hampers VER.
For Zundel cations selectively prepared in acetonitrile, the OH bending overtone at approximately 3480 cm^{-1} and the OH stretching fundamental at 3400 cm^{-1} are nearly in resonance, thus stretch to bend relaxation rates should be extremely high.
Transient infrared absorption spectra in the range of the OH bending vibration of $H_5O_2^+$ after OH stretching excitation are shown in Fig. 5.15a. We observe a quasi-instantaneous enhanced absorption for frequencies below 1680 cm^{-1}, a direct manifestation of the anharmonic coupling of the OH bending oscillator to the OH stretching oscillator. It should be noted, that population transfer from the v = 1 state of the OH stretching vibration to the v = 2 state of the OH bending vibration is expected due to their near resonance. However, such transient signals cannot be observed in our measurements as the time resolution is not sufficient to resolve the involved vibrational lifetimes. The delayed absorption decrease in the range from ∼1650-1900 cm^{-1} is complete at ∼250 fs and a hallmark for the sub-

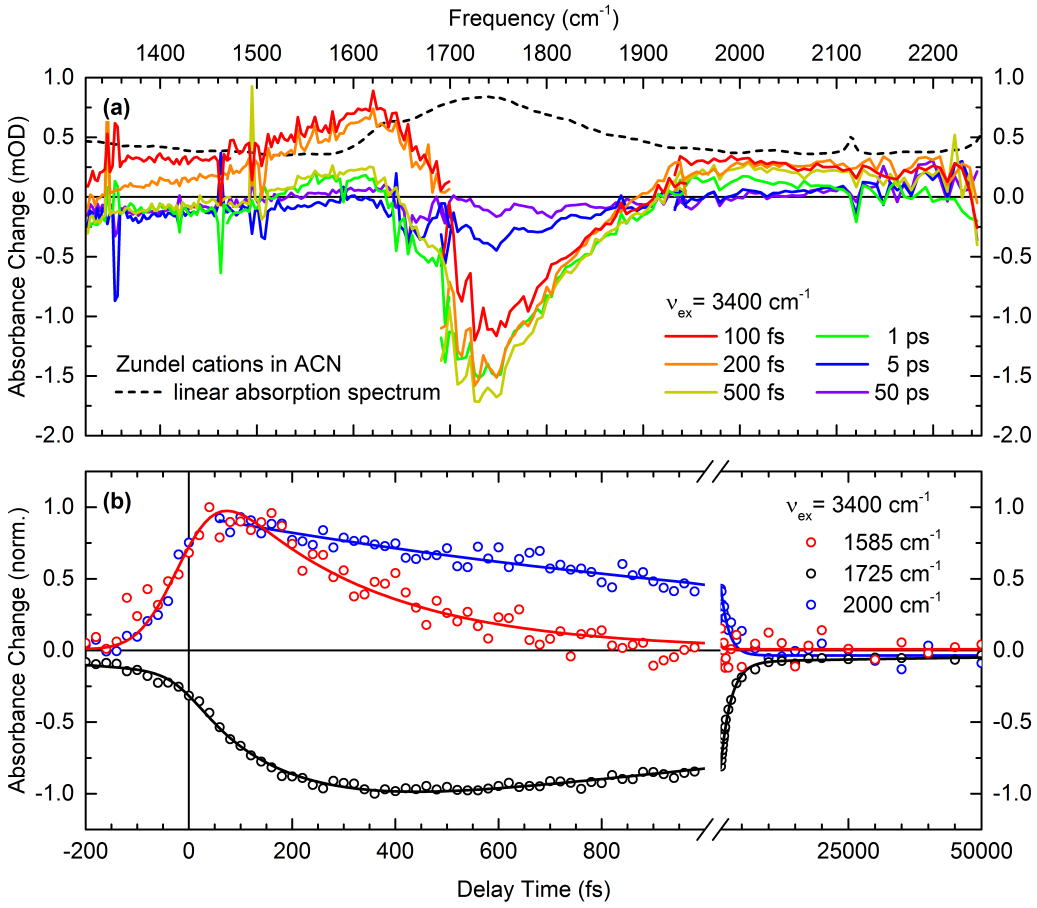

Figure 5.15: Adapted from [146]. **(a)** Transient infrared absorption spectra after resonant OH stretching excitation. The absorbance change ΔA is plotted as a function of probe frequency for fixed pump-probe delay times in a range from 100 fs to 50 ps. **(b)** Kinetic transients taken at the frequency positions indicated by the colored arrows in (a). The absorbance change ΔA (normalized) is plotted as a function of pump-probe delay and characteristic time constants are retrieved by numerical fits (solid lines).

picosecond formation of the locally hot ground state. This behavior is strongly determined by the decay rate of the OH stretching vibration into low frequency modes of the excited Zundel cation. The observed spectral broadening of the bleaching feature with increasing delay time is a consequence of its slower time evolution compared to the enhanced absorption for frequencies below 1680 cm^{-1}, leading to a smaller signal overlap at delay times >200 fs.

For frequencies above 1900 cm^{-1}, we observe a featureless enhanced absorption, similar to our measurements with resonant OH bending excitation. This signal can be explained in the same way and reflects the energy redistribution within the excited molecule and the transient population of the proton transfer mode and decays with the same 1.5 ps time constant found in the experiment with resonant OH bending excitation.

In the range of the OH bending fundamental ($\sim$1630 cm^{-1}) of water monomers in our sample, a pronounced absorption decrease is observed at delay times greater than 3 ps. This behavior is a consequence of the simultaneous excitation of the OH stretching vibrations of water monomers in our sample by the broad pump pulse centered at 3400 cm^{-1}, leading to the vibrational signatures on the OH bending oscillator explained in chapter 4.

Our two-color pump-probe experiments clearly discern the vibrational character of OH stretching and OH bending vibrations from the absorption continuum. We find vibrational lifetimes of the v = 1 state of the OH stretching and bending vibration in $H_5O_2^+$ to be in the sub-100 fs range, much faster than in bulk liquid water [52]. Ottosson et al. [163] recently found similar time scales for the OH stretching vibration of Zundel cations in an acetonitrile environment.

The extraordinarily fast decay rates are facilitated by a pronounced resonance of the OH bending overtone with the OH stretching vibration and the Zundel absorption continuum, that spans several thousand wavenumbers and acts as an excellent acceptor of vibrational excess energy.

Table 5.1: Time constants derived from a rate-equation analysis (cf. section 9.1 of the Appendix) of the measured pump-probe transients (ν_{ex}: pump frequency, ν_{pr}: probe frequency). τ_1 represent population decay times and τ_2 describes the subsequent energy redistribution within the excited Zundel molecule leading to the formation of a locally hot ground state. The decay time τ_3 of the locally hot ground state represents energy transfer from the excited Zundel cation to the ACN environment. Additional transient signals at negative delay times were accounted by τ_{PFID}, describing a perturbed free induction decay.
[a] The amplitude of this component is very small and the time constant has to be taken with care.

	Zundel cations in ACN			
	τ_1 (fs)	τ_2 (fs)	τ_3 (fs)	τ_{PFID} (fs)
$\nu_{ex} = 1200$ cm^{-1}				
$\nu_{pr} = 1280$ cm^{-1}	20-40 ± 10	100 ± 20	1200 ± 100	-
$\nu_{ex} = 1740$ cm^{-1}				
$\nu_{pr} = 1585$ cm^{-1}	<60 ± 10	300 ± 30	1500 ± 80	-
$\nu_{pr} = 1725$ cm^{-1}	<60 ± 10	300 ± 30	1600 ± 80	60 ± 5
$\nu_{pr} = 2000$ cm^{-1}	-	-	1500 ± 150	-
$\nu_{ex} = 2700$ cm^{-1}				
$\nu_{pr} = 2655$ cm^{-1}	<65 ± 10	80 ± 10	2000 ± 200	-
$\nu_{pr} = 2860$ cm^{-1}	<65 ± 10	85 ± 10	1800 ± 170	-
$\nu_{pr} = 3370$ cm^{-1}	-	115 ± 10	2600 ± 210	-
$\nu_{pr} = 3450$ cm^{-1}	-	190 ± 10	2000 ± 140	-
$\nu_{ex} = 3400$ cm^{-1}				
$\nu_{pr} = 1585$ cm^{-1}	-	290 ± 20	-	-
$\nu_{pr} = 1725$ cm^{-1}	-	185 ± 20	1900 ± 80	360 ± 30 [a]
$\nu_{pr} = 2000$ cm^{-1}	-	-	1500 ± 70	-
$\nu_{pr} = 3130$ cm^{-1}	<50 ± 10	470 ± 40	2300 ± 360	-
$\nu_{pr} = 3435$ cm^{-1}	<50 ± 10	120 ± 10	2700 ± 200	50 ± 5

6 Excess Protons in Water

The experimental investigation of excess protons in bulk liquid water has been a major challenge due to the structural heterogeneity of the system as outlined in chapter 2. Our results obtained for Zundel cations predominantly prepared in acetonitrile allow to benchmark the vibrational response of excess protons diluted in bulk liquid water. We focus on the range of the Zundel marker mode z and compare 2D-IR and two-color pump-probe spectra of protons in H_2O to $H_5O_2^+$ in ACN. For the first time, we are able to directly investigate the role of a prototypical species, specifically the Zundel cation, in water.

6.1 Stationary Vibrational Spectra

A concentration-dependent IR series of different water/acetonitrile mixtures with 1 M HI (67%) was collected in attenuated total reflection (Fig. 6.1, solid lines). The gap between HI diluted in pure CH_3CN and HI in H_2O was bridged by solutions with varying mole-fractions (m_f) of water and acetonitrile with a step size of $\Delta m_f = 0.1$. It should be noted, that the stock solution of HI (67%) inherently contains approximately 3.5 water molecules per acid molecule, thus a ratio of $m_f(H_2O)$ 0 : 1 $m_f(CH_3CN)$ is not possible. The extra amount of water induced by addition of acid to the solutions has been accounted for in the respective mole-fractions.
For HI (67%) in ACN (brown line), we observe the vibrational spectrum of Zundel cations selectively prepared in acetonitrile (cf. Fig. 5.2). With the addition of water to the solution, we observe changes in the ATR spectra, assigned to the appearance and subsequent growth of the absorption features of bulk water.
For ratios below $m_f(H_2O)$ 0.5 : 0.5 $m_f(CH_3CN)$ we find increased absorption in the range of the water OH stretching vibrations at ∼3000-3700 cm^{-1}, with negligible changes to the spectrum for frequencies below 3000 cm^{-1}. At ratios larger than $m_f(H_2O)$ 0.5 : 0.5 $m_f(CH_3CN)$ an additional absorption increase occurs in other parts of the spectrum.
These are the growth of the librational L2 band at 670 cm^{-1} [52], here observed as increased absorption below 1000 cm^{-1}, the high frequency tail of the librational absorption in a range from ∼1000-1750 cm^{-1} [52], the OH bending vibration at 1650 cm^{-1} and the combination band of the libration at ∼400 cm^{-1} with the OH bending mode appearing at 2100 cm^{-1} [47].
H_2O:CH_3CN solutions with the same molar ratios were recorded without addition of acid (dashed colored lines). Fig. 6.1b displays the characteristic absorption spectra of hydrated excess protons in the various H_2O:CH_3CN mixtures presented in (a), obtained as differential signals of according solutions with and without acid, respectively.
With the addition of water, we observe three effects: (i) An absorption decrease in the range of the OH stretching vibration of $H_5O_2^+$ due to the over-correction of the OH stretching

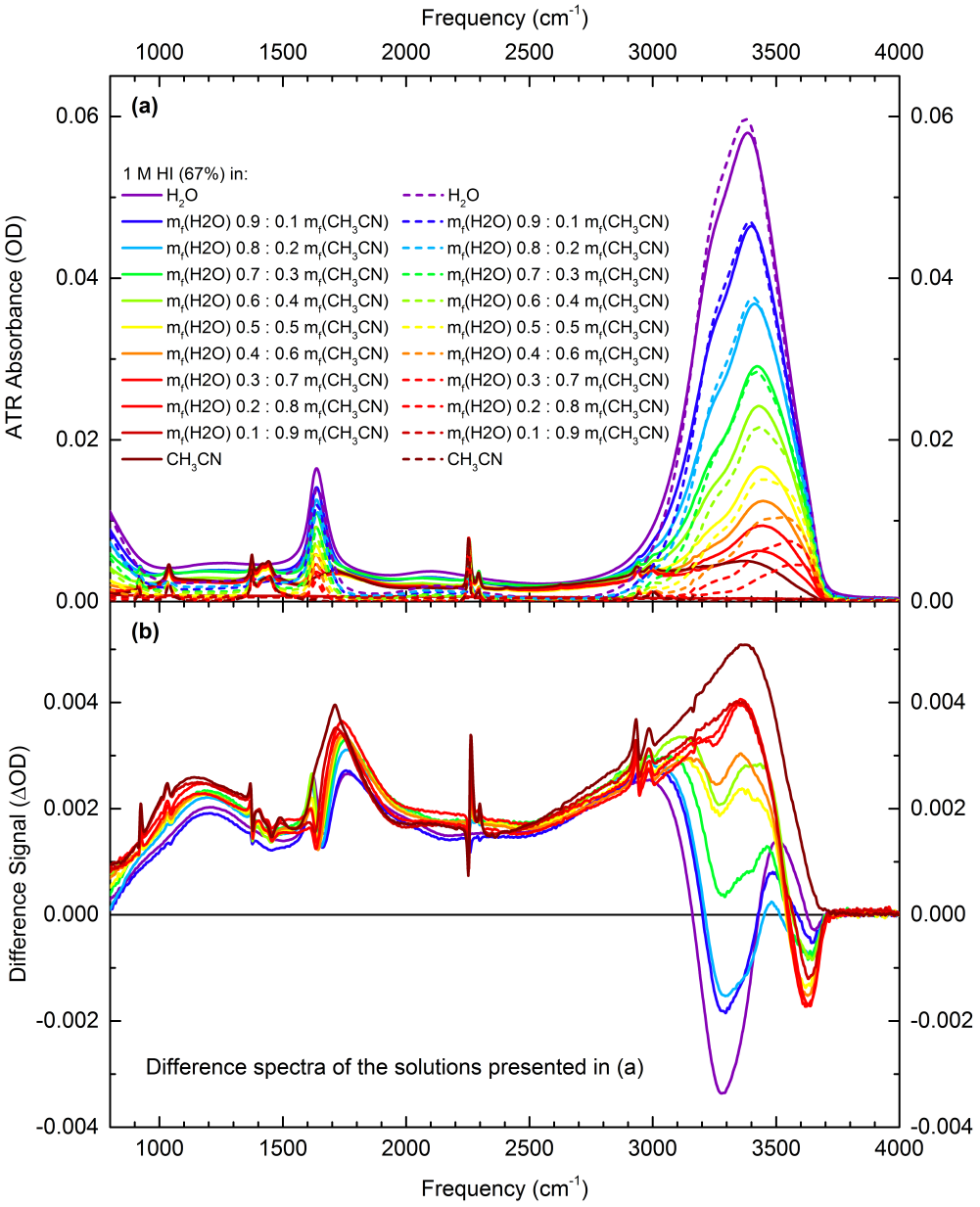

Figure 6.1: (a) ATR absorption spectra for 1 M HI (67%) diluted in different H_2O:CH_3CN mixtures (solid lines) and according mixtures without acid (dashed lines). Spectra were recorded for mixtures ranging from acid in pure water to pure acetonitrile with a step size of $\Delta m_f = 0.1$ ($m_f =$ mole fraction). It should be noted that HI (67%) diluted in CH_3CN inherently contains 3.5 H_2O molecules per acid molecule and a water free mixture is not possible with the acid used in the experiment. **(b)** Difference spectra for the solutions presented in (a). By subtraction of the H_2O:CH_3CN mixture without acid from the according counterpart with 1 M of acid, the characteristic absorption spectra of hydrated excess protons in the solution is revealed.

vibrations of bulk water molecules. This is a consequence of the weaker OH stretching absorption of water molecules directly solvating the protons in the solution, thus not contributing to the strong OH stretching absorption of bulk water as in the sample solution without acid. This leads to a net decrease of absorption strength in the differential signal; (ii) An absorption decrease and blue shift of the OH bending vibration at 1730 cm^{-1} of approximately 20 cm^{-1}. Additionally a new band appears in the differential signals at 1615 cm^{-1} due to the increasing solvation of the iodine counter ions in our samples, shifting the OH bending vibration of the involved water molecules; (iii) An absorption decrease and a blue shift of the proton transfer mode of approximately 40 cm^{-1}, consistent with the stronger field that water exerts on the hydrated excess proton as a dominant mechanism. However, the absorption decrease of the associated absorption features might be an indication of a decrease in Zundel type proton configurations. At this point it should be noted, that similar to the over-correction in the OH stretching range, one over-corrects the librational background in the differential signals as water molecules directly solvating the proton do not contribute, thus leading to a net absorption decrease for frequencies below $\sim$1750 cm^{-1}.
The overall peak absorption of the Zundel marker mode z diminishes continuously to approximately 80 % of its original value when going from HI in CH_3CN to HI in H_2O. This behavior is consistent with recent FTIR studies in the range of the proton transfer mode for Zundel cations in ACN and protons in water [160]. With the preposition that the spectral feature around 1200 cm^{-1} is caused by absorption of Zundel cations, we translate the decreased absorption in this region when comparing HI in ACN to HI in H_2O to an upper limit of 80 $\pm$ 20 % of Zundel type configurations for the hydrated proton in water [160]. It should be stressed, that steady state absorption studies as presented in Fig. 6.1 do not allow to discern the mechanisms contributing to the observed lineshapes and other hydrated proton species could in principle also contribute to the absorption observed in the range of 1000-1500 cm^{-1}.

6.2 2D-IR and Pump-Probe Data

We applied 2D-IR spectroscopy in the range of the proton transfer mode in the limiting cases of excess protons in water and Zundel cations selectively prepared in acetonitrile. Absorptive 2D-IR spectra for different waiting times T (0, 25, 50, 100 fs) are summarized in Fig. 6.2. Red to yellow and blue contour lines represent negative and positive absorption features, respectively. The intensity difference between neighboring contour lines is 10 %. Excitation pulses were centered at 1200 cm^{-1} with a FWHM of 165 cm^{-1}. Excess protons in water (a-d) are compared to Zundel cations in ACN (e-h), the latter described in detail in the previous chapter (see chapter 5).
The vibrational response of protons in water is very similar to Zundel cations in ACN. We observe the blue shifted excited state absorption, a direct manifestation of the double well potential of a proton hydrated in a Zundel type configuration. The negative and positive absorption features for detection frequencies below and above 1180 cm^{-1} are essentially parallel to the excitation frequency axis even for the earliest waiting time $T = 0$. It should be noted, that the observed intensity differences along the excitation frequency axis, such as the stronger absorption decrease at 1100 cm^{-1} in (a-c) have to be taken with care. The width of the mid-IR pulses used in the experiment only allows to sample a fraction of the

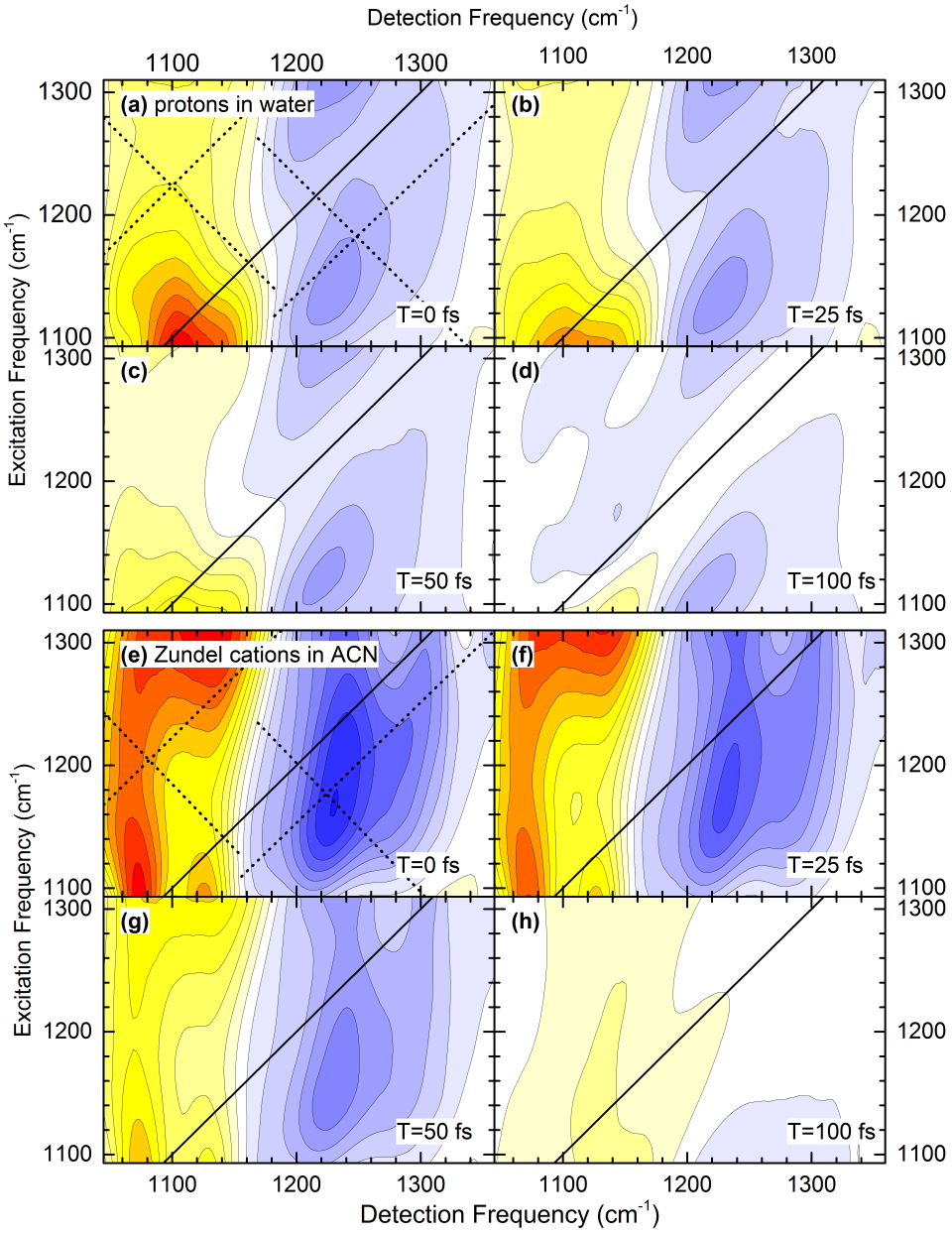

Figure 6.2: Absorptive 2D-IR spectra in the range of the proton transfer mode (z) with excitation centered around 1200 cm^{-1} for different waiting times T (0, 25, 50, 100 fs). Excitation frequency (ω_1) is plotted as a function of probe frequency (ω_3). Red to yellow and blue contour lines represent negative and positive absorbance changes, respectively. The intensity change between neighboring contour lines is 10 %.
(a)-(d) Excess protons in water. **(e)-(h)** Zundel cations selectively prepared in acetonitrile.

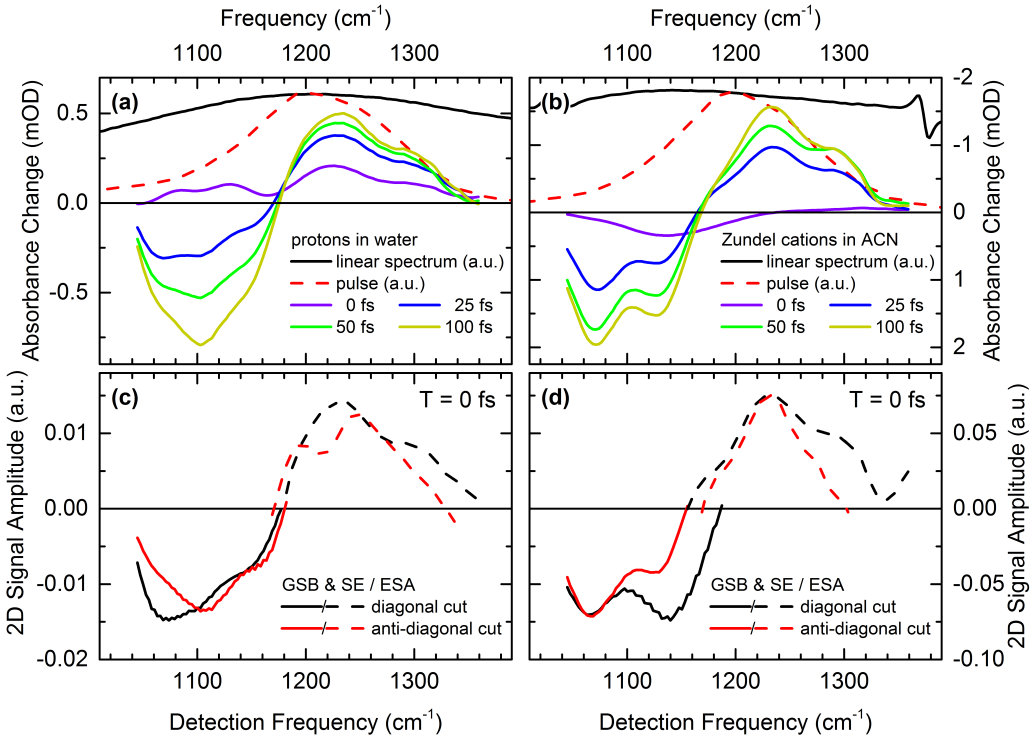

Figure 6.3: 2D-IR Signal integrated along the excitation frequency and plotted as a function of detection frequency for **(a)** excess protons in water and **(b)** Zundel cations selectively prepared in acetonitrile. The respective steady state absorption spectrum (black line) taken from Fig. 6.1b is shown together with the mid-IR pulse used in the experiment (red dashed line). Diagonal (black) and anti-diagonal cuts (red) taken along the signal of the GSB & SE (solid lines) and the ESA (dashed lines) in Fig. 6.2 for **(c)** excess protons in water and **(d)** Zundel cations selectively prepared in acetonitrile. The spectral cuts presented in this figure correspond to the dotted black lines in the respective ($T = 0$ fs) absorptive 2D-IR spectra in Fig 6.2a,e.

proton transfer fundamental around its maximum value (cf. Fig. 6.3a,b), thus overall intensity changes are limited due to the broad and homogeneous lineshape of z_{01}. Consequently, uncertainties in the phasing procedure of our 2D-IR spectra may lead to the observation of artificial "substructure" that would be way less pronounced if a larger bandwidth of z could be sampled and larger overall intensity differences would be measured (cf. Fig. 5.3 vs. Fig. 6.2e-h).

Fig. 6.3a,b displays the 2D-Signal integrated along the excitation frequency axis as a function of detection frequency. This representation is equivalent to transient pump-probe spectra obtained for delay times of 0, 25, 50 and 100 fs. When comparing protons in water to Zundel cations in ACN we observe a nearly identical behavior with the exception of the transient infrared spectrum at a delay time of 100 fs, that will be explained later. The integrated 2D-IR signal is a clear representation of the "artificial substructure", as we can directly compare it to the transient infrared spectra obtained with our two-color pump-probe setup (cf. Fig. 6.4), where the modulations on the signal are absent. The intensity modulations of our 2D-IR signals caused by the phasing procedure hamper the significance

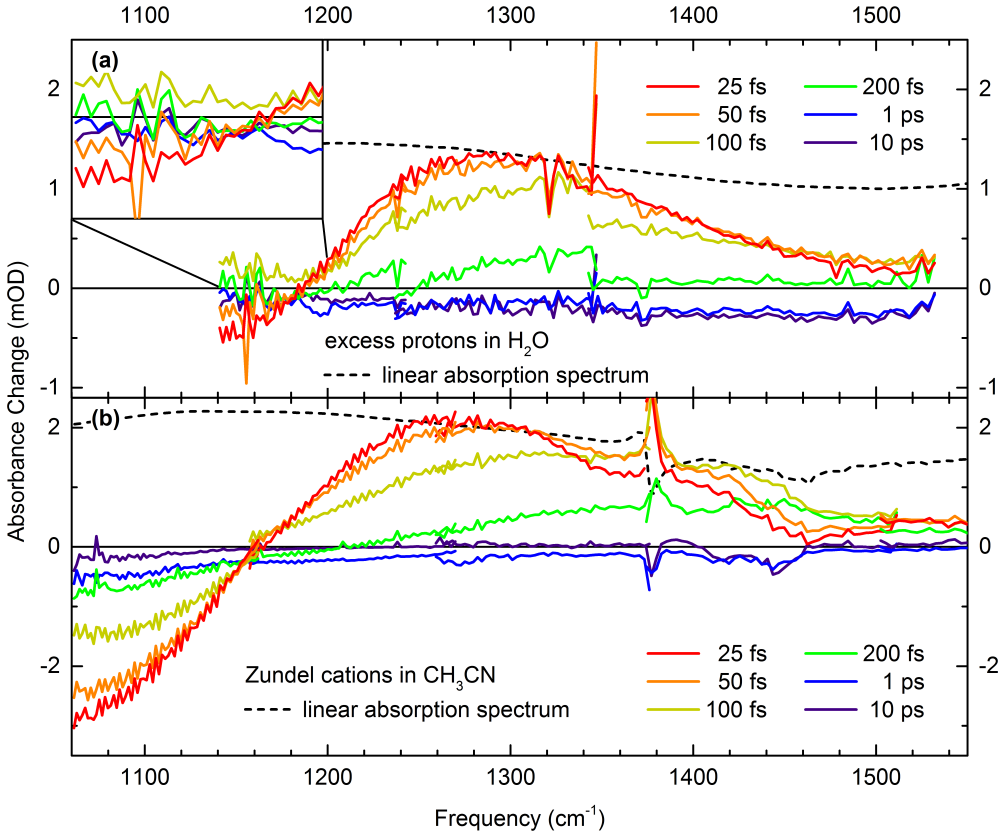

Figure 6.4: Transient infrared absorption spectra recorded in the range of the proton transfer mode z. The absorbance change ΔA is plotted as a function of probe frequency for fixed pump probe delay times in a range from 25 fs to 10 ps (solid lines). The scaled steady state absorption spectrum is shown as a dashed black line. **(a)** Excess protons in water. **(b)** Zundel cations selectively prepared in acetonitrile.

of the diagonal (black) and anti-diagonal (red) cuts presented in Fig. 6.3c,d.
In the author's view, discrepancies of the diagonal and anti-diagonal cuts for both protons in water Fig. 6.3c and Zundel cations in ACN Fig. 6.3d are artificial with the exception of frequencies above ∼1300 cm^{-1} for the cuts taken along the ESA. The slight inhomogeneity on the blue wing of the enhanced absorption feature is consistent throughout all of our 2D-IR data sets and needs further investigation.
In order to investigate the temporal evolution of the signal in the range of the proton transfer mode, we obtained two-color pump-probe spectra. Fig. 6.4 shows transient infrared absorption spectra measured with excitation centered at 1200 cm^{-1} for excess protons in water (a) and Zundel cations in acetonitrile (b). The spectral shape and to a large extent the temporal evolution of the transient spectra are nearly identical. Discrepancies occur only for frequencies below 1200 cm^{-1} and at delay times >1 ps. These can be explained by the vibrational response of the librational background of bulk water that is also excited by the pump pulse in (a). The inset in Fig. 6.4a magnifies the vibrational response for frequencies below 1200 cm^{-1}. We initially observe a negative absorbance change that transiently becomes positive before ending up in a long lived bleaching signal. We explain this behavior as follows.

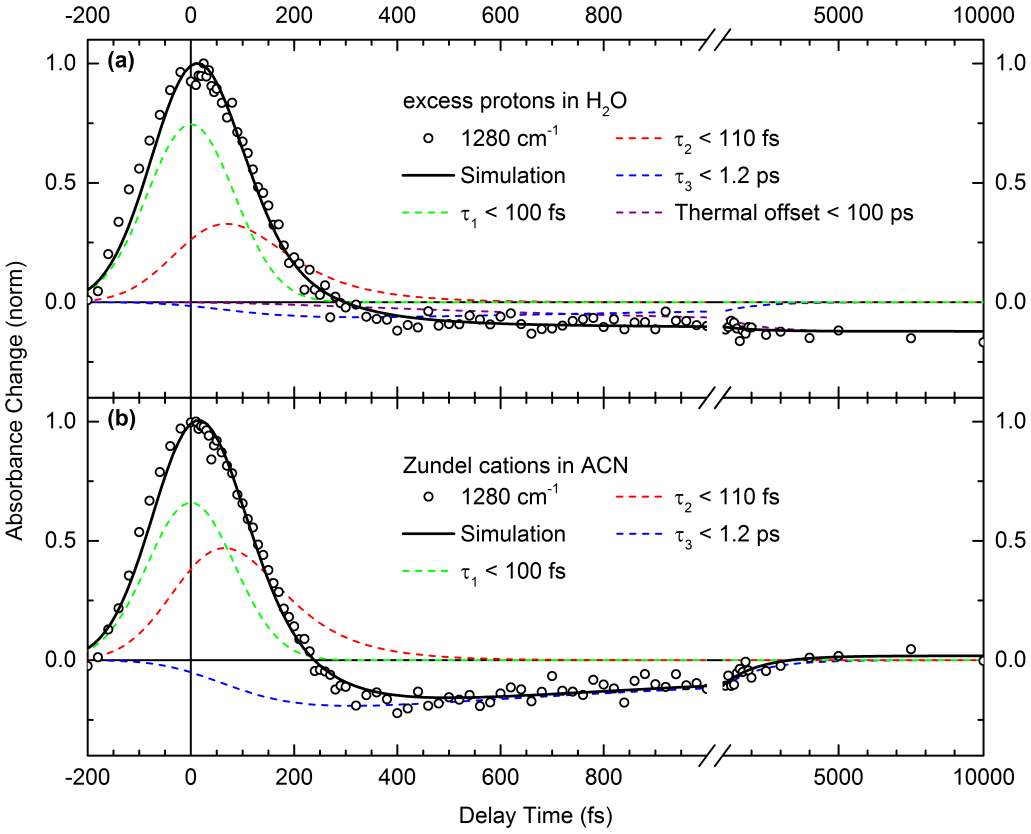

Figure 6.5: Time-resolved absorption changes ΔA at a fixed probe frequency of 1280 cm^{-1} (open circles). The experimental data is fit to a rate-equation model (black line) in order to retrieve the characteristic time constants τ_{1-3}. Dashed colored lines represent the deconvolution of the rate-equation model into contributing components. **(a)** Excess protons in water. **(b)** Zundel cations selectively prepared in acetonitrile.

The signal at the earliest delay times (<100 fs) is dominated by the ground state bleach and stimulated emission between the v = 0 and 1 state of the proton transfer mode z, leading to a negative absorption feature in the spectrum. As demonstrated by Ashihara et al. [52], bulk water exhibits a positive absorption signal in this frequency range due to the response of librational motions of bulk H_2O, that initially lead to a positive signal with maximum intensity for pump-probe delays of approximately 100 fs. Such signals compensate the negative absorption feature of z leading to a net positive signal at delay times around 100 fs. At pump-probe delays >3 ps, bulk water exhibits a long lived heating signal that manifests in a broad unstructured negative absorption change spanning the whole measured range, while the Zundel cations in ACN exhibit almost no absorbance change at delay times >3 ps.

Kinetic transients taken at the maximum of the excited state absorption signal (1280 cm^{-1}) are displayed in Fig. 6.5. At early times, excess protons in water (Fig.6.4a & Fig. 6.5a) exhibit a nearly identical behavior compared to Zundel cations predominantly prepared in ACN (Fig. 6.4b & Fig. 6.5b). Population relaxation occurs within the time resolution of the experiment (green dashed line in Fig. 6.5a) followed by energy redistribution processes (red dashed line) on a 110 fs time scale that lead to the formation of a locally hot ground

state. The energy transfer to the water environment, and thus the decay of the locally hot ground state occurs with a 1.2 ps time scale, comparable to the energy transfer from Zundel cations to the ACN environment in Fig. 6.5b. The long lived heating signal of the water background for protons in H_2O is accounted by an additional component (purple dashed line).

Concluding remarks

We observed striking similarities in our time-resolved experiments when comparing the vibrational response of excess protons in bulk water to Zundel cations predominantly prepared in acetonitrile. The unique character of the proton potential in a $H_5O_2^+$ moiety is at the heart of our analysis and allows to assign the observed vibrational responses of excess protons in water to Zundel type configurations. We embark on the same mechanisms to explain the observed 2D-IR and two-color pump-probe signals, as discussed in detail for $H_5O_2^+$ in ACN.
The low barrier proton potential in the $H_5O_2^+$ moiety is subject to strong modulations exerted by the water environment. Electrical fields along the direction of z are reported to range up to 60 MV/cm in bulk water at ambient conditions [162], twice as strong as in plain acetonitrile. Such electrical fields fluctuate with typical time scales of the water-network and the dominating contributions are sub-100 fs librational motions. These fluctuations translate into an ultrafast modulation of the proton position in the $H_5O_2^+$ moiety, resembled by asymmetries in the proton potential. This ultrafast modulation of the potential is connected with strong frequency excursions of intramolecular modes of $H_5O_2^+$ and manifests in the broad and nearly homogeneous lineshapes observed in the 2D-IR experiments (cf. Fig. 6.2a-d).
The present experiments do not qualify to make a statement about the abundance or importance of the Eigen cation as we specifically probe a Zundel marker mode. However, the full recovery of the signal associated with Zundel cations in water (cf. dashed blue line in Fig. 6.5a) suggests that the Zundel geometry is preserved for a minimum lifetime on the order of a picosecond − the average lifetime of a hydrogen bond in bulk water.
In conclusion, our experimental results strongly suggest that the Zundel cation is a substantial hydration species of excess protons in water and thus plays an important role in the resting period between proton transfer steps. This statement is supported by recent 2D-IR experiments in the OH bending and stretching range of protons in water by Thämer et al., invoking an important role of the Zundel cation and a minimum lifetime of such hydration species of 470 fs [29]. Consequently, our results rule out pictures of proton transport in water, that are based on the Eigen cation as the sole meta-stable structure and the Zundel cation occurring as a fleeting transition state which persists only for very short times [20].

The controversial discussion of Eigen and Zundel type hydration species in interpretations of proton transport in water is partly induced by dissimilar definitions of the involved hydration species such as the commonly used asymmetry parameter z, that formally equals the proton transfer vibration [23, 164–167][1].
Fig. 6.6 illustrates the concept of z. Here, the excess proton position is evaluated as a function of the O$\cdots$H distance to the two closest neighboring water molecules. The difference value $z = r_1 - r_2$ determines the classification in either Zundel or Eigen type complexes.

[1] The asymmetry parameter is usually referred to as δ in the literature and must not be confused with the OH bending vibration δ.

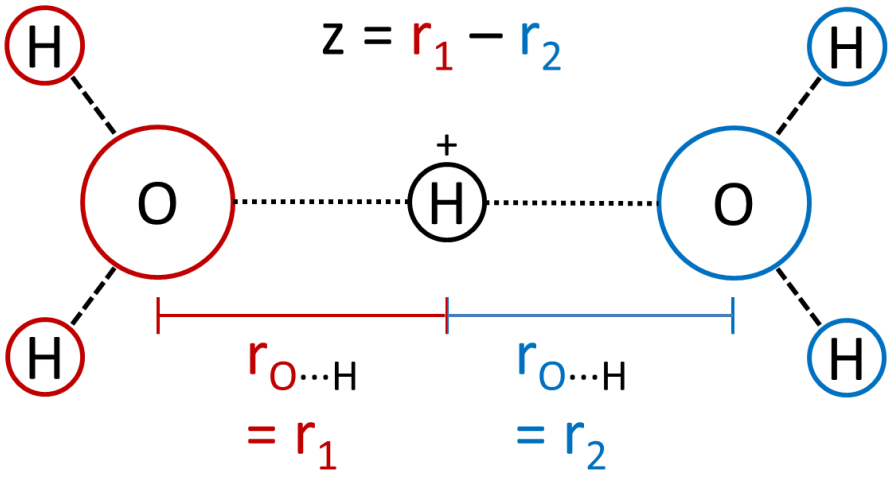

Figure 6.6: Schematic illustration of the asymmetry parameter z. It is defined as the difference value of the excess proton distance in relation to the oxygen atoms of its nearest two neighboring water molecules $z = r_1 - r_2$. Eigen and Zundel hydration geometries are discriminated by different z values.

With the results of the current work, this definition is meaningless. Sub-100 fs field fluctuations of the water environment modulate the proton position on an ultrafast time scale, sampling the major part of the O···O distance in a Zundel complex. As a result, z covers a large range within the existing Zundel geometry and cannot be used to distinguish Zundel and Eigen species.
The O···O distance R is a more suitable parameter to define Eigen and Zundel geometries. Our calculations have shown, that the character of the proton potential critically depends on R (cf. Fig. 5.6b on page 74). The central barrier of the potential is lower than the zero point energy of the proton transfer mode for $R \leq 2.5$ Å and the proton wavefunction is delocalized in the field free case. Typical field fluctuations $E_z \leq 30$ MV/cm distort the proton potential, however the low barrier double well character is retained and the proton does not localize in the form of an H_3O^+. For O···O distances larger than 2.5 Å, the central barrier of the proton potential becomes energetically comparable to, or larger than the zero point energy of z. Consequently, the proton potential gains an anharmonic character allowing the proton to localize in the form of H_3O^+ even in the field free case. In our view, such configurations are defined as Eigen type hydration species.
The outlined concept may be subject to improvements in the future, but gives a suitable definition of Eigen and Zundel species with respect to vibrational spectroscopy, considering realistic time scales of the excess proton's dynamics in solution.
Problems arise in a range, where the central barrier is energetically higher than the v = 0 state but lower than the v = 1 state of the proton potential. This scenario occurs for O···O distances in the range of approximately 2.5-2.6 Å. Here, one would still observe a blue shifted excited state absorption in time-resolved mid-IR experiments in the range of the proton transfer mode z, as the energy difference ΔE for the v = 1 to 2 transition remains larger than for the v = 0 to 1 transition. However, the proton can localize in the form of H_3O^+ as the central barrier exceeds the v = 0 state at least transiently for strongly

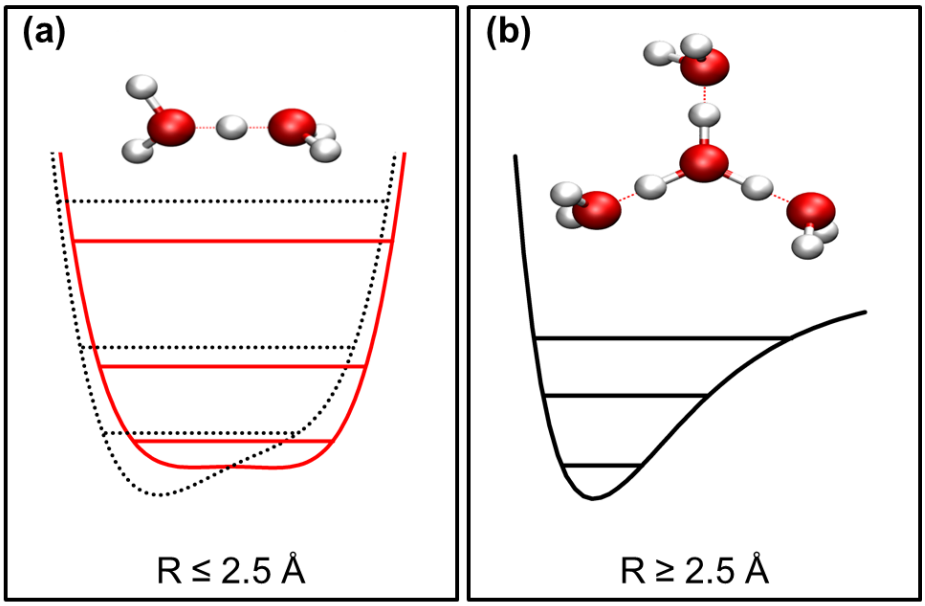

Figure 6.7: Schematic illustration of the double minimum potential associated with a Zundel type configuration **(a)** and the anharmonic potential associated with an Eigen type configuration **(b)**.

distorted potentials. This behavior results in a complex that is neither fully described by our definitions of Eigen and Zundel cations.

Our results obtained from time-resolved 2D-IR experiments, two-color pump-probe experiments and theoretical simulations suggest that the time scales associated with the proton transfer vibration are clearly separated from actual proton transfer events. The population of the v = 1 state of the proton transfer mode after resonant vibrational excitation decays with a 20-40 fs time constant leading to the formation of a locally hot ground state of the excited molecule within ∼100 fs. Furthermore, the proton position in $H_5O_2^+$ is strongly modulated by external field fluctuations with typical time scales of the fluctuating environment. For both solvents, H_2O and ACN, the dominant contributions of structural fluctuations are in the sub-100 fs range [31, 162]. In contrast, proton transfer events in water occur on a ∼1.5 ps time scale [6]. As an important consequence, vibrational excitation of the proton transfer mode, contrary to its name, does not relate to the proton hopping itself. Other mechanisms must be essential that trigger the transfer of the proton to a neighboring water molecule, such as larger structural reorientations of water molecules in the vicinity of the Zundel cation.

7 Conclusions

The aim of this thesis, to give new insight into the local environment of the hydrated excess proton in the resting period in between successive proton transfer events, was realized by the selective preparation of Zundel-type hydration species in an acetonitrile environment. Vibrational dynamics and spectral signatures were studied by ultrafast nonlinear vibrational spectroscopy in close conjunction with theoretical simulations. The experimental identification and characterization of the Zundel marker mode O$\cdots$H$\cdots$O (z), which is the shuttling motion of the shared proton between the flanking oxygen atoms in the $H_5O_2^+$ moiety, allowed for a one to one comparison to protons in water. The results obtained from time-resolved 2D-IR and two-color pump-probe experiments strongly suggest Zundel type configurations as a major hydration species of excess protons in water. The lifetime of such complexes exceeds one picosecond, the average lifetime of the hydrogen bond in bulk water. In the following, the main results are summarized:

H_2O monomers in acetonitrile

To benchmark the results obtained for Zundel cations in ACN, we investigated water monomers before addition of excess protons. Results obtained from two-color pump-probe experiments on water monomers diluted in acetonitrile revealed vibrational lifetimes of the v = 1 state of the OH stretching and bending vibration of 6.4 $\pm$ 1 ps and 4 $\pm$ 0.5 ps, respectively. Population of the symmetric and asymmetric OH stretching vibrations decays via the OH bending overtone, the OH bending fundamental as well as the librational motion of the excited water molecule around its x-axis. In this context, the anharmonic coupling of the OH stretching and bending vibrations was observed directly in our two-color pump-probe transients. A rate-equation analysis of the data suggests a dissimilar faster decay rate for the OH bending overtone compared to the OH bending and stretching fundamental transitions, resulting in negligibly small transient populations of the v = 2 state of the OH bending oscillator.

Zundel cations in acetonitrile

The addition of excess protons to water monomers in ACN has a dramatic effect even on the steady state absorption spectrum. We relied on the predominant preparation of Zundel cations in acetonitrile to obtain species dependent data. Ultrafast 2D-IR and two-color pump-probe experiments allowed for a separation of OH stretching and bending vibrations from the proton motion and continuum absorption by their different vibrational character. In conjunction with theory, a picture of proton hydration in a $H_5O_2^+$ moiety was developed, that explains the continuous absorption in the mid-infrared region, a hallmark of Zundel cations in the condensed phase.

- 2D-IR experiments in the range of the proton transfer mode z revealed, for the first time, the double minimum character of the proton potential in a Zundel cation by observing a blue-shifted v = 1 to 2 absorption band. This potential is modulated on the femtosecond time scale by electric field fluctuations imposed on z by structural fluctuations of the polar acetonitrile environment, manifesting in broad and homogeneous lineshapes in the absorptive 2D-IR spectra.

- Theoretical calculations of the proton potential showed, that the vibrational ground state v = 0 of the proton transfer mode lies clearly above the central barrier. Consequently, the proton can move barrierless in between the flanking oxygen atoms. For typical field strengths $E_z \leq 30$ MV/cm that ACN exerts along the direction of z, the potential becomes clearly asymmetric while retaining the low-barrier double minimum well character.

- Modulations of the proton potential by external field fluctuations are linked to strong frequency excursions of associated transitions, that are the fundamental transition of the proton transfer mode z_{01}, its overtone transition z_{02} and a combination tone with the O$\cdots$O mode R. Additionally, stochastic thermal excitation of R lead to a change in the O$\cdots$O distance of approximately 0.1 Å, deforming the proton potential and adding to the line broadening of the transitions mentioned above. In combination with anharmonic couplings between the proton transfer mode and the O$\cdots$O mode, these two mechanisms explain the observed absorption continuum of Zundel cations in acetonitrile.

- The vibrational lifetime of the v = 1 state of the proton transfer mode is estimated in a range from 20 to 40 fs, close to the intrinsic oscillation period of ∼30 fs.

- Two-color pump-probe experiments helped to discern OH stretching and bending vibrations from the absorption continuum by their different vibrational character. Vibrational lifetimes were found to be less than 50 fs for the OH stretching and less than 60 fs for the OH bending vibration, 4 times shorter than in bulk liquid water and 2 orders of magnitude shorter than for water monomers in acetonitrile.

- Population relaxation of the OH stretching, OH bending and the proton transfer vibration leads to a sub-picosecond formation of a locally hot ground state, where the energy is redistributed within the excited Zundel molecule and "dumped" into low frequency modes. Subsequent energy transfer from the excited molecule to the acetonitrile environment occurs on a 1-2 ps time scale.

Excess protons in water

- The vibrational signature of the proton transfer mode persists to a large extent (∼80 %) in the steady state absorption spectrum transitioning from Zundel cations in ACN to excess protons in water. However, the maximum of the absorption band shifts by about 40 cm^{-1} to higher frequencies, consistent with the stronger electrical fields E_z (up to 60 MV/cm) that water exerts on the shared proton.

- 2D-IR and two-color pump-probe experiments in the range of the proton transfer mode display a vibrational response very similar compared to Zundel cations in ACN. These are, the blue shifted ESA, the broad and homogeneous lineshapes and very similar

vibrational relaxation dynamics. The striking similarities invoke a similar mechanisms of proton hydration for the excess proton in water and the Zundel cation in ACN.

The Zundel cation in water and acetonitrile is not a static structure but a highly fluctuating complex. The proton samples a large range of the O$\cdots$O distance between the flanking water molecules within 1 ps. The ultrafast proton rattling is mediated by the fluctuating electrical forces exerted by the polar environment. Whilst approaching one of the flanking oxygen atoms temporarily, the proton does not localize in the form of H_3O^+ for the average O$\cdots$O distance $R \leq 2.5$ Å. Such proton dynamics are on a much shorter time scale (fs) than the lifetime of the Zundel complex in water (ps).
A similar protocol should be applied using marker modes of the Eigen cation, e.g., the umbrella mode in order to investigate the importance of such hydration species in bulk water, work that is currently in progress. Eventually, this could help to resolve the controversial discussion on the relative abundance and stability of Eigen and Zundel cations in water.

8 Zusammenfassung

Das Ziel dieser Dissertation, neue Einsicht in die lokale Umgebung hydratisierter Überschussprotonen welche in Ruhephasen zwischen erfolgreichen Protontransfereignissen vorliegen, wurde durch die selektive Präparation einer Zundel-artigen Hydratisierungsspezies in einer Acetonitrilumgebung realisiert. Schwingungsdynamiken und spektrale Signaturen wurden mittels ultraschneller nichtlinearer Spektroskopie und in enger Zusammenarbeit mit theoretischen Simulationen studiert. Die experimentelle Identifikation und Charakterisierung der Zundelmarkermode O···H···O (z), welche die Hin- und Herbewegung des geteilten Protons zwischen den flankierenden Sauerstoffatomen in der $H_5O_2^+$-Gruppierung darstellt, erlaubte einen eins zu eins Vergleich zu Protonen in Wasser. Die Ergebnisse von zeitaufgelösten 2D-IR und Zweifarben-Anrege-Abtastexperimenten legen Zundel-artige Konfigurationen als eine dominante Hydratisierungsspezies von Protonen in Wasser nahe. Solche Komplexe weisen eine Lebensdauer von mehr als einer Pikosekunde auf, die mittlere Lebensdauer einer Wasserstoffbrückenbindung in Wasser. Im Folgenden sind die Hauptergebnisse zusammengefasst:

H_2O Monomere in Acetonitril

Um die Ergebnisse für Zundel-Kationen in ACN zu bewerten, wurden Wassermonomere vor der Zugabe von Protonen untersucht. Ergebnisse von Zweifarben-Anrege-Abtastexperimenten an Wassermonomeren verdünnt in Acetonitril haben Schwingungslebensdauern des v = 1 Zustandes der OH Streck- und Biegeschwingung von 6.4 ± 1 ps und 4 ± 0.5 ps enthüllt. Populationen der symmetrischen und asymmetrischen OH Streckschwingungen zerfallen mittels des OH Biegeobertons, der OH Biegefundamentalschwingung, sowie der Librationsbewegung des angeregten Wassermoleküls um seine x-Achse. In diesem Zusammenhang wurde die anharmonische Kopplung der OH Streck- und Biegebewegungen direkt in unseren Zweifarben-Anrege-Abtasttransienten beobachtet. Eine Analyse der Daten mit einem Ratengleichungsmodell suggeriert eine ungleich schnellere Zerfallsrate für den OH Biegeoberton im Vergleich zur OH Biege- und Streckfundamentalschwingung, was zu einer vernachlässigbar kleinen Übergangspopulation des v = 2 Zustandes des OH Biegeoszillators führt.

Zundel-Kationen in Acetonitril

Die Zugabe von Überschussprotonen zu Wassermonomeren in ACN hat einen dramatischen Effekt, sogar auf das stationäre Absorptionsspektrum. Wir haben uns auf die vorwiegende Präparation von Zundel-Kationen in Acetonitril berufen um speziesspezifische Daten zu erhalten. Ultraschnelle 2D-IR und Zweifarben-Anrege-Abtastexperimente erlauben eine Separierung der OH Streck- und Biegeschwingungen von der Protonbewegung und dem

Absorptionskontinuum anhand ihres unterschiedlichen Schwingungscharakters. In Zusammenarbeit mit Theorie wurde ein Bild der Protonhydratisierung in einer $H_5O_2^+$-Gruppierung entwickelt, das die kontinuierliche Absorption im mittleren Infrarotbereich erklärt, ein Kennzeichen von Zundel-Kationen in der kondensierten Phase.

- 2D-IR Experimente im Bereich der Protontransferschwingung z haben zum ersten mal den Doppelminimumcharakter des Protonpotentials in Zundel-Kationen durch die Beobachtung einer blau verschobenen v = 1 nach 2 Absorptionsbande enthüllt. Dieses Potential wird auf der Femtosekundenzeitskala durch elektrische Feldfluktuationen moduliert, welche durch die strukturellen Fluktuationen der polaren Acetonitrilumgebung auf z ausgeübt werden und sich in den breiten und homogenen Linienformen der 2D-IR Spektren offenbaren.

- Theoretische Berechnungen des Protonpotentials zeigten, dass der Schwingungsgrundzustand v = 0 der Protontransfermode deutlich über der zentralen Barriere liegt. Infolgedessen kann sich das Proton barrierefrei zwischen den flankierenden Sauerstoffatomen bewegen. Für typische Feldstärken $E_z \leq 30$ MV/cm, welche ACN entlang der Richtung von z ausübt, wird das Potential deutlich asymmetrisch, wobei es seinen Doppelminimumcharakter mit einer niedrigen Barriere beibehält.

- Modulationen des Protonpotentials durch externe Feldfluktuationen sind mit starken Frequenzverschiebungen von zugehörigen Übergängen verknüpft. Diese sind der Fundamentalübergang der Protontransfermode z_{01}, ihr Oberton z_{02} und ein Kombinationston mit der O···O Mode R. Zusätzlich führen stochastische thermische Anregungen von R zu einer Änderung des O···O Abstandes um ungefähr 0.1 Å, was das Protonpotential verformt und zur Linienverbreiterung der zuvor genannten Übergänge beiträgt. In Kombination mit anharmonischen Kopplungen zwischen der Protontransfermode und der O···O Mode erklären diese beiden Mechanismen die beobachtete kontinuierliche Absorption von Zundel-Kationen in Acetonitril.

- Die Schwingungslebensdauer des v = 1 Zustandes der Protontransfermode wird im Bereich von 20 bis 40 fs abgeschätzt, nahe der intrinsischen Schwingungsperiode von ∼30 fs.

- Zweifarben-Anrege-Abtastexperimente haben dabei geholfen die OH Streck- und Biegeschwingung anhand ihres unterschiedlichen Schwingungscharakters vom Absortpionskontinuum zu unterscheiden. Es wurden Schwingungslebensdauern von weniger als 50 fs für die OH Streckschwingung und weniger als 60 fs für die OH Biegeschwingung gefunden, 4 mal kürzer als in flüssigem Wasser und um 2 Größenordnungen kürzer als in Acetonitril gelösten Wassermonomeren.

- Populationszerfall der OH Streck-, OH Biege- und Protontransferschwingung führt zu einer Ausbildung eines lokalen heißen Grundzustandes auf der sub-Pikosekunden Zeitskala, in welchem die Energie im angeregten Zundel-Molekül umverteilt und in niederfrequenten Moden „deponiert" wird. Anschließender Energietransfer vom angeregten Molekül an die Acetonitrilumgebung findet auf einer 1-2 ps Zeitskala statt.

Überschussprotonen in Wasser

- Bei einem Übergang von ACN nach H_2O bleiben die Schwingungssignaturen der Protontransfermode zu einem großen Teil (∼80 %) im stationären Absorptionsspek-

trum bestehen. Indes verschiebt das Maximum der Absorptionsbande um 40 cm^{-1} zu höheren Frequenzen, konsistent mit den stärkeren Feldern E_z (bis zu 60 MV/cm) die Wasser auf das geteilte Proton ausübt.

- 2D-IR und Zweifarben-Anrege-Abtastexperimente im Bereich der Protontransfermode zeigen eine nahezu nicht unterscheidbare Schwingungsantwort zu der von Zundel-Kationen in ACN. Diese sind die blau verschobene ESA, die breiten und homogenen Linienformen und ähnliche Schwingungsrelaxationsdynamiken. Die bemerkenswerten Gemeinsamkeiten weisen auf einen vergleichbaren Mechanismus der Protonhydratisierung von Überschussprotonen in Wasser und Zundel-Kationen in ACN hin.

Das Zundel-Kation in Wasser und Acetonitril ist keine statische Struktur aber ein stark fluktuierender Komplex. Das Proton durchschreitet einen großen Bereich des O$\cdots$O Abstandes zwischen den flankierenden Wassermolekülen binnen 1 ps. Die ultraschnelle Proton-Schüttelbewegung wird durch fluktuierende elektrische Kräfte der polaren Umgebung vermittelt. Während sich das Proton temporär einem der flankierenden Sauerstoffatome annähert, lokalisiert es nicht in der Form des H_3O^+. Insbesondere für mittlere O$\cdots$O Abständ $R \leq 2.5$ Å sind die fluktuierenden Komplexe als Zundel-Kationen in Lösung charakterisiert. Solche Protondynamiken finden auf einer viel kürzeren Zeitskala (fs) statt als die Lebensdauer des Zundel-Komplexes in Wasser (ps).
Ein ähnliches Protokoll sollte unter Verwendung von Markermoden des Eigen-Kations angewandt werden, um z.B. anhand der ,,UmbrellaMode die Bedeutung solcher Hydratisierungsspezies in Wasser zu untersuchen. Solche Untesuchungen finden gegenwärtig statt. Letztlich könnte dies die kontroverse Diskussion um die relative Menge und Stabilität von Eigen- und Zundel-Kationen in Wasser aufklären.

Publications

Peer Reviewed Articles

Related to this work:

- F. Dahms, R. Costard, E. T. J. Nibbering, and T. Elsaesser, "Ultrafast Vibrational Energy Flow in Water Monomers," *Chemical Physics Letters*, vol. 652, pp. 50-55, 2016
- F. Dahms, R. Costard, E. Pines, B. P. Fingerhut, E. T. J. Nibbering, and T. Elsaesser, "The Hydrated Excess Proton in the Zundel Cation $H_5O_2^+$: The Role of Ultrafast Solvent Fluctuations," *Angewandte Chemie International Edition*, vol. 55, pp. 10600-10605, 2016
- F. Dahms, B. P. Fingerhut, E. T. J. Nibbering, E. Pines, and T. Elsaesser, "Large Amplitude Transfer Motion of Hydrated Excess Protons Mapped by Ultrafast 2D IR Spectroscopy," *Science*, vol. 357, pp. 491-495, 2017

Other:

- B. Schäfer, T. Bauer, I. Faus, J. A. Wolny, F. Dahms, O. Fuhr, S. Lebedkin, H.-C. Wille, K. Schlage, K. Chevalier, F. Rupp, R. Diller, V. Schünemann, M. M. Kappes, and M. Ruben, "A Luminescent Pt_2Fe Spin Crossover Complex," *Dalton Transactions*, vol. 46, pp. 2289-2302, 2017

Conference Proceedings

Related to this work:

- F. Dahms, R. Costard, B. P. Fingerhut, E. Pines, E. T. J. Nibbering, and T. Elsaesser, "The Hydrated Excess Proton – Ultrafast Vibrational Dynamics of the Zundel Cation $H_5O_2^+$," *Ultrafast Phenomena XX*, 2016

Bibliography

[1] R. Stewart, *The Proton: Applications to Organic Chemistry*. Academic Press, first ed., 1985.

[2] R. P. Bell, *The Proton in Chemistry*. Springer, Boston MA, 1973.

[3] A. A. Noyes and Y. Kato, "The Equivalent Conductance of Hydrogen-Ion Derived from Transference Experiments with Nitric Acid," *Journal of the American Chemical Society*, vol. 30, pp. 318–334, 1908.

[4] A. A. Noyes, A. Melcher, H. Cooper, G. Eastman, and Y. Kato, "The Conductivity and Ionization of Salts, Acids, and Bases in Aqueous Solutions at High Temperatures," *Journal of the American Chemical Society*, vol. 30, pp. 335–353, 1908.

[5] J. Johnston, "The Change of the Equivalent Conductance of Ions with the Temperature," *Journal of the American Chemical Society*, vol. 31, pp. 1010–1020, 1909.

[6] S. Meiboom, "Nuclear Magnetic Resonance Study of the Proton Transfer in Water," *The Journal of Chemical Physics*, vol. 34, pp. 375–388, 1961.

[7] M. Eigen and L. De Maeyer, "Self-Dissociation and Protonic Charge Transport in Water and Ice," *Proceedings of the Royal Society of London. Series A, Mathematical and Physical Sciences*, pp. 505–533, 1958.

[8] M. Eigen, "Proton Transfer, Acid-Base Catalysis, and Enzymatic Hydrolysis. Part I: Elementary Processes," *Angewandte Chemie International Edition*, vol. 3, pp. 1–19, 1964.

[9] L. Onsager, "The Motion of Ions: Principles and Concepts," *Science*, vol. 166, p. 1359–1364, 1969.

[10] P. Atkins and J. de Paula, *Atkins' Physical Chemistry*. Oxford University Press, tenth ed., 2014.

[11] B. Roux, "Computational Studies of the Gramicidin Channel," *Accounts of Chemical Research*, vol. 35, pp. 366–375, 2002.

[12] T. E. Decoursey, "Voltage-Gated Proton Channels and Other Proton Transfer Pathways," *Physiological Reviews*, vol. 83, pp. 475–579, 2003.

[13] S. Cukierman, "Et tu, Grotthuss! And Other Unfinished Stories," *Biochimica et Biophysica Acta (BBA)-Bioenergetics*, vol. 1757, pp. 876–885, 2006.

[14] C. A. Wraight, "Chance and Design—Proton Transfer in Water, Channels and Bioenergetic Proteins," *Biochimica et Biophysica Acta (BBA) - Bioenergetics*, vol. 1757, pp. 886 – 912, 2006.

[15] K.-D. Kreuer, "Proton Conductivity: Materials and Applications," *Chemistry of Materials*, vol. 8, pp. 610–641, 1996.

[16] K.-D. Kreuer, S. J. Paddison, E. Spohr, and M. Schuster, "Transport in Proton Conductors for Fuel-Cell Applications: Simulations, Elementary Reactions, and Phenomenology," *Chemical Reviews*, vol. 104, pp. 4637–4678, 2004.

[17] E. Wicke, M. Eigen, and T. Ackermann, "Über den Zustand des Protons (Hydroniumions) in Wässriger Lösung," *Zeitschrift für Physikalische Chemie*, vol. 1, pp. 340–364, 1954.

[18] G. Zundel and H. Metzger, "Energiebänder der Tunnelnden Überschuß-Protonen in Flüssigen Säuren. Eine IR-Spektroskopische Untersuchung der Natur der Gruppierungen $H_5O_2^+$," *Zeitschrift für Physikalische Chemie*, vol. 58, pp. 225–245, 1968.

[19] M. L. Huggins, "Hydrogen Bridges in Ice and Liquid Water," *The Journal of Physical Chemistry*, vol. 40, pp. 723–731, 1936.

[20] N. Agmon, H. J. Bakker, R. K. Campen, R. H. Henchman, P. Pohl, S. Roke, M. Thämer, and A. Hassanali, "Protons and Hydroxide Ions in Aqueous Systems," *Chemical Reviews*, vol. 116, pp. 7642–7672, 2016.

[21] D. Marx, "Proton Transfer 200 Years After von Grotthuss: Insights From Ab Initio Simulations," *ChemPhysChem*, vol. 7, pp. 1848–1870, 2006.

[22] D. Marx, A. Chandra, and M. E. Tuckerman, "Aqueous Basic Solutions: Hydroxide Solvation, Structural Diffusion, and Comparison to the Hydrated Proton," *Chemical Reviews*, vol. 110, pp. 2174–2216, 2010.

[23] D. Marx, M. E. Tuckerman, J. Hutter, and M. Parrinello, "The Nature of the Hydrated Excess Proton in Water," *Nature*, vol. 397, pp. 601–604, 1999.

[24] J. A. Napoli, O. Marsalek, and T. E. Markland, "Decoding the Spectroscopic Features and Timescales of Aqueous Proton Defects," *arXiv preprint arXiv:1709.05740*, 2017.

[25] Y. Wu, H. Chen, F. Wang, F. Paesani, and G. A. Voth, "An Improved Multistate Empirical Valence Bond Model for Aqueous Proton Solvation and Transport," *The Journal of Physical Chemistry B*, vol. 112, pp. 467–482, 2008.

[26] E. T. J. Nibbering and T. Elsaesser, "Ultrafast Vibrational Dynamics of Hydrogen Bonds in the Condensed Phase," *Chemical Reviews*, vol. 104, pp. 1887–1914, 2004. PMID: 15080715.

[27] J. M. Headrick, E. G. Diken, R. S. Walters, N. I. Hammer, R. A. Christie, J. Cui, E. M. Myshakin, M. A. Duncan, M. A. Johnson, and K. D. Jordan, "Spectral Signatures of Hydrated Proton Vibrations in Water Clusters," *Science*, vol. 308, pp. 1765–1769, 2005.

[28] W. Kulig and N. Agmon, "A 'Clusters-in-Liquid' Method for Calculating Infrared Spectra Identifies the Proton-Transfer Mode in Acidic Aqueous Solutions," *Nature Chemistry*, vol. 5, pp. 29–35, 2013.

[29] M. Thämer, L. De Marco, K. Ramasesha, A. Mandal, and A. Tokmakoff, "Ultrafast 2D IR Spectroscopy of the Excess Proton in Liquid Water," *Science*, vol. 350, pp. 78–82, 2015.

[30] N. B.-M. Kalish, E. Shandalov, V. Kharlanov, D. Pines, and E. Pines, "Apparent Stoichiometry of Water in Proton Hydration and Proton Dehydration Reactions in CH_3CN/H_2O Solutions," *The Journal of Physical Chemistry A*, vol. 115, pp. 4063–4075, 2011.

[31] J. Ruthmann, S. Kovalenko, N. Ernsting, and D. Ouw, "Femtosecond Relaxation of 2-Amino-7-Nitrofluorene in Acetonitrile: Observation of the Oscillatory Contribution to the Solvent Response," *The Journal of Chemical Physics*, vol. 109, pp. 5466–5468, 1998.

[32] P. Ädelroth and P. Brzezinski, "Surface-Mediated Proton-Transfer Reactions in Membrane-Bound Proteins," *Biochimica et Biophysica Acta (BBA)-Bioenergetics*, vol. 1655, pp. 102–115, 2004.

[33] F. M. Menger, "Enzyme Reactivity from an Organic Perspective," *Accounts of Chemical Research*, vol. 26, pp. 206–212, 1993.

[34] A. Novak, "Hydrogen Bonding in Solids. Correlation of Spectroscopic and Crystallographic Data.," in *Large Molecules*, pp. 177–216, Springer, 1974.

[35] E. Libowitzky, "Correlation of O−H Stretching Frequencies and O−H···O Hydrogen Bond Lengths in Minerals," *Monatshefte für Chemie/Chemical Monthly*, vol. 130, pp. 1047–1059, 1999.

[36] G. A. Jeffrey and G. A. Jeffrey, *An Introduction to Hydrogen Bonding*, vol. 32. Oxford University Press New York, 1997.

[37] T. Steiner, "The Hydrogen Bond in the Solid State," *Angewandte Chemie International Edition*, vol. 41, pp. 48–76, 2002.

[38] H. M. Chadwell, "The Molecular Structure of Water," *Chemical Reviews*, vol. 4, pp. 375–398, 1928.

[39] D. Ives and T. Lemon, "Structure and Properties of Water," *Royal Institute of Chemistry, Reviews*, vol. 1, pp. 62–105, 1968.

[40] F. Franks, ed., *Water: A Comprehensive Treatise*. Plenum Press, 1975.

[41] F. Franks, *Water: A Matrix of Life*. Royal Society of Chemistry, 2007.

[42] F. H. Allen, O. Kennard, D. G. Watson, L. Brammer, A. G. Orpen, and R. Taylor, "Tables of Bond Lengths Determined by X-Ray and Neutron Diffraction. Part 1. Bond Lengths in Organic Compounds," *Journal of the Chemical Society, Perkin Transactions 2*, pp. S1–S19, 1987.

[43] R. Rey, K. B. Møller, and J. T. Hynes, "Ultrafast Vibrational Population Dynamics of Water and Related Systems: A Theoretical Perspective," *Chemical Reviews*, vol. 104, pp. 1915–1928, 2004.

[44] H. J. Bakker and J. L. Skinner, "Vibrational Spectroscopy as a Probe of Structure and Dynamics in Liquid Water," *Chemical Reviews*, vol. 110, pp. 1498–1517, 2010.

[45] D. Laage, G. Stirnemann, F. Sterpone, R. Rey, and J. T. Hynes, "Reorientation and Allied Dynamics in Water and Aqueous Solutions," *Annual Review of Physical Chemistry*, vol. 62, pp. 395–416, 2011.

[46] S. Ashihara, N. Huse, A. Espagne, E. Nibbering, and T. Elsaesser, "Vibrational Couplings and Ultrafast Relaxation of the O–H Bending Mode in Liquid H_2O," *Chemical Physics Letters*, vol. 424, pp. 66–70, 2006.

[47] A. B. McCoy, "The Role of Electrical Anharmonicity in the Association Band in the Water Spectrum," *The Journal of Physical Chemistry B*, vol. 118, pp. 8286–8294, 2014.

[48] Y. Maréchal, "Infrared Spectra of Water. I. Effect of Temperature and of H/D Isotopic Dilution," *The Journal of Chemical Physics*, vol. 95, pp. 5565–5573, 1991.

[49] Y. Maréchal, "Infrared Spectra of Water. II: Dynamics of H2O (D2O) Molecules," *Journal de Physique II*, vol. 3, pp. 557–571, 1993.

[50] A. V. Khakhalin and A. V. Koroleva, "Investigation of the Temperature Dependence for the Spectra of Supercooled Water in the Middle Infrared," *Moscow University Physics Bulletin*, vol. 69, pp. 66–71, 2014.

[51] S. Giuffrida, G. Cottone, and L. Cordone, "The Water Association Band as a Marker of Hydrogen Bonds in Trehalose Amorphous Matrices," *Physical Chemistry Chemical Physics*, vol. 19, pp. 4251–4265, 2017.

[52] S. Ashihara, N. Huse, A. Espagne, E. T. J. Nibbering, and T. Elsaesser, "Ultrafast Structural Dynamics of Water Induced by Dissipation of Vibrational Energy," *The Journal of Physical Chemistry A*, vol. 111, pp. 743–746, 2007.

[53] M. Cowan, B. D. Bruner, N. Huse, J. Dwyer, B. Chugh, E. Nibbering, T. Elsaesser, and R. Miller, "Ultrafast Memory Loss and Energy Redistribution in the Hydrogen Bond Network of Liquid H_2O," *Nature*, vol. 434, pp. 199–202, 2005.

[54] T. Elsaesser and H. J. Bakker, *Ultrafast Hydrogen Bonding Dynamics and Proton Transfer Processes in the Condensed Phase*. Kluwer Academic Publishers, 2002.

[55] A. J. Lock and H. J. Bakker, "Temperature Dependence of Vibrational Relaxation in Liquid H_2O," *The Journal of Chemical Physics*, vol. 117, pp. 1708–1713, 2002.

[56] I. Ohmine and H. Tanaka, "Fluctuation, Relaxations, and Hydration in Liquid Water. Hydrogen-Bond Rearrangement Dynamics," *Chemical Reviews*, vol. 93, pp. 2545–2566, 1993.

[57] P. Atkins, *Paula J. Atkins' Physical Chemistry*. New York: WH Freeman and Company, 2006.

[58] C. J. T. de Grotthuss, "Mémoire - Sur la Décomposition de l'Eau et des Corps qu'elle Tient en Dissolution à l'Aide de l'Électricité Galvanique," *Annales de Chimie (Paris)*, 1805.

[59] R. Janoschek, E.-G. Weidemann, H. Pfeiffer, and G. Zundel, "Extremely High Polarizability of Hydrogen Bonds," *Journal of the American Chemical Society*, vol. 94, pp. 2387–2396, 1972.

[60] R. Janoschek, E. G. Weidemann, and G. Zundel, "Calculated Frequencies and Intensities Associated with Coupling of the Proton Motion with the Hydrogen Bond Stretching Vibration in a Double Minimum Potential Surface," *Journal of the Chemical Society, Faraday Transactions 2: Molecular and Chemical Physics*, vol. 69, pp. 505–520, 1973.

[61] Q. Yu and J. M. Bowman, "How the Zundel ($H_5O_2^+$) Potential Can Be Used to Predict the Proton Stretch and Bend Frequencies of Larger Protonated Water Clusters," *The journal of physical chemistry letters*, vol. 7, pp. 5259–5265, 2016.

[62] D. Borgis, G. Tarjus, and H. Azzouz, "An Adiabatic Dynamical Simulation Study of the Zundel Polarization of Strongly H-Bonded Complexes in Solution," *The Journal of Chemical Physics*, vol. 97, pp. 1390–1400, 1992.

[63] K. Ando and J. T. Hynes, "Ionization of Acids in Water," ACS Publications, 1994.

[64] K. Ando and J. T. Hynes, "HCl Acid Ionization in Water: A Theoretical Molecular Modeling," *Journal of Molecular Liquids*, vol. 64, pp. 25–37, 1995.

[65] K. Ando and J. T. Hynes, "HF Acid Ionization in Water: The First Step," *Faraday Discussions*, vol. 102, pp. 435–441, 1995.

[66] N. Agmon, "The Grotthuss Mechanism," *Chemical Physics Letters*, vol. 244, pp. 456–462, 1995.

[67] M. Tuckerman, K. Laasonen, M. Sprik, and M. Parrinello, "Ab Initio Molecular Dynamics Simulation of the solvation and Transport of H_3O^+ and OH-Ions in Water," *The Journal of Physical Chemistry*, vol. 99, pp. 5749–5752, 1995.

[68] N. Agmon, "Hydrogen Bonds, Water Rotation and Proton Mobility," *Journal de Chimie Physique*, vol. 93, pp. 1714–1736, 1996.

[69] B. J. Gertner and J. T. Hynes, "Molecular Dynamics Simulation of Hydrochloric Acid Ionization at the Surface of Stratospheric Ice," *Science*, vol. 271, pp. 1563–1565, 1996.

[70] J. Lobaugh and G. A. Voth, "The Quantum Dynamics of an Excess Proton in Water," *The Journal of Chemical Physics*, vol. 104, pp. 2056–2069, 1996.

[71] M. E. Tuckerman, D. Marx, M. L. Klein, and M. Parrinello, "On the Quantum Nature of the Shared Proton in Hydrogen Bonds," *Science*, vol. 275, pp. 817–820, 1997.

[72] R. Vuilleumier and D. Borgis, "Quantum Dynamics of an Excess Proton in Water Using an Extended Empirical Valence-Bond Hamiltonian," *The Journal of Physical Chemistry B*, vol. 102, pp. 4261–4264, 1998.

[73] K. Ando and J. T. Hynes, "Acid-Base Proton Transfer and Ion Pair Formation in Solution," *Advances in Chemical Physics*, vol. 110, pp. 381–430, 1999.

[74] B. J. Gertner, G. H. Peslherbe, and J. T. Hynes, "Acid Ionization of HBr in a Small Water Cluster," *Israel Journal of Chemistry*, vol. 39, pp. 273–281, 1999.

[75] R. Vuilleumier and D. Borgis, "Transport and Spectroscopy of the Hydrated Proton: A Molecular Dynamics Study," *The Journal of Chemical Physics*, vol. 111, pp. 4251–4266, 1999.

[76] U. W. Schmitt and G. A. Voth, "The Computer Simulation of Proton Transport in Water," *The Journal of Chemical Physics*, vol. 111, pp. 9361–9381, 1999.

[77] P. L. Geissler, C. Dellago, D. Chandler, J. Hutter, and M. Parrinello, "Autoionization in Liquid Water," *Science*, vol. 291, pp. 2121–2124, 2001.

[78] A. Al-Halabi, R. Bianco, and J. T. Hynes, "Acid Dissociation of HBr on a Model Ice Surface," *The Journal of Physical Chemistry A*, vol. 106, pp. 7639–7645, 2002.

[79] J. Kim, U. W. Schmitt, J. A. Gruetzmacher, G. A. Voth, and N. E. Scherer, "The Vibrational Spectrum of the Hydrated Proton: Comparison of Experiment, Simulation, and Normal Mode Analysis," *The Journal of Chemical Physics*, vol. 116, pp. 737–746, 2002.

[80] N. Agmon, "Elementary Steps in Excited-State Proton Transfer," *The Journal of Physical Chemistry A*, vol. 109, pp. 13–35, 2005.

[81] H. Lapid, N. Agmon, M. K. Petersen, and G. A. Voth, "A Bond-Order Analysis of the Mechanism for Hydrated Proton Mobility in Liquid Water," *The Journal of Chemical Physics*, vol. 122, p. 014506, 2005.

[82] O. Markovitch and N. Agmon, "Structure and Energetics of the Hydronium Hydration Shells," *The Journal of Physical Chemistry A*, vol. 111, pp. 2253–2256, 2007.

[83] O. Markovitch, H. Chen, S. Izvekov, F. Paesani, G. A. Voth, and N. Agmon, "Special Pair Dance and Partner Selection: Elementary Steps in Proton Transport in Liquid Water," *The Journal of Physical Chemistry B*, vol. 112, pp. 9456–9466, 2008.

[84] J. Xu, Y. Zhang, and G. A. Voth, "Infrared Spectrum of the Hydrated Proton in Water," *The Journal of Physical Chemistry Letters*, vol. 2, pp. 81–86, 2010.

[85] P. M. Kiefer and J. T. Hynes, "Theoretical Aspects of Tunneling Proton Transfer Reactions in a Polar Environment," *Journal of Physical Organic Chemistry*, vol. 23, pp. 632–646, 2010.

[86] A. Hassanali, M. K. Prakash, H. Eshet, and M. Parrinello, "On the Recombination of Hydronium and Hydroxide Ions in Water," *Proceedings of the National Academy of Sciences*, vol. 108, pp. 20410–20415, 2011.

[87] R. Jorn, J. Savage, and G. A. Voth, "Proton Conduction in Exchange Membranes Across Multiple Length Scales," *Accounts of Chemical Research*, vol. 45, pp. 2002–2010, 2012.

[88] A. Hassanali, F. Giberti, J. Cuny, T. D. Kühne, and M. Parrinello, "Proton Transfer through the Water Gossamer," *Proceedings of the National Academy of Sciences*, vol. 110, pp. 13723–13728, 2013.

[89] M. V. Sigalov, N. Kalish, B. Carmeli, D. Pines, and E. Pines, "Probing Small Protonated Water Clusters in Acetonitrile Solutions by 1H NMR," *Zeitschrift für Physikalische Chemie*, vol. 227, pp. 983–1007, 2013.

[90] S. Daschakraborty, P. M. Kiefer, Y. Miller, Y. Motro, D. Pines, E. Pines, and J. T. Hynes, "Reaction Mechanism for Direct Proton Transfer from Carbonic Acid to a Strong Base in Aqueous Solution I: Acid and Base Coordinate and Charge Dynamics," *The Journal of Physical Chemistry B*, vol. 120, pp. 2271–2280, 2016.

[91] S. Daschakraborty, P. M. Kiefer, Y. Miller, Y. Motro, D. Pines, E. Pines, and J. T. Hynes, "Reaction Mechanism for Direct Proton Transfer from Carbonic Acid to a

Strong Base in Aqueous Solution II: Solvent Coordinate-Dependent Reaction Path," *The Journal of Physical Chemistry B*, vol. 120, pp. 2281–2290, 2016.

[92] M. E. Tuckerman, D. Marx, and M. Parrinello, "The Nature and Transport Mechanism of Hydrated Hydroxide Ions in Aqueous Solution," *Nature*, vol. 417, pp. 925–929, 2002.

[93] D. Eisenberg and W. Kauzmann, *The Structure and Properties of Water*. Oxford University Press on Demand, 2005.

[94] M. E. Tuckerman, A. Chandra, and D. Marx, "Structure and Dynamics of OH^-(aq)," *Accounts of Chemical Research*, vol. 39, pp. 151–158, 2006.

[95] J. A. Morrone and M. E. Tuckerman, "Ab Initio Molecular Dynamics Study of Proton Mobility in Liquid Methanol," *The Journal of Chemical Physics*, vol. 117, pp. 4403–4413, 2002.

[96] J. A. Morrone, K. E. Haslinger, and M. E. Tuckerman, "Ab Initio Molecular Dynamics Simulation of the Structure and Proton Transport Dynamics of Methanol-Water Solutions," *The Journal of Physical Chemistry B*, vol. 110, pp. 3712–3720, 2006.

[97] L. Rosso and M. E. Tuckerman, "Direct Evidence of an Anomalous Charge Transport Mechanism in Ammonium Perchlorate Crystal in an Ammonia-Rich Atmosphere from First-Principles Molecular Dynamics," *Solid State Ionics*, vol. 161, pp. 219–229, 2003.

[98] T. J. Day, U. W. Schmitt, and G. A. Voth, "The Mechanism of Hydrated Proton Transport in Water," *Journal of the American Chemical Society*, vol. 122, pp. 12027–12028, 2000.

[99] E. G. Diken, J. M. Headrick, J. R. Roscioli, J. C. Bopp, M. A. Johnson, and A. B. McCoy, "Fundamental Excitations of the Shared Proton in the $H_3O_2^-$ and $H_5O_2^+$ Complexes," *The Journal of Physical Chemistry A*, vol. 109, pp. 1487–1490, 2005. PMID: 16833469.

[100] J. A. Fournier, C. J. Johnson, C. T. Wolke, G. H. Weddle, A. B. Wolk, and M. A. Johnson, "Vibrational Spectral Signature of the Proton Defect in the Three-Dimensional $H^+(H_2O)_{21}$ Cluster," *Science*, vol. 344, pp. 1009–1012, 2014.

[101] J. A. Fournier, C. T. Wolke, M. A. Johnson, T. T. Odbadrakh, K. D. Jordan, S. M. Kathmann, and S. S. Xantheas, "Snapshots of Proton Accommodation at a Microscopic Water Surface: Understanding the Vibrational Spectral Signatures of the Charge Defect in Cryogenically Cooled $H^+(H_2O)_{n=2-28}$ Clusters," *The Journal of Physical Chemistry A*, vol. 119, pp. 9425–9440, 2015.

[102] H.-H. Limbach, P. M. Tolstoy, N. Pérez-Hernández, J. Guo, I. G. Shenderovich, and G. S. Denisov, "OHO Hydrogen Bond Geometries and NMR Chemical Shifts: From Equilibrium Structures to Geometric H/D Isotope Effects, with Applications for Water, Protonated Water, and Compressed Ice," *Israel Journal of Chemistry*, vol. 49, 2009.

[103] S. Woutersen and H. J. Bakker, "Ultrafast Vibrational and Structural Dynamics of the Proton in Liquid Water," *Physical Review Letters*, vol. 96, p. 138305, 2006.

[104] S. Mukamel, *Principles of Nonlinear Optical Spectroscopy.* No. 6, Oxford University Press on Demand, 1999.

[105] M. Cho, *Two-Dimensional Optical Spectroscopy.* CRC press, 2009.

[106] P. Hamm and M. Zanni, *Concepts and Methods of 2D Infrared Spectroscopy.* Cambridge University Press, 2011.

[107] R. Costard, *Ultrafast Dynamics of Phospholipid-Water Interfaces Studied by Nonlinear Time-Resolved Vibrational Spectroscopy.* Springer, 2015.

[108] W. S. Struve, *Fundamentals of Molecular Spectroscopy.* Wiley New York, 1989.

[109] H. Goldstein, *Classical Mechanics.* Addison-Wesley Press, 1965.

[110] L. A. Woodward, *Introduction to the Theory of Molecular Vibrations and Vibrational Spectroscopy.* Oxford at the Clarendon Press, 1972.

[111] J. P. Kraack, *Ultrafast Structural Molecular Dynamics Investigated with 2D Infrared Spectroscopy Methods*, vol. 375. Springer, 2017.

[112] R. Kubo, "A Stochastic Theory of Line Shape," *Stochastic Processes in Chemical Physics*, vol. 15, pp. 101–127, 1969.

[113] K. Kwak, S. Park, I. J. Finkelstein, and M. D. Fayer, "Frequency-Frequency Correlation Functions and Apodization in Two-Dimensional Infrared Vibrational Echo Spectroscopy: A New Approach," *The Journal of Chemical Physics*, vol. 127, p. 124503, 2007.

[114] R. J. Abbott and D. W. Oxtoby, "Exchange Dephasing and Motional Narrowing of Vibrational Modes," *The Journal of Chemical Physics*, vol. 70, pp. 4703–4707, 1979.

[115] R. W. Boyd, *Nonlinear Optics.* Academic Press, 2008.

[116] S. Mukamel, *Principles of Nonlinear Optics and Spectroscopy.* Oxford University Press, 1995.

[117] V. Chernyak and S. Mukamel, "Time-Dependent Density-Matrix Functional in Liouville Space and the Optical Response of Many-Electron Systems," *Physical Review A*, vol. 52, p. 3601, 1995.

[118] P. Hamm, "Coherent Effects in Femtosecond Infrared Spectroscopy," *Chemical Physics*, vol. 200, pp. 415–429, 1995.

[119] T. Meier, V. Chernyak, and S. Mukamel, "Femtosecond Photon Echoes in Molecular Aggregates," *The Journal of Chemical Physics*, vol. 107, pp. 8759–8780, 1997.

[120] A. Okada, V. Chernyak, and S. Mukamel, "Solvent Reorganization in Long-Range Electron Transfer: Density Matrix Approach," *The Journal of Physical Chemistry A*, vol. 102, pp. 1241–1251, 1998.

[121] S.-H. Shim and M. T. Zanni, "How to Turn your Pump–Probe Instrument into a Multidimensional Spectrometer: 2D IR and Vis Spectroscopies via Pulse Shaping," *Physical Chemistry Chemical Physics*, vol. 11, pp. 748–761, 2009.

[122] Y. S. Kim and R. M. Hochstrasser, "Applications of 2D IR Spectroscopy to Peptides, Proteins, and Hydrogen-Bond Dynamics," *The Journal of Physical Chemistry B*, vol. 113, pp. 8231–8251, 2009.

[123] Y. S. Kim and R. M. Hochstrasser, "Chemical Exchange 2D IR of Hydrogen-Bond Making and Breaking," *Proceedings of the National Academy of Sciences of the United States of America*, vol. 102, pp. 11185–11190, 2005.

[124] G. Cerullo and S. D. Silvestri, "Ultrafast Optical Parametric Amplifiers," *Review of Scientific Instruments*, vol. 74, pp. 1–18, 2003.

[125] Coherent, 5100 Patrick Henry Drive, Santa Clara, CA 95054, *Operator's Manual Legend Laser System Kilohertz, Diode-Pumped, Ultrafast Ti:Sapphire Amplifier.*

[126] Coherent, 5100 Patrick Henry Drive, Santa Clara, CA 95054, *Operator's Manual Libra Ultrafast Amplifier Laser System.*

[127] Coherent, 5100 Patrick Henry Drive, Santa Clara, CA 95054, *Operator's Manual Micra Modelocked Ti:Sapphire Laser.*

[128] G. Cerullo, C. Manzoni, T. Elsaesser, G. Lanzani, M. Först, T. Dekorsy, M. Gühr, and S. L. Dexheimer, *Coherent Vibrational Dynamics*, vol. 36 of *Practical Spectroscopy Series.* CRC Press, 2008.

[129] R. A. Kaindl, M. Wurm, K. Reimann, P. Hamm, A. M. Weiner, and M. Woerner, "Generation, Shaping, and Characterization of Intense Femtosecond Pulses Tunable from 3 to 20 µm," *J. Opt. Soc. Am. B*, vol. 17, pp. 2086–2094, 2000.

[130] M. D. Fayer, *Ultrafast Infrared Vibrational Spectroscopy.* CRC Press, 2013.

[131] M. Cowan, J. Ogilvie, and R. Miller, "Two-Dimensional Spectroscopy Using Diffractive Optics Based Phased-Locked Photon Echoes," *Chemical Physics Letters*, vol. 386, pp. 184 – 189, 2004.

[132] A. C. Eckbreth, "BOXCARS: Crossed-Beam Phase-Matched CARS Generation in Gases," *Applied Physics Letters*, vol. 32, pp. 421–423, 1978.

[133] T. Brixner, T. Mančal, I. V. Stiopkin, and G. R. Fleming, "Phase-Stabilized Two-Dimensional Electronic spectroscopy," *The Journal of Chemical Physics*, vol. 121, pp. 4221–4236, 2004.

[134] V. Volkov, R. Schanz, and P. Hamm, "Active Phase Stabilization in Fourier-Transform Two-Dimensional Infrared Spectroscopy," *Opt. Lett.*, vol. 30, pp. 2010–2012, 2005.

[135] L. P. DeFlores, R. A. Nicodemus, and A. Tokmakoff, "Two-Dimensional Fourier Transform Spectroscopy in the Pump-Probe Geometry," *Optics Letters*, vol. 32, pp. 2966–2968, 2007.

[136] J. Helbing and P. Hamm, "Compact Implementation of Fourier Transform Two-Dimensional IR Spectroscopy without Phase Ambiguity," *Journal of the Optical Society of America B*, vol. 28, pp. 171–178, 2011.

[137] R. Trebino, K. W. DeLong, D. N. Fittinghoff, J. N. Sweetser, M. A. Krumbügel, B. A. Richman, and D. J. Kane, "Measuring Ultrashort Laser Pulses in the Time-Frequency Domain Using Frequency-Resolved Optical Gating," *Review of Scientific Instruments*, vol. 68, pp. 3277–3295, 1997.

[138] J. E. Bertie and Z. Lan, "Liquid Water-Acetonitrile Mixtures at 25 ° C: The Hydrogen-Bonded Structure Studied through Infrared Absolute Integrated Absorption Intensities," *The Journal of Physical Chemistry B*, vol. 101, pp. 4111–4119, 1997.

[139] T. Takamuku, M. Tabata, A. Yamaguchi, J. Nishimoto, M. Kumamoto, H. Wakita, and T. Yamaguchi, "Liquid Structure of Acetonitrile-Water Mixtures by X-Ray Diffraction and Infrared Spectroscopy," *The Journal of Physical Chemistry B*, vol. 102, pp. 8880–8888, 1998.

[140] K. R. Harris and P. J. Newitt, "Diffusion and Structure in Aqueous Amphiphile Mixtures: Water-Acetonitrile," *The Journal of Physical Chemistry B*, vol. 103, pp. 7015–7018, 1999.

[141] I. M. Kolthoff and M. Chantooni Jr, "Protonation in Acetonitrile of Water, Alcohols, and Diethyl Ether," *Journal of the American Chemical Society*, vol. 90, pp. 3320–3326, 1968.

[142] M. K. Chantooni Jr and I. M. Kolthoff, "Reevaluation of the Formation Constants of the Hydrated Proton in Acetonitrile," *Journal of the American Chemical Society*, vol. 92, pp. 2236–2239, 1970.

[143] Q. Yu and J. M. Bowman, "Communication: VSCF/VCI Vibrational Spectroscopy of $H_7O_3^+$ and $H_9O_4^+$ Using High-Level, Many-Body Potential Energy Surface and Dipole Moment Surfaces," *The Journal of Chemical Physics*, vol. 146, p. 121102, 2017.

[144] A. B. McCoy, T. L. Guasco, C. M. Leavitt, S. G. Olesen, and M. A. Johnson, "Vibrational Manifestations of Strong Non-Condon Effects in the $H_3O^+ \cdot X_3$ (X= Ar, N_2, CH_4, H_2O) Complexes: A Possible Explanation for the Intensity in the "Association Band" in the Vibrational Spectrum of Water," *Physical Chemistry Chemical Physics*, vol. 14, pp. 7205–7214, 2012.

[145] O. Vendrell, F. Gatti, and H.-D. Meyer, "Full Dimensional (15-Dimensional) Quantum-Dynamical Simulation of the Protonated Water Dimer. II. Infrared Spectrum and Vibrational Dynamics," *The Journal of Chemical Physics*, vol. 127, p. 184303, 2007.

[146] F. Dahms, R. Costard, E. Pines, B. P. Fingerhut, E. T. J. Nibbering, and T. Elsaesser, "The Hydrated Excess Proton in the Zundel Cation $H_5O_2^+$: The Role of Ultrafast Solvent Fluctuations," *Angewandte Chemie International Edition*, vol. 55, pp. 10600–10605, 2016.

[147] "Chemical Resistance Chart - PEEK." `https://www.zeusinc.com/materials/peek/chemical-resistance-chart-peek`. Accessed: 14.11.2017.

[148] "PTFE Chemical Resistance Chart." `http://www.componentsupplycompany.com/PTFE-Chemical-Resistance-Data.html`. Accessed: 14.11.2017.

[149] "V2A - Rustproof Steel and Scale-Resistant Steel." https://www.rime.de/en/101/v2a-steel/. Accessed: 14.11.2017.

[150] G. Seifert, T. Patzlaff, and H. Graener, "Comprehensive Investigation of Vibrational Relaxation of Non-Hydrogen-Bonded Water Molecules in Liquids," *The Journal of Chemical Physics*, vol. 125, p. 154506, 2006.

[151] D. Cringus, S. Yeremenko, M. S. Pshenichnikov, and D. A. Wiersma, "Hydrogen Bonding and Vibrational Energy Relaxation in Water-Acetonitrile Mixtures," *The Journal of Physical Chemistry B*, vol. 108, pp. 10376–10387, 2004.

[152] D. Cringus, T. l. C. Jansen, M. S. Pshenichnikov, and D. A. Wiersma, "Ultrafast Anisotropy Dynamics of Water Molecules Dissolved in Acetonitrile," *The Journal of Chemical Physics*, vol. 127, p. 084507, 2007.

[153] F. Dahms, R. Costard, E. T. Nibbering, and T. Elsaesser, "Ultrafast Vibrational Energy Flow in Water Monomers in Acetonitrile," *Chemical Physics Letters*, vol. 652, pp. 50 – 55, 2016.

[154] W. B. Carpenter, J. A. Fournier, R. Biswas, G. A. Voth, and A. Tokmakoff, "Delocalization and Stretch-Bend Mixing of the HOH Bend in Liquid Water," *The Journal of Chemical Physics*, vol. 147, p. 084503, 2017.

[155] R. Rey and J. T. Hynes, "Vibrational Energy Relaxation of HOD in Liquid D_2O," *The Journal of Chemical Physics*, vol. 104, pp. 2356–2368, 1996.

[156] N. P. Ernsting, G. M. Photiadis, H. Hennig, and T. Laurent, "Rotational Friction Kernel in Water from the Femtosecond Time-Resolved Optical Kerr Effect of Acetonitrile/Water Mixtures," *The Journal of Physical Chemistry A*, vol. 106, pp. 9159–9173, 2002.

[157] D. S. Venables and C. A. Schmuttenmaer, "Spectroscopy and Dynamics of Mixtures of Water with Acetone, Acetonitrile, and Methanol," *The Journal of Chemical Physics*, vol. 113, pp. 11222–11236, 2000.

[158] B. Schrader, *Raman / Infrared Atlas of Organic Compounds*. VCH Verlagsgesellschaft, 1989.

[159] E. S. Stoyanov and C. A. Reed, "IR Spectrum of the $H_5O_2^+$ Cation in the Context of Proton Disolvates L-H^+-L," *The Journal of Physical Chemistry A*, vol. 110, pp. 12992–13002, 2006.

[160] F. Dahms, B. P. Fingerhut, E. T. Nibbering, E. Pines, and T. Elsaesser, "Large-Amplitude Transfer Motion of Hydrated Excess Protons Mapped by Ultrafast 2D IR Spectroscopy," *Science*, vol. 357, pp. 491–495, 2017.

[161] D. McMorrow and W. T. Lotshaw, "Intermolecular Dynamics in Acetonitrile Probed with Femtosecond Fourier-Transform Raman Spectroscopy," *The Journal of Physical Chemistry*, vol. 95, pp. 10395–10406, 1991.

[162] S. D. Fried and S. G. Boxer, "Measuring Electric Fields and Noncovalent Interactions Using the Vibrational Stark Effect," *Accounts of Chemical Research*, vol. 48, pp. 998–1006, 2015.

[163] N. Ottosson, L. Liu, and H. Bakker, "Vibrational Relaxation of the Aqueous Proton in Acetonitrile: Ultrafast Cluster Cooling and Vibrational Predissociation," *The Journal of Physical Chemistry B*, vol. 120, pp. 7154–7163, 2016.

[164] D. Marx, M. E. Tuckerman, and M. Parrinello, "Solvated Excess Protons in Water: Quantum Effects on the Hydration Structure," *Journal of Physics: Condensed Matter*, vol. 12, pp. A153–A159, 2000.

[165] J. Xu, Y. Zhang, and G. A. Voth, "Infrared Spectrum of the Hydrated Proton in Water," *The Journal of Physical Chemistry Letters*, vol. 2, pp. 81–86, 2011.

[166] R. Biswas, W. Carpenter, G. A. Voth, and A. Tokmakoff, "Molecular Modeling and Assignment of IR Spectra of the Hydrated Excess Proton in Isotopically Dilute Water," *The Journal of Chemical Physics*, vol. 145, p. 154504, 2016.

[167] R. Biswas, W. Carpenter, J. A. Fournier, G. A. Voth, and A. Tokmakoff, "IR Spectral Assignments for the Hydrated Excess Proton in Liquid Water," *The Journal of Chemical Physics*, vol. 146, p. 154507, 2017.

[168] *Mathematica*. Version 10, Wolfram Research, Inc., 2014.

[169] M. Gheorghiu and A. Tokmakoff, "5.33 Advanced Chemical Experimentation and Instrumentation." `https://ocw.mit.edu/courses/chemistry/5-33-advanced-chemical-experimentation-and-instrumentation-fall-2007/labs/laser_appendix3.pdf`, 2007. Accessed: 2018-02-02.

[170] M. Deegan and P. Knowles, "Perturbative Corrections to Account for Triple Excitations in Closed and Open Shell Coupled Cluster Theories," *Chemical Physics Letters*, vol. 227, pp. 321–326, 1994.

[171] J. K. Watson, "Simplification of the Molecular Vibration-Rotation Hamiltonian," *Molecular Physics*, vol. 15, pp. 479–490, 1968.

9 Appendix

9.1 Rate-Equation Model

In order to retrieve characteristic time constants for the vibrational energy relaxation processes of Zundel cations in acetonitrile and water, a rate-equation model was employed. The model is based on the relaxation scheme shown in figure 9.1 and consists of exponentially rising and decaying components convoluted with the cross correlation of the experiment. Time constants are derived by least square fits of the experimental data with this model.

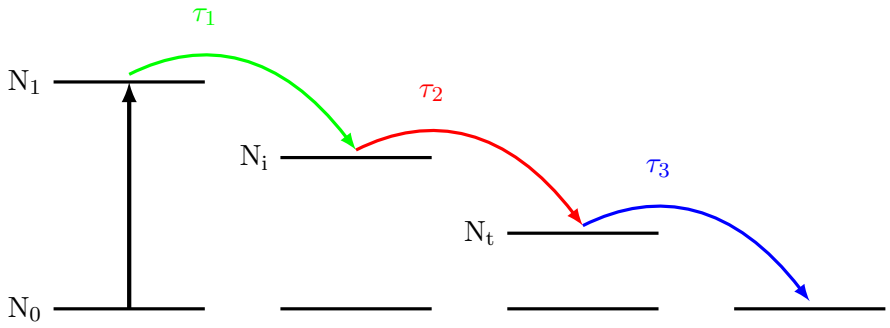

Figure 9.1: Scheme that was used to describe the vibrational energy relaxation (VER) processes in Zundel cations. An excitation pulse transfers population from N_0 to N_1 (black arrow). The excited state N_1 depopulates with τ_1 (green arrow) leading to energy redistribution processes in the Zundel cation described by the intermediate state N_i. The redistribution of excess energy results in the formation of a locally hot ground state with τ_2 (red arrow). The Zundel cation is de-excited by transferring its vibrational excess energy to the acetonitrile environment with τ_3 (blue arrow).

In detail, vibrational excitation causes population to transfer from state N_0 to N_1 (black arrow in Fig. 9.1). State N_1 decays with an intrinsic time constant τ_1 accounting for population relaxation. Subsequently, energy is redistributed within the excited molecule, represented by the intermediate state N_i. This energy redistribution is triggered by the population relaxation of N_1 thus N_i has a formation time according to τ_1 (green arrow) and a decay time τ_2 that accounts for the time needed to redistribute the energy into lower frequency modes of the excited Zundel cation, resulting in a locally hot ground state N_t (red arrow). N_t has a rise time equal to τ_2 and decays by transferring the excess energy from the excited Zundel cation to the acetonitrile environment with the time constant τ_3 (blue arrow). Rate-equations describing the VER processes are summarized in Eqn. 9.1.

$$\begin{aligned}\frac{\mathrm{dN_1}}{\mathrm{dt}} &= -\frac{\mathrm{N_1}}{\tau_1} \\ \frac{\mathrm{dN_i}}{\mathrm{dt}} &= \frac{\mathrm{N_1}}{\tau_1} - \frac{\mathrm{N_i}}{\tau_2} \\ \frac{\mathrm{dN_t}}{\mathrm{dt}} &= \frac{\mathrm{N_i}}{\tau_2} - \frac{\mathrm{N_t}}{\tau_3}\end{aligned} \tag{9.1}$$

The rate-equations where solved with the Mathematica 10 software package [168], employing exponential kinetics:

$$N_x(t) = A_x \cdot e^{-t/\tau} \ . \tag{9.2}$$

The calculated equations where convoluted with the cross-correlation of the experiment, using a formalism described in [169]:

$$I(t) = A \cdot \exp\left(\frac{\sigma^2}{2\tau^2} - \frac{\mathrm{t}}{\tau}\right)\left[1 - \mathrm{erf}\left(\frac{\sigma^2 - \mathrm{t}\tau}{\sqrt{2}\sigma\tau}\right)\right] \ . \tag{9.3}$$

9.2 Theoretical Simulations

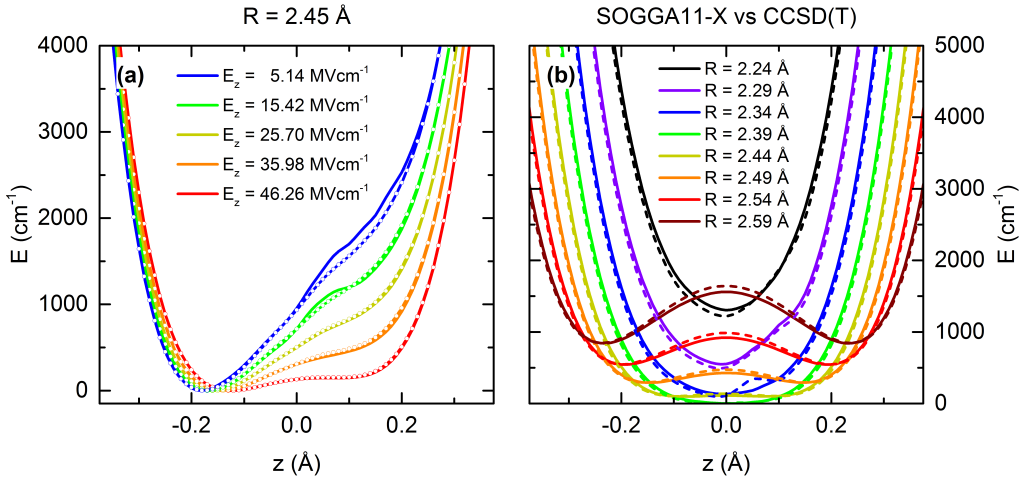

Figure 9.2: **(a)** Calculated potentials of the O· · ·H$^+$ · ··O mode (z) for a fixed O· · ·O distance R = 2.45 Å and varying external fields E_z from a non-perturbative (symbols) and a perturbative (solid lines) approach. **(b)** Cuts taken at different R values of the 2D PES of z and R calculated with the SOGGA11-X functional (solid lines) and the CCSD(T) functional (dashed lines), respectively.

This section briefly demonstrates the model and methods used to simulate the theoretical results presented throughout this work. A more detailed description is given in the supplementary information of references [146] and [160]. Calculations were carried out by Dr. Benjamin Fingerhut[1], who kindly provides the particular results for this thesis.

[1] Max Born Institut für Nichtlineare Optik und Kurzzeitspektroskopie
E-Mail: Fingerhut@mbi-berlin.de

The goal of the simulations is to understand the influence of the fluctuating electric fields the acetonitrile environment exerts on the proton transfer coordinate $O\cdots H^+\cdots O$ (z) and to investigate the effect of intermode-coupling on the proton potential, especially to the $O\cdots O$ mode (R) in $H_5O_2^+$.
Initially, the potential energy surface of z and R is constructed with a two-dimensional model based on the original work of Janoschek et al. [59] employing modern wave-function based coupled-cluster singles-doubles with perturbative triples corrections level of theory (CCSD(T)/aug-cc-pVTZ) [170]. Here, other internal coordinates are optimized on density functional [DF(PBE0); aug-cc-pVTZ basis] level of theory. Inter-mode coupling is included with a three-dimensional model based on the Watson Hamiltonian described in [171].
The 2D model is constructed for the bare $H_5O_2^+$ molecule and influences of the fluctuating environment are implemented as static electrical fields E_z along the z coordinate. Sampling E_z in a range typical for ACN allows to map the influence of the average electrical field, structurally different solvent configurations exert on the proton potential, affecting transition frequencies and transition dipole moments.
Treating this model with a non-perturbative approach poses high computational cost, as one has to solve the electronic structure problem in the Schrödinger equation for each value of E_z individually. This can be circumvented by perturbative treatment, where one only has to solve the Schrödinger equation for $E_z = 0$.
A comparison of the treatments for a fixed $O\cdots O$ distance R = 2.45 Å and varying electrical fields along z is shown in Fig. 9.2a. For field strengths <46 MV/cm, the agreement between both treatments is compelling, thus calculations were performed with a perturbative approach.
To better capture the dynamical character of the environment, not just as a statistical solvent averaged electrical field along z, an enhanced full dimensional model was developed. In this QM/MM model, the Zundel cation is treated quantum mechanically (QM) on the density functional level of theory employing a hybrid GGA functional SOGGA11-X in an aug-cc-pVTZ basis. The ACN solvent is treated on the molecular mechanics (MM) level of theory, employing a point charge model that generates the electrical fields. This approach does not require an initial assumption about the field strengths E_z and the $H_5O_2^+$ moiety is simulated in a fluctuating electrostatic solvent. The accuracy of the SOGGA11-X/aug-cc-pVTZ level of theory is in excellent agreement with the results obtained from the 2D model on the CCSD(T)/aug-cc-pVTZ level of theory described earlier (Fig. 9.2b), while reducing the computational cost by a factor of 30.

Danksagung

Mein besonderer Dank gilt meinem Doktorvater **Prof. Dr. Thomas Elsässer** für die exellente Betreuung während meiner gesamten Doktorandenzeit, die vielen wissenschaftlichen Beiträge zu meiner Arbeit und der Gelegenheit meine Promotion im hervorragenden Arbeitsumfeld des Max-Born-Instituts durchführen zu können.
Ich möchte mich herzlichst bei **Dr. Erik Nibbering** für seine stetige Unterstüzung und Förderung bedanken, die maßgeblich zu meiner Entwicklung als Wissenschaftler beigetragen hat. Bei Fragen und Problemen bin ich immer auf ein offenes Ohr gestoßen und der große Erfahrungsschatz haben mir sehr weitergeholfen.
Besonders möchte ich mich auch bei **Dr. René Costard** für die umfassende Einführung in die Kurzzeitspektroskopie und die Arbeitsweisen in den Laboren bedanken. Die gemeinsame Zeit am MBI hat mir viel Freude bereitet und den Weg für eine erfolgreiche Promotion geebnet.
Ich bedanke mich aufrichtig bei **Dr. Benjamin Fingerhut** für die unzählbaren Ratschläge und wissenschaftlichen Beiträge zu meiner Arbeit. Die vielen themenbezogenen Diskussionen haben mein physikalisches Verständnis der Materie ungemein erweitert.
Ich bedanke mich bei meinen Kollegen: **Benjamin Fingerhut, Martin Richter, Mara Oßwald, Eva Brüning, Jakob Schauss, Andrej Codescu, Nirmalendu Acharyya und Achintya Kundu**, die mir die tägliche Mittagspausen und den Arbeitsaltag verschönert haben.
Ganz besonders möchte ich mich auch bei **Regina Lendt** bedanken, die mit viel Einsatz, Freundlichkeit und Kuchen meine Arbeitzzeit versüßt hat. **Peter Scholze** danke ich für die Hilfe bei der Entwicklung, Planung und Fertigung der Nanofluiden-Zelle für meine säurehaltigen Proben, ohne die die Experimente gar nicht erst hätten stattfinden können.

Mein größter Dank gilt **meiner Familie**, die mich immer und bedingungslos unterstützt hat. Ihr habt mich auf meinem gesamten Weg begleitet und zu dem Menschen gemacht der ich heute bin. Ich bedanke mich auch für die Zeit und Mühe die ihr investiert habt, die Freude die ihr geteilt und den Trost den ihr gespendet habt.

Selbständigkeitserklärung

Ich erkläre, dass ich die Dissertation selbständig und nur unter Verwendung der von mir gemäß §7 Abs. 3 der Promotionsordnung der Mathematisch-Naturwissenschaftlichen Fakultät, veröffentlicht im Amtlichen Mitteilungsblatt der Humboldt-Universität zu Berlin Nr. 126/2014 am 18.11.2014 angegebenen Hilfsmittel angefertigt habe.